Molecular Cell

Article

Sexually dimorphic RNA helicases DDX3X and DDX3Y differentially regulate RNA metabolism through phase separation

Graphical abstract

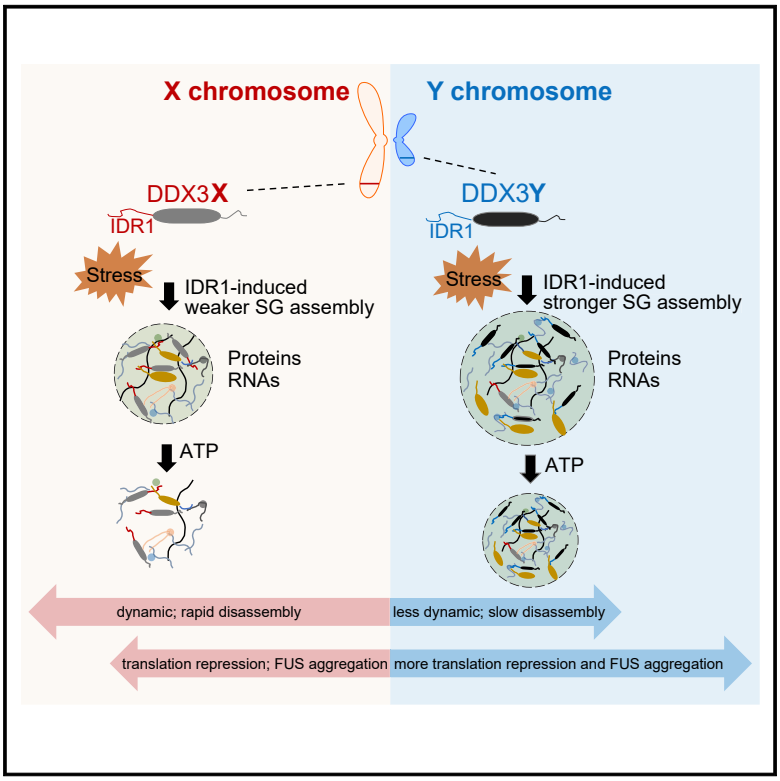

Highlights

- The N-terminal IDR of DDX3Y more strongly promotes condensation than that of DDX3X
- Slower ATPase activity of DDX3Y contributes to weaker dissolution of condensates
- Stronger phase separation of DDX3Y than DDX3X leads to more translation repression
- DDX3Y condensates enhance aggregation of FUS more strongly than DDX3X

Authors

Hui Shen, Amber Yanas, Michael C. Owens, ..., James Shorter, Yale E. Goldman, Kathy Fange Liu

Correspondence

liufg@pennmedicine.upenn.edu

In brief

Shen et al. report that the Y chromosome-encoded RNA helicase DDX3Y has a stronger propensity for liquid-liquid phase separation compared with its X chromosome-encoded homolog DDX3X, which results in the stronger repression of mRNA translation and promotion of FUS aggregation under stress conditions.

Shen et al., 2022, Molecular Cell *82*, 1–16
July 21, 2022
https://doi.org/10.1016/j.molcel.2022.04.022

CellPress

Molecular Cell

CellPress

Article

Sexually dimorphic RNA helicases DDX3X and DDX3Y differentially regulate RNA metabolism through phase separation

Hui Shen,[1,7] Amber Yanas,[1,2,7] Michael C. Owens,[1,2] Celia Zhang,[1] Clark Fritsch,[3] Charlotte M. Fare,[1,2] Katie E. Copley,[1,4] James Shorter,[1,2,3,4] Yale E. Goldman,[2,5,6] and Kathy Fange Liu[1,2,8,*]

[1]Department of Biochemistry and Biophysics, Perelman School of Medicine, University of Pennsylvania, Philadelphia, PA 19104, USA
[2]Graduate Group in Biochemistry and Molecular Biophysics, Perelman School of Medicine, University of Pennsylvania, Philadelphia, PA 19104, USA
[3]Graduate Group in Cellular and Molecular Biology, Perelman School of Medicine, University of Pennsylvania, Philadelphia, PA 19104, USA
[4]Graduate Group in Neuroscience, Perelman School of Medicine, University of Pennsylvania, Philadelphia, PA 19104, USA
[5]Department of Physiology, Perelman School of Medicine, University of Pennsylvania, Philadelphia, PA 19104, USA
[6]Pennsylvania Muscle Institute, Perelman School of Medicine, University of Pennsylvania, Philadelphia, PA 19104, USA
[7]These authors contributed equally
[8]Lead contact
*Correspondence: liufg@pennmedicine.upenn.edu
https://doi.org/10.1016/j.molcel.2022.04.022

SUMMARY

Sex differences are pervasive in human health and disease. One major key to sex-biased differences lies in the sex chromosomes. Although the functions of the X chromosome proteins are well appreciated, how they compare with their Y chromosome homologs remains elusive. Herein, using ensemble and single-molecule techniques, we report that the sex chromosome-encoded RNA helicases DDX3X and DDX3Y are distinct in their propensities for liquid-liquid phase separation (LLPS), dissolution, and translation repression. We demonstrate that the N-terminal intrinsically disordered region of DDX3Y more strongly promotes LLPS than the corresponding region of DDX3X and that the weaker ATPase activity of DDX3Y, compared with DDX3X, contributes to the slower disassembly dynamics of DDX3Y-positive condensates. Interestingly, DDX3Y-dependent LLPS represses mRNA translation and enhances aggregation of FUS more strongly than DDX3X-dependent LLPS. Our study provides a platform for future comparisons of sex chromosome-encoded protein homologs, providing insights into sex differences in RNA metabolism and human disease.

INTRODUCTION

Many human disorders manifest in a sex-biased manner, yet the molecular mechanisms responsible for these biases are not fully understood (Mauvais-Jarvis et al., 2020). On a genetic level, the most significant differences between males and females lie in the sex chromosomes. Although the X and Y chromosomes are, by and large, not homologous, a handful of X chromosome-encoded proteins have Y chromosome-encoded homologs (Bellott et al., 2014). These Y chromosome-encoded homologs were historically thought to only be expressed and to function in the reproductive system. However, a growing body of evidence suggests that Y chromosome-encoded homologs are not only expressed throughout the body at transcript and protein levels but are also evolutionarily conserved (Godfrey et al., 2020). However, the functional differences between the protein homologs encoded on the X and Y chromosomes have not been thoroughly investigated. Emerging evidence is starting to reveal that Y chromosome-encoded proteins may function differently from their X chromosome-encoded homologs (Gozdecka et al., 2018; Nguyen et al., 2020; Shi et al., 2021).

One pair of sex chromosome-encoded proteins are the RNA helicases DDX3X and DDX3Y. In females (specified as XX individuals), DDX3X escapes X inactivation, and two copies of the protein are expressed, whereas in males (specified as XY individuals), one copy of each of the X- and Y-linked proteins is expressed (Cotton et al., 2015; Ditton et al., 2004). The *DDX3X* gene (Xp11.4) encodes a DEAD-box RNA helicase (Sharma and Jankowsky, 2014), which is evolutionarily conserved in *C. elegans* (LAF-1), yeast (Ded1p), *Drosophila* (Belle), and humans (Sharma and Jankowsky, 2014). The functions of DDX3X are more well studied than those of DDX3Y, including its activity as a translation-initiation factor (Lai et al., 2008; Lee et al., 2008) for a set of mRNAs with highly structured 5′ UTRs (Ku et al., 2019; Lai et al., 2008; Lee et al., 2008; Phung et al., 2019; Soto-Rifo et al., 2012), and at repeat-associated non-AUG (RAN) start sites

Please cite this article in press as: Shen et al., Sexually dimorphic RNA helicases DDX3X and DDX3Y differentially regulate RNA metabolism through phase separation, Molecular Cell (2022), https://doi.org/10.1016/j.molcel.2022.04.022

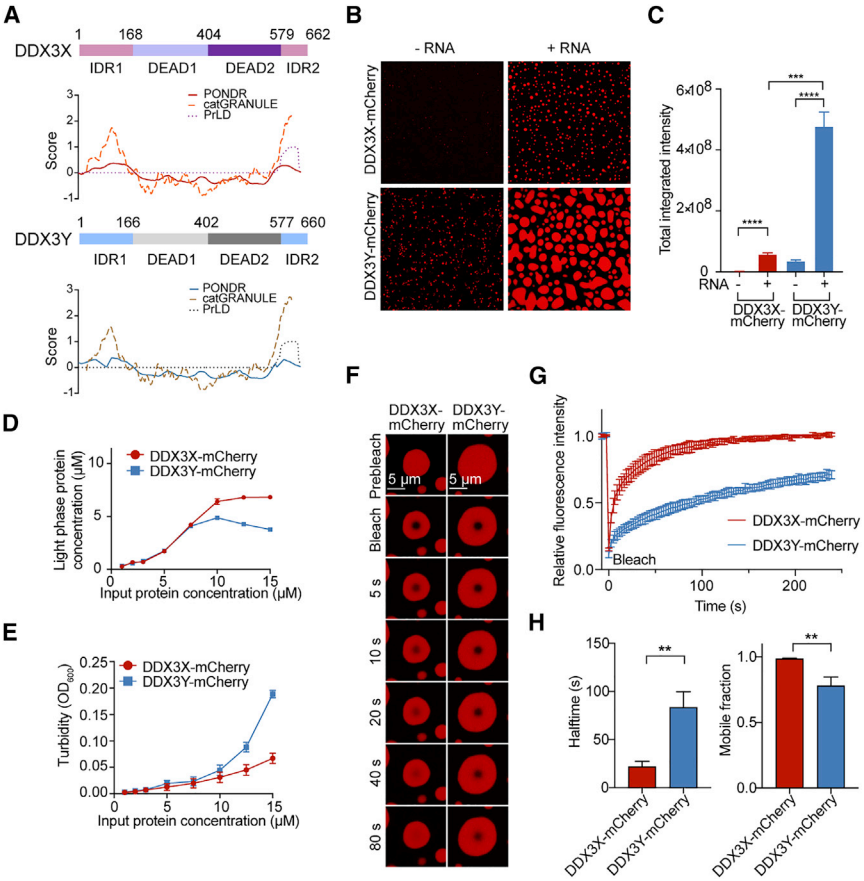

Figure 1. DDX3Y has a stronger LLPS propensity compared with DDX3X *in vitro*

(A) Structural prediction of DDX3X and DDX3Y using PONDR (natural disordered regions), PLAAC (prion-like amino acid regions), and catGRANULE (LLPS propensity).

(B) *In vitro* droplet formation of 10 μM recombinant DDX3X-mCherry or DDX3Y-mCherry in the absence or presence of 200 ng/μL poly(U)-RNA. Scale bars, 25 μm.

(C) Quantification of the total integrated intensity of DDX3X condensation and DDX3Y condensation in (B). A two-tailed t test was used to calculate the p value. ***$p < 0.001$, **** $p < 0.0001$.

(D) Concentrations of DDX3 proteins in the light phase (supernatant after centrifugation) versus input protein concentrations.

(E) Turbidity (absorbance at 600 nm) of DDX3X-mCherry and DDX3Y-mCherry LLPS. The mean value of turbidity and protein concentration for each condition from three separate protein purifications and three technical repeats were plotted in (D) and (E).

(F) Time-lapse images of *in vitro* FRAP experiments. The FRAP experiments were performed identically for DDX3X-mCherry and DDX3Y-mCherry droplets.

(G) FRAP curves for *in vitro* droplets of DDX3X-mCherry (red) and DDX3Y-mCherry (blue). The traces of the FRAP data represent mean ± SEM (n = 3, from three independent experiments).

(H) Half-time and mobile fractions from (G). A two-tailed t test was used to calculate the p value. **$p < 0.01$.

See also Figure S1.

(Cheng et al., 2019; Linsalata et al., 2019). In addition, DDX3X (and its homologs) undergoes liquid-liquid phase separation (LLPS) and is a conserved component of stress granules (SGs) (Beckham et al., 2008; Elbaum-Garfinkle et al., 2015; Iserman et al., 2020; Shih et al., 2012; Valentin-Vega et al., 2016). SGs, which are composed of RNAs and proteins and form part of the stress response, are correlated with changes to mRNA metabolism, including translational repression (Kimball et al., 2003; Moon et al., 2019). Dysregulation of SGs has been implicated in a wide range of human disorders, including cardiomyopathy, Alzheimer's disease, and amyotrophic lateral sclerosis (ALS), many of which present with varying degrees of sex-biased incidences, progressions, and outcomes (Ash et al., 2014; Baradaran-Heravi et al., 2020; Ferretti et al., 2018; Manjaly et al., 2010; McCombe and Henderson, 2010; Meyer et al., 2014; Schneider et al., 2020; Watkins et al., 2020). Additionally, DDX3X mutations can lead to DDX3X syndrome, a disorder that accounts for 1%–3% of intellectual disability cases and is more prevalent in females than in males (Iossifov et al., 2014; Lennox et al., 2020; Ruzzo et al., 2019; Scala et al., 2019; Snijders Blok et al., 2015; Wang et al., 2018b).

Notably, the presence of the *DDX3Y* gene can only sometimes compensate for the loss of the *DDX3X* gene (Chen et al., 2016). For example, *Ddx3y* cannot fully compensate for the loss of *Ddx3x* during embryonic and neuronal development in mice (Chen et al., 2016; Patmore et al., 2020). Furthermore, male mice, but not female mice, survive conditional knockout of *Ddx3x* in the bone marrow, but these male mice present with distinct deficiencies in innate antimicrobial immunity compared with *Ddx3x* conditional knockout female mice (Szappanos et al., 2018). These findings highlight the fact that DDX3X and DDX3Y have roles beyond the reproductive system and suggest that *Ddx3x* and *Ddx3y* possibly have distinct functions in immune cells (Szappanos et al., 2018). Indeed, recently compiled proteomic databases show that both DDX3X and DDX3Y proteins are expressed in the human immune system, including in T cells, B cells, and NK cells (Bryk and Wisniewski, 2017; Joshi et al., 2019). Moreover, previous studies revealed that the DDX3Y protein is present in the enteric nervous system and the human heart (Cardinal et al., 2020; Godfrey et al., 2020; Vakilian et al., 2015). Still, potential functional differences between DDX3X and DDX3Y and their contributions to sex-biased human diseases are largely unknown.

Like other DEAD-box helicases, DDX3X and DDX3Y contain a helicase core composed of two RecA-like domains and one intrinsically disordered region (IDR) on each of the N and C termini. IDRs are frequently involved in the process of LLPS, driven by weak multivalent interactions (Figure 1A). Although DDX3X and DDX3Y share 92% amino acid sequence identity overall, the N-terminal IDRs (IDR1) are more divergent,

Please cite this article in press as: Shen et al., Sexually dimorphic RNA helicases DDX3X and DDX3Y differentially regulate RNA metabolism through phase separation, Molecular Cell (2022), https://doi.org/10.1016/j.molcel.2022.04.022

CellPress

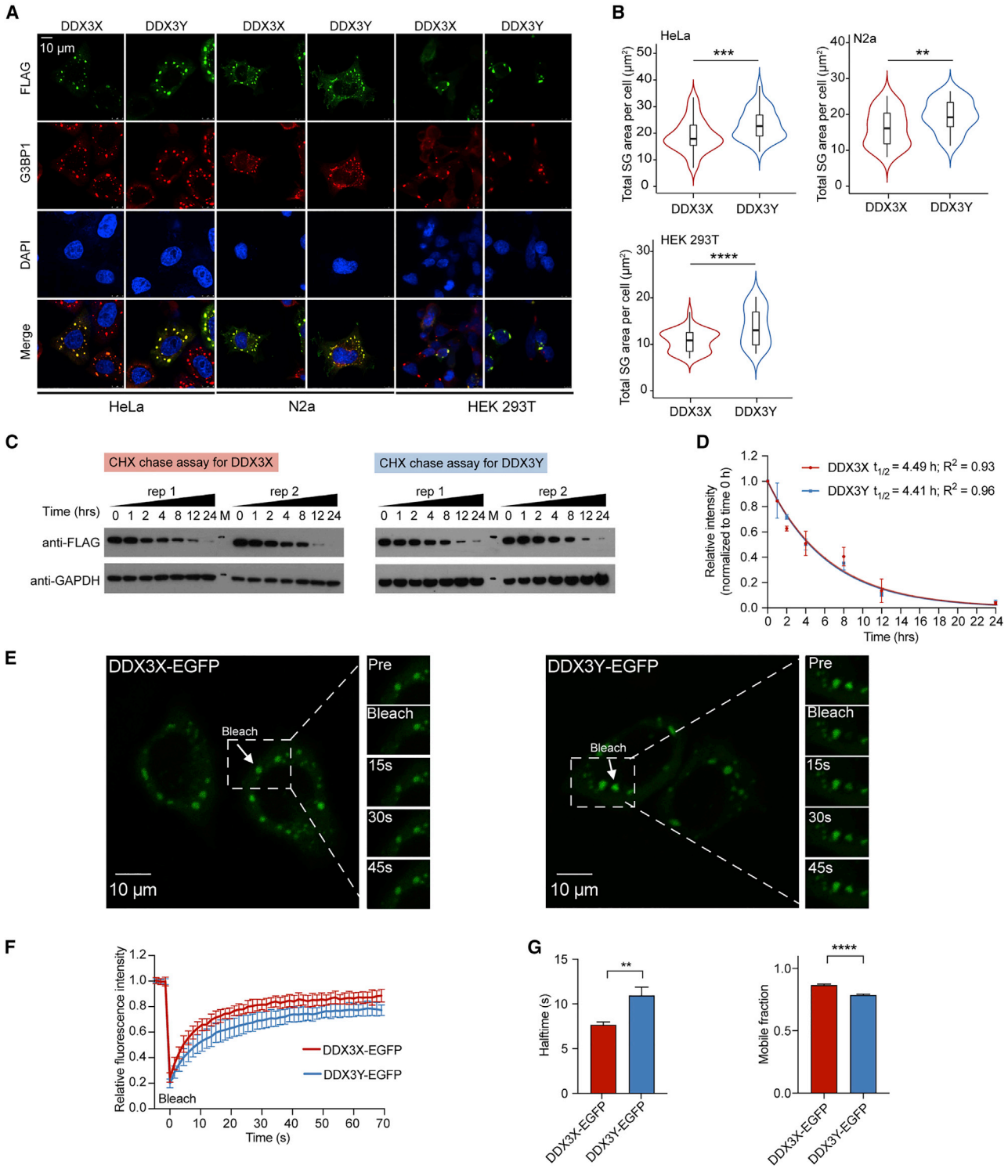

Figure 2. DDX3Y has a stronger LLPS propensity compared with DDX3X in cells

(A) Representative images of colocalization of DDX3X and DDX3Y with G3BP1 in HeLa, N2a, and HEK293T cells with the endogenous DDX3X knocked down upon arsenite treatment (500 μM, 1 h). Scale bars, 10 μm.

(B) Violin plots of the total SG area of DDX3X- or DDX3Y-positive SGs per cell across 50 cells upon arsenite treatment (500 μM, 1 h) in endogenous DDX3X-depleted HeLa, N2a, or HEK293T cells (n = 50 cells in total, from three biologically independent experiments). p values were determined by a two-tailed t test; **p < 0.01, ***p < 0.001, ****p < 0.0001.

(legend continued on next page)

Please cite this article in press as: Shen et al., Sexually dimorphic RNA helicases DDX3X and DDX3Y differentially regulate RNA metabolism through phase separation, Molecular Cell (2022), https://doi.org/10.1016/j.molcel.2022.04.022

accounting for 60% difference between DDX3X and DDX3Y (Figures S1A and S1B). IDR1 of DDX3X specifically is known to be essential for its LLPS *in vitro* and inside cells (Saito et al., 2019; Shih et al., 2012). Since many of the differences between the sequences of DDX3X and DDX3Y are concentrated in IDR1, we wondered whether DDX3X and DDX3Y differ in their propensity to LLPS and consequently differ in responding to cellular stress.

Here, we show that DDX3Y has a greater LLPS propensity than DDX3X. DDX3Y-positive SGs are less dynamic (less able to exchange particles with the light phase) than DDX3X-positive SGs. Furthermore, we demonstrate that although DDX3X- and DDX3Y-positive SGs share a large overlap of RNA constituents, there are also RNA components that are unique to either SG. We also show that the condensation of either DDX3X or DDX3Y represses the translation of RNAs, with DDX3Y condensation showing a significantly stronger inhibitory effect. Additionally, we show that both helicases specifically augment the aggregation of fused in sarcoma (FUS) *in vitro* and in cells, with DDX3Y having a more profound effect. Collectively, our results suggest that these sexually dimorphic RNA helicases differentially regulate RNA metabolism through their distinct biochemical and biophysical properties, which might contribute to sex bias in human diseases.

RESULTS

DDX3Y has a stronger propensity than DDX3X for *in vitro* and cellular phase separation

Given that DDX3X is known to undergo LLPS *in vitro*, we wanted to establish whether DDX3Y could also phase separate and how it compares with DDX3X. Thus, we purified mCherry-tagged full-length DDX3X and DDX3Y to near homogeneity (Figures S1C and S1D). Full-length mCherry-tagged DDX3X and DDX3Y formed noticeable droplets *in vitro*, and the addition of poly(U)-RNA greatly stimulated this process (Figures 1B and 1C). Strikingly, DDX3Y phase separation was more strongly enhanced by the addition of poly(U)-RNA than DDX3X *in vitro*; the average integrated fluorescence intensity of DDX3Y droplets was ~10-fold higher than that of an equal amount of DDX3X (Figures 1B and 1C). As shown in Figure S1E, RNase treatment had no influence on the *in vitro* droplet formation, indicating negligible RNA carry-over during protein purification. Furthermore, we determined the saturation concentration (C_{sat}) of DDX3X and DDX3Y using sedimentation analysis. The C_{sat} of DDX3X was ~5 μM whereas that of DDX3Y was ~3 μM, indicating that DDX3Y undergoes LLPS at lower concentrations than DDX3X (Figure 1D). In parallel, we performed a turbidity assay; the results consistently showed that DDX3Y gave substantially higher turbidity at the same total protein concentrations, compared with DDX3X (Figure 1E), suggesting a greater degree of phase separation.

We next studied the dynamics of DDX3X and DDX3Y droplets using fluorescence recovery after photobleaching (FRAP). The recovery half-time for DDX3X droplets was ~21.9 s, which was significantly faster than the ~83.4 s for DDX3Y droplets (Figures 1F, 1G, and S1F; Videos S1, S2, S3, and S4). Also, we observed a larger mobile fraction for DDX3X droplets (~99%) than for DDX3Y droplets (~78%) (Figure 1H). These results demonstrate that DDX3X is less prone to phase separation and that DDX3X droplets are more dynamic than DDX3Y droplets *in vitro*.

To assess if DDX3Y enters cellular SGs, we expressed DDX3X or DDX3Y in several mammalian cell types, each of which lacks endogenous DDX3Y (HeLa, N2a, and HEK293T cells). Before expressing either protein, we performed a transient knockdown of endogenous DDX3X with >80% knockdown efficiency (Figure S2A). Exogenous expressions of DDX3X and DDX3Y were at a similar level (Figures S2B and S2C). DDX3X and DDX3Y were diffused throughout the cytoplasm in unstressed HeLa cells (Figure S2D). Upon arsenite treatment (a commonly used oxidative stress inducer [Markmiller et al., 2018; Protter and Parker, 2016]), both DDX3X and DDX3Y colocalized with the SG marker G3BP1 (Markmiller et al., 2018; Figure 2A). Strikingly, the total area of DDX3Y-positive SGs was larger than that of DDX3X-positive SGs in HeLa cells (1.6-fold), N2a cells (1.3-fold), and HEK293T cells (1.7-fold) (Figure 2B). To control for possible differences in protein concentrations, we expressed DDX3X and DDX3Y across a range of concentrations in HeLa cells with endogenous DDX3X depleted. The results consistently showed that DDX3Y-positive granules were significantly larger than DDX3X-positive granules at similar expressed concentrations (Figures S2E–S2G). Additionally, we quantified the protein half-life of DDX3X and DDX3Y in HeLa cells using cycloheximide (CHX) chase experiments. As shown in Figures 2C and 2D, the cellular half-life of DDX3X is indistinguishable from DDX3Y. FRAP experiments performed on live HeLa cells expressing DDX3X-EGFP or DDX3Y-EGFP (Figure S2H) reveal that the average recovery half-time of DDX3X-positive granules was ~7.6 s, which was significantly faster than the ~10.2 s measured for DDX3Y-positive SGs (Figures 2E–2G; Videos S5 and S6). Additionally, a larger mobile fraction was observed in DDX3X-positive SGs (86%) than in DDX3Y-positive SGs (77%) (Figure 2G), consistent with our *in vitro* FRAP experiments. These results together suggest that DDX3X-positive SGs are more dynamic than DDX3Y-positive SGs.

(C) Cycloheximide (CHX) chase assay to determine the cellular half-life of DDX3X and DDX3Y in HeLa cells. Two biological replicates for DDX3X and for DDX3Y were performed. "M" represents the protein ladder on the western blot membranes (markers: upper 75 kDa, lower 37 kDa).
(D) Quantification of the protein levels in (C). The intensity of each DDX3X and DDX3Y band was normalized to the corresponding glyceraldehyde-3-phosphate dehydrogenase (GAPDH) intensity before being normalized to the intensity at the corresponding 0 h time point. The half-lives of DDX3X and DDX3Y were 4.49 and 4.41 h, respectively.
(E) Time-lapse images of photobleached SGs in HeLa cells expressing DDX3X-EGFP (left) or DDX3Y-EGFP (right) from in-cell FRAP experiments. The photobleaching events and fluorescence recovery by DDX3X-EGFP- and DDX3Y-EGFP-positive SGs are highlighted by the arrow in each outlined box.
(F) FRAP curves for DDX3X-EGFP (red) and DDX3Y-EGFP (blue) in HeLa cells. The trace of the FRAP data represents mean ± SEM (n = 20 independent measurements, from three biologically independent experiments).
(G) The half-time and mobile fractions in (E) and (F). A two-tailed t test was used to calculate the p value. $^{**}p < 0.01$, $^{****}p < 0.0001$.
See also Figure S2.

Please cite this article in press as: Shen et al., Sexually dimorphic RNA helicases DDX3X and DDX3Y differentially regulate RNA metabolism through phase separation, Molecular Cell (2022), https://doi.org/10.1016/j.molcel.2022.04.022

IDR1 is a major contributor to the higher phase separation propensity of DDX3Y

We constructed several truncated variants of DDX3X and DDX3Y to study the effect of each domain on SG partitioning (Figures S3A and S3B). Deletion of IDR1 from DDX3X (DDX3X$^{\Delta IDR1}$) and DDX3Y (DDX3Y$^{\Delta IDR1}$) led to the sequestration of the variants into cell nuclei and thus completely prevented either protein from entering cytoplasmic SGs, which is consistent with previous work showing that IDR1 of DDX3X contains a nuclear export sequence (Yedavalli et al., 2004; Figures S1A and S3C). Both DDX3X$^{\Delta IDR1}$ and DDX3Y$^{\Delta IDR1}$ were diffused in the nucleus, even with arsenite treatment (Figure S3C), so we hypothesized that the high nuclear RNA concentrations prevented these truncations from forming condensates, since this phenomenon has been seen with other RNA binding proteins with IDRs (Maharana et al., 2018). To test this, we treated cells expressing DDX3X$^{\Delta IDR1}$ or DDX3Y$^{\Delta IDR1}$ with actinomycin D (ActD), which inhibits transcription and thus decreases RNA levels. ActD treatment led to the formation of DDX3X and DDX3Y puncta inside the nucleus, consistent with an RNA-dependent LLPS buffering mechanism (Figure S3D).

Deleting any individual domain in DDX3X and DDX3Y dramatically decreased SG area, compared with the full-length (Figures 3A, 3B, S3A, and S3B). Consistent with previous results, IDR1 of either DDX3X or DDX3Y as a stand-alone protein entered SGs and colocalized with G3BP1. Furthermore, a noticeable fraction of IDR1 from either protein remained diffused throughout the cytoplasm upon arsenite treatment, indicating that IDR1 alone is less prone to enter SGs. For DDX3X, the deletion of IDR2 (DDX3X$^{\Delta IDR2}$) significantly decreased the total SG area of DDX3X$^{\Delta IDR2}$-positive SGs per cell (by ~1.4-fold) compared with the wild-type DDX3X SGs. Deletion of the helicase domains (both DEAD1 and DEAD2) from DDX3X also decreased the total area of DDX3X$^{\Delta helicase}$ SGs (~1.2-fold) per cell, but to a lesser extent than the deletion of IDR1 or IDR2. Similarly, for DDX3Y, deletion of IDR2 or the helicase domains both led to a ~1.2-fold decrease in the size of DDX3Y$^{\Delta IDR2}$-positive or DDX3Y$^{\Delta helicase}$-positive SGs, compared with the full-length DDX3Y SGs. Notably, the total SG area for each DDX3Y truncation was still larger than their DDX3X truncation counterparts (~1.3- to 1.85-fold), suggesting that subtle sequence variation throughout the protein contributes to the distinct behaviors of DDX3X and DDX3Y (Figures 3A and 3B).

When we swapped IDRs between DDX3X and DDX3Y, we observed that any domain-swapped variants containing IDR1 of DDX3Y formed significantly larger SGs than the hybrid variants that did not contain IDR1 of DDX3Y, whereas swapping helicase domains or IDR2 did not significantly affect SG sizes (Figures 3C, 3D, S3E, and S3F). When we performed *in vitro* droplet formation assays with wild-type and domain-swapped variants (which were purified to a similar level of homogeneity; Figures S3G and S3H), our results recapitulated the finding that any domain-swapped variants that contained IDR1 of DDX3Y more readily phase separated in the presence of RNA than variants that did not contain IDR1 of DDX3Y (Figures 3E and 3F). Our results further suggest that the IDR2 and helicase domains may also contribute to the differences in propensity to undergo LLPS, as the X^{IDR1}Y^{helicase}Y^{IDR2} variant more readily formed droplets, compared with wild-type DDX3X, X^{IDR1}Y^{helicase}X^{IDR2}, and X^{IDR1}X^{helicase}Y^{IDR2} (Figures 3D and 3F). To dissect the contributions of RNA binding and IDRs in phase separation of the proteins, we next performed the *in vitro* droplet assays with wild-type and domain-swapped variants in the absence of poly(U)-RNA. As shown in Figure S3I, proteins containing IDR1 of DDX3Y formed larger droplets than proteins containing IDR1 of DDX3X. These results suggest that although each of the domains in DDX3 proteins plays a distinct role in facilitating LLPS and in their accumulation into SGs, the sequence of IDR1 is a significant factor in determining the relative droplet sizes.

The weaker ATPase activity of DDX3Y compared with DDX3X weakens its condensate disassembly

DDX3X and DDX3Y harness the energy of ATP hydrolysis to control RNA binding, unwinding, and release (Hondele et al., 2019). Because LLPS droplets assemble through many multivalent, weak interactions between RNAs and proteins (Wang et al., 2018a), we stimulated the ATPase activity of DDX3X and DDX3Y to see if this could induce condensate disassembly by affecting protein-RNA interactions. As shown in Figures 4A and 4B, the addition of 4 mM ATP to protein-RNA droplets induced the disassembly of both DDX3X and DDX3Y condensates. To control the hydrotropic effect of ATP (Patel et al., 2017) in dissolving the droplets, we repeated the droplet assay using UTP (which is not hydrolyzed by DDX3 and thus could only act as a hydrotrope in this context; Patel et al., 2017). The addition of UTP had no significant effect on the droplets formed by DDX3X and DDX3Y with RNA (Figures 4A and 4B). These results suggest that the ATPase activity of DDX3X and DDX3Y is a major factor in dissolving DDX3-RNA condensation, possibly by breaking the multivalent protein-RNA interactions.

We next studied whether there are intrinsic differences in ATPase activity between DDX3X and DDX3Y, as this could explain the differences observed in their condensate disassembly in response to ATP. Thus, we measured the ATPase activities of both DDX3X and DDX3Y using a malachite green ATPase assay. In this assay, we used maltose-binding protein (MBP)-tagged proteins purified to near homogeneity (Figures S4A and S4B). Both of the MBP-tagged DDX3X and DDX3Y displayed the same melting temperatures in differential scanning fluorimetry measurements, and the melting curves are indicative of well-folded proteins devoid of aggregates (Figures S4C and S4D; Gao et al., 2020).

To ensure that any potential RNA carry-over would not confound our measurements, we performed the malachite green ATPase assays in the absence of additional RNA or with 100 ng/μL total HeLa RNA. In reactions with no added RNA but with 2 mM ATP, DDX3X and DDX3Y reactions had nearly identical amounts of free phosphate after a 30-min reaction time (Figure S4E). This phosphate is likely due to the spontaneous hydrolysis of ATP, as it is also present in the controls with buffer only. When RNA was added, DDX3X reactions produced more free phosphates (indicative of more ATP hydrolysis) than DDX3Y reactions. The malachite green ATPase assays were also performed using RNase-treated and -untreated MBP-tagged DDX3X and DDX3Y, respectively. As shown in Figure S4F, RNase treatment has no noticeable effects on the

Please cite this article in press as: Shen et al., Sexually dimorphic RNA helicases DDX3X and DDX3Y differentially regulate RNA metabolism through phase separation, Molecular Cell (2022), https://doi.org/10.1016/j.molcel.2022.04.022

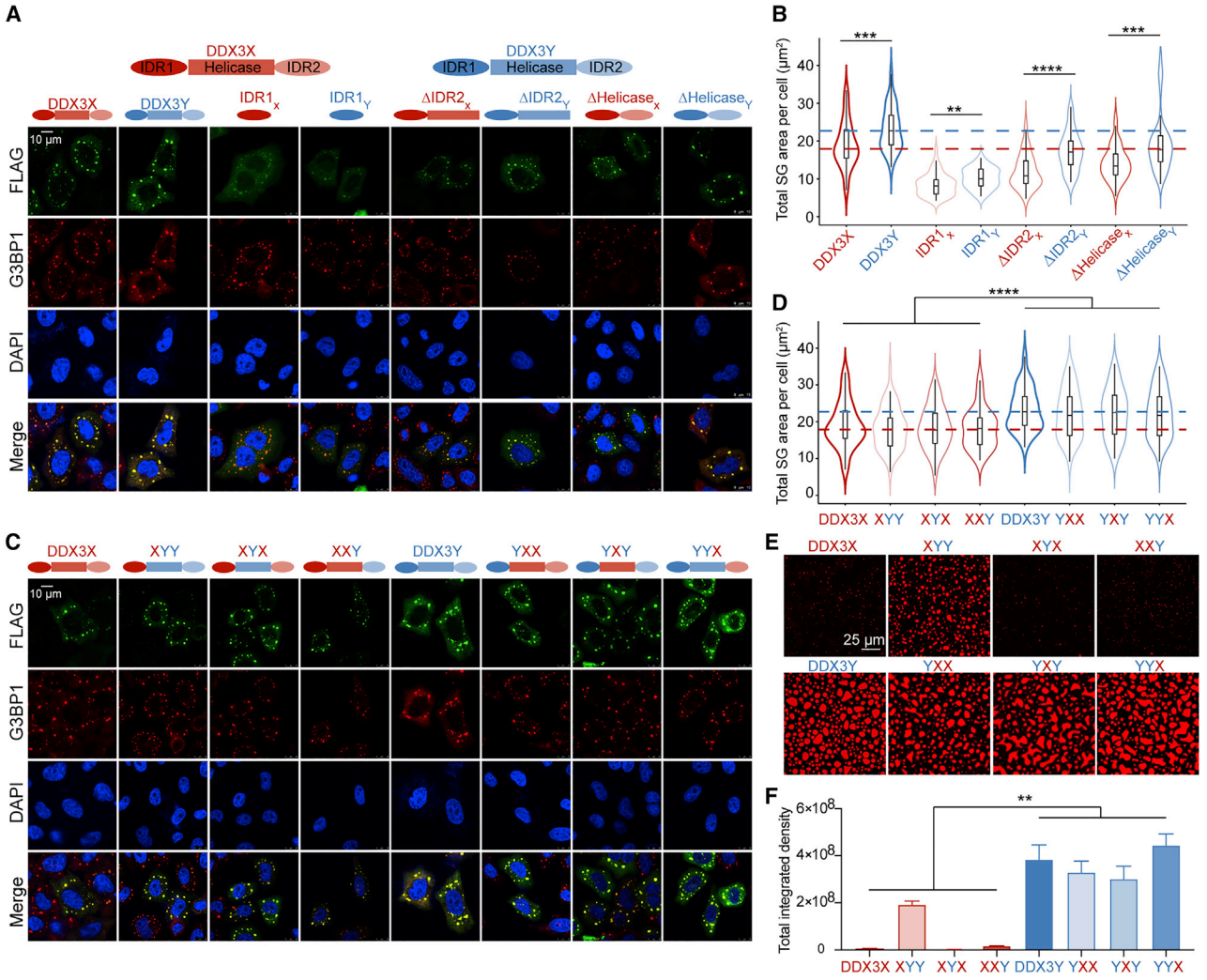

Figure 3. IDR1 of DDX3Y more strongly promotes phase separation than IDR1 of DDX3X

(A) Colocalization of DDX3X or DDX3Y domain truncation variants in HeLa cells with G3BP1 upon 500 μM arsenite treatment for 1 h. Scale bars, 10 μm.

(B) Violin plots of the total SG area of truncation SGs per cell (n = 50 cells in total, from three biologically independent experiments). The median of the total SG areas per cell of wild-type DDX3X SGs and DDX3Y SGs are indicated by red and blue dashed lines, respectively. p values were determined by a two-tailed t test; $^{**}p < 0.01$, $^{***}p < 0.001$, $^{****}p < 0.0001$.

(C) Colocalization of DDX3X or DDX3Y domain-swapped variants in HeLa cells with G3BP1 upon 500 μM arsenite treatment for 1 h. Scale bars, 10 μm.

(D) Violin plots of the total SG area of DDX3X or DDX3Y domain swap SGs per cell (50 cells in total from three biologically independent experiments). The median sum of SG areas per cell of wild-type DDX3X SGs and DDX3Y SGs is indicated by red and blue dashed lines, respectively. p values were determined by nested t test to compare all domain-swapped variants with X^{IDR1} versus all domain-swapped variants with Y^{IDR1}; $^{****}p < 0.0001$.

(E) *In vitro* droplet formation of 7.5 μM recombinant DDX3X-mCherry, DDX3Y-mCherry, or domain-swapped variants of DDX3X and DDX3Y in the presence of 200 ng/μL poly(U)-RNA. Scale bars, 25 μm.

(F) Quantification of the total integrated intensity of the different conditions shown in (E). Error bars represent SD from three repeats at each condition. p values were determined by nested t test to compare all domain-swapped variants with X^{IDR1} versus all domain-swapped variants with Y^{IDR1}; $^{**}p < 0.01$.

See also Figure S3.

ATPase activities. Collectively, these results suggest that DDX3X is a more robust ATPase than DDX3Y, and that the possible trace amount of RNA carry-over in the purified MBP-tagged DDX3X and DDX3Y was not responsible for the ATPase activity differences.

To obtain a more complete picture of the ATPase differences between DDX3X and DDX3Y, we performed a continuous ATPase assay, as previously reported, using the MBP-tagged DDX3X and DDX3Y constructs (Song and Ji, 2019). DDX3X reached a V_{max} of 7.9 μM/min, whereas DDX3Y only achieved a V_{max} of 5.9 μM/min (Figure 4C). Both DDX3X and DDX3Y hydrolyzed ATP cooperatively (Hill coefficient ≈ 2), as has been previously reported for DDX3X (Song and Ji, 2019). Whereas the ATPase activity of DDX3Y has not been previously investigated, our V_{max} values for the full-length DDX3X were higher than those reported for a truncation lacking both IDRs (amino

Please cite this article in press as: Shen et al., Sexually dimorphic RNA helicases DDX3X and DDX3Y differentially regulate RNA metabolism through phase separation, Molecular Cell (2022), https://doi.org/10.1016/j.molcel.2022.04.022

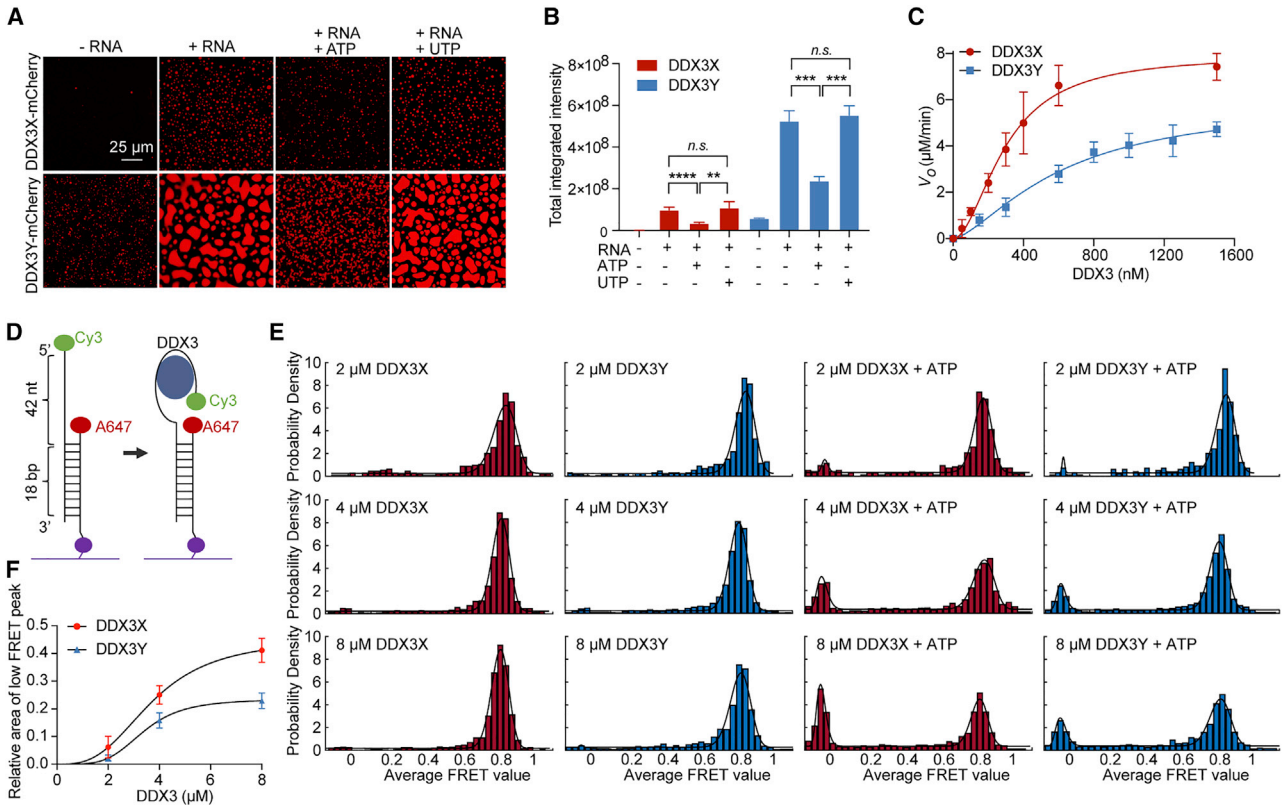

Figure 4. The weaker ATPase activity of DDX3Y, compared with DDX3X, weakens its condensate disassembly

(A) *In vitro* droplet formation of 10 μM recombinant DDX3X-mCherry and DDX3Y-mCherry in the absence and presence of 200 ng/μL poly(U)-RNA with and without the addition of 4 mM ATP or UTP. Scale bars, 25 μm.

(B) Quantification of the total integrated intensity of different groups of condensates shown in (A). A two-tailed t test was used to calculate the p value. n.s. means $p > 0.05$, $^{**}p < 0.01$, $^{***}p < 0.001$, and $^{****}p < 0.0001$.

(C) ATPase activity of DDX3X and DDX3Y, as measured by release of free phosphate, in μM/min. Error bars represent ± SD from six individual replicates. The background value (initial rate when no protein was added) was subtracted from each point before plotting and curve fitting to the Hill equation. DDX3X: V_{max} = 7.9 ± 0.4 μM/min, H = 1.9 ± 0.2, $K_{1/2}$ = 297.2 ± 22.6 nM. DDX3Y: V_{max} = 5.9 ± 0.7 μM/min, H = 1.5 ± 0.2, $K_{1/2}$ = 617.9 ± 123.6 nM. All fitting parameter uncertainties are ±SEM.

(D) Schematic of smFRET RNA probe.

(E) FRET efficiency distributions with increasing protein concentrations (2, 4, and 8 μM) of DDX3X and DDX3Y in the presence or absence of ATP. FRET values were collected from over 1,000 molecules to build the histograms.

(F) Fitting of the Hill equation to relative values of the low-FRET peak area (with background subtracted) in (E) for DDX3X and DDX3Y.

See also Figure S4.

acids 132–607) (7.9 versus 3.1 μM/min, 2.54-fold higher) (Song and Ji, 2019). Our data suggest that ATP hydrolysis activity of DDX3Y is significantly slower than that of DDX3X (Figure 4C).

DDX3X is a non-processive helicase: it binds its dsRNA substrate, binds ATP, unwinds approximately 13–19 bp of dsRNA, and releases the two RNA strands upon ATP hydrolysis (Song and Ji, 2019). Given that ATP hydrolysis is a crucial step in this catalytic cycle and that our ATPase data suggest that DDX3X is a more efficient ATPase than DDX3Y, we next investigated how the differences in ATPase activities may affect the dynamics of these enzymes. To this end, we employed single-molecule FRET (smFRET) assays with MBP-DDX3X and MBP-DDX3Y to compare their RNA binding abilities and the dynamics of their ATP-dependent interactions with RNA as described previously (Figure 4D; Kim and Myong, 2016). At protein concentrations of 2, 4, or 8 μM, DDX3X and DDX3Y tightly bound the RNA substrate, resulting in high FRET, with a peak FRET efficiency (*E*) of 0.81–0.85 (Figures 4E and S4G; Table S1). This binding is specific to DDX3X and DDX3Y, as MBP (a non-RNA interacting protein) gave low FRET, like RNA alone (Figures S4H and S4I).

The addition of ATP to DDX3X and DDX3Y led to a low-FRET population that was larger for DDX3X than it was for DDX3Y (Figures 4E, S4J, and S4K; Table S1). Of note, this low-FRET population of RNA molecules does not represent full strand separation of the RNA duplex because alternating direct illumination of the Cy3 and Alexa Fluor 647 probes (lowest traces in Figures S4J and S4K) showed that both labeled strands are present in each individual high- and low-FRET particles. This change in FRET from high to low efficiency likely represents partial unwinding activity. As shown in Figure 4F, the relative areas of the low-FRET peak, induced by addition of ATP, increased along with increasing protein concentrations,

Please cite this article in press as: Shen et al., Sexually dimorphic RNA helicases DDX3X and DDX3Y differentially regulate RNA metabolism through phase separation, Molecular Cell (2022), https://doi.org/10.1016/j.molcel.2022.04.022

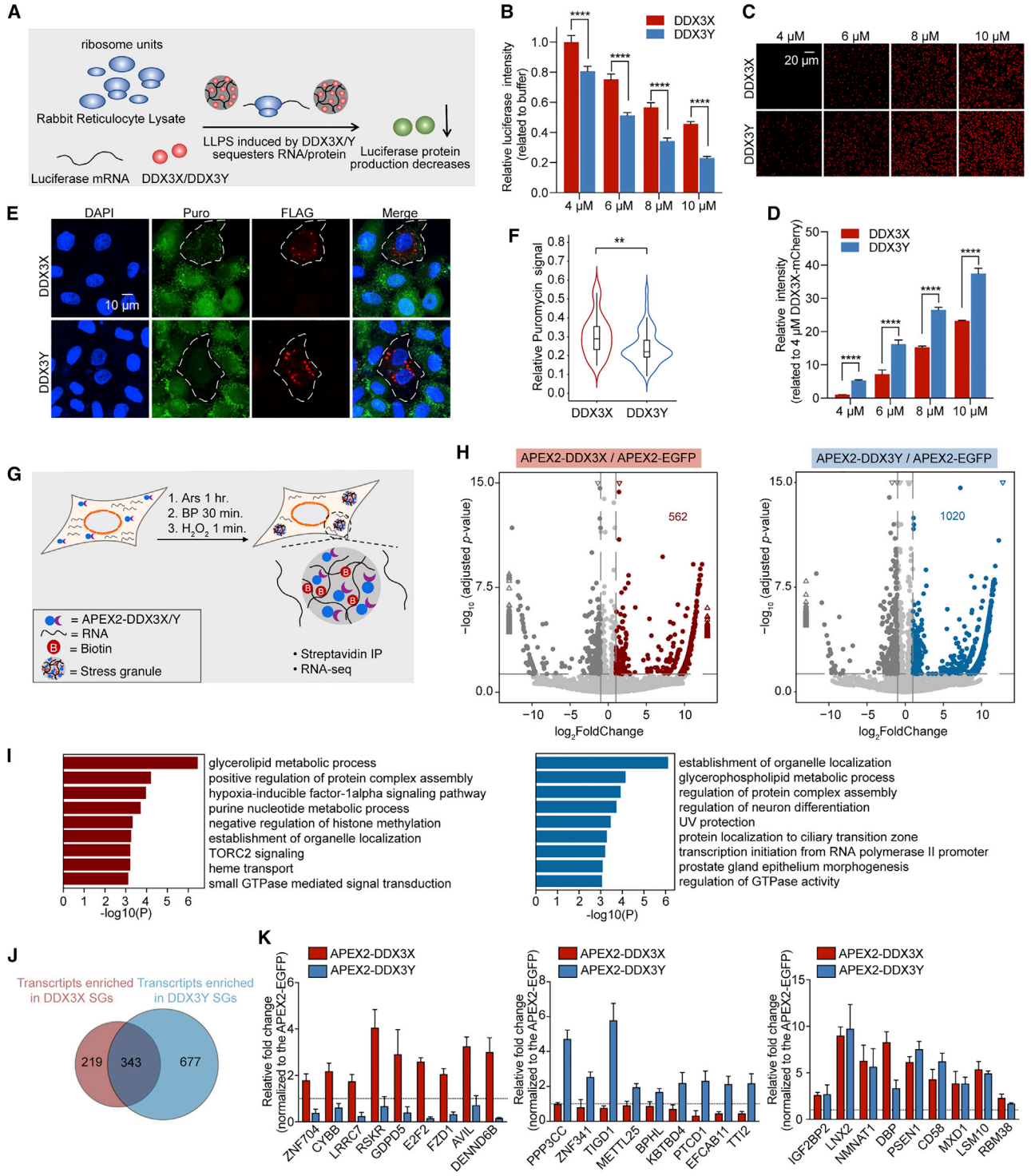

Figure 5. DDX3X and DDX3Y condensation inhibit the translation of luciferase RNA, and DDX3X- and DDX3Y-positive SGs have shared and unique RNA constituents in cells

(A) Schematic illustration of the *in vitro* translation assay.

(B) *In vitro* translation inhibition at the indicated concentrations of DDX3X-mCherry or DDX3Y-mCherry. p values were determined by two-tailed t test; ****p < 0.0001.

(C) DDX3X-mCherry and DDX3Y-mCherry phase separation in the reticulocyte assay at each indicated concentration. Scale bars, 20 μm.

(D) Quantification of the total integrated intensity of different condensates shown in (C).

(legend continued on next page)

Please cite this article in press as: Shen et al., Sexually dimorphic RNA helicases DDX3X and DDX3Y differentially regulate RNA metabolism through phase separation, Molecular Cell (2022), https://doi.org/10.1016/j.molcel.2022.04.022

which exemplifies the cooperativity of the DDX3X- and DDX3Y-catalyzed reactions. Importantly, the smFRET histograms suggest that DDX3X had higher (partial) unwinding activity than DDX3Y, consistent with the kinetics data (Figure 4C). DDX3X also showed a larger proportion of dynamic FRET recordings upon addition of ATP than DDX3Y (Figure S4L). Together, the kinetics and smFRET data support the conclusion that DDX3Y has slower ATPase and (partial) unwinding activities, leading to the less dynamic characteristics of RNA-DDX3Y complexes. Decreased dynamics may contribute to the weaker disassembly of DDX3Y condensates compared with those of DDX3X, which in turn contributes to the observation that DDX3Y condensates persist in the presence of ATP to a greater degree than DDX3X condensates (Figure 4A).

Translation is differentially modulated by DDX3X and DDX3Y

Given that SGs are formed concomitant with translational repression and are thought to harbor proteins that regulate translation (Kimball et al., 2003), we employed a reticulocyte *in vitro* translation assay to investigate how phase-separated DDX3X and DDX3Y influence the translation of a luciferase reporter (Figure 5A). Upon titration of 4–10 μM mCherry-DDX3X or mCherry-DDX3Y into the lysate, there was a dramatic, dose-dependent decrease of luciferase signal with increased concentrations of DDX3X or DDX3Y, indicating a decrease in the *in vitro* translation (Figure 5B). Indeed, we observed a concentration-dependent increase in protein condensation of DDX3X or DDX3Y within the lysate (Figures 5C and 5D). These results indicate that the condensation of DDX3X and DDX3Y is correlated with repressed mRNA translation. Of note, at each concentration tested, DDX3Y induced a more pronounced decrease in luciferase signal compared with DDX3X (Figure 5B). To ensure that the observed effects were specific to DDX3X and DDX3Y, we also titrated truncated versions of DDX3X and DDX3Y, which only contained the minimally active helicase domain (both RecA-like domains and the N- and C-terminal extensions) (Floor et al., 2016; Song and Ji, 2019) to serve as negative controls. As shown in Figure S5A, the luciferase signal remained steady across all concentrations of the truncated versions of DDX3X and DDX3Y, likely because these constructs lack IDRs. We next studied whether adding ATP could alleviate translation repression by disassembling the DDX3X and DDX3Y condensates in the *in vitro* translation assays. To this end, the assays were repeated with the addition of 1 mM ATP. Upon ATP addition, *in vitro* translation was partially restored in both DDX3X and DDX3Y reactions; however, DDX3Y reactions remained less translationally active than the corresponding DDX3X reactions (Figure S5B). These findings support the notion that the decreased ATPase activity of DDX3Y decelerates the dispersal of DDX3Y-containing condensates, and thus ATP does not fully restore *in vitro* translation.

Next, we investigated whether DDX3Y condensation had a stronger translation repression impact than DDX3Y condensation in cells, using a puromycin incorporation assay in HeLa cells after transient transfection of FLAG-DDX3X or FLAG-DDX3Y with endogenous DDX3X depleted. Puromycin was incorporated into newly synthesized proteins, and as shown in Figures 5E and 5F, the formation of DDX3X- and DDX3Y-positive SGs significantly reduced puromycin signals, compared with the neighboring cells which were not transfected and thus lacked DDX3X-positive or DDX3Y-positive SGs. Notably, the puromycin signals were weaker in cells with DDX3Y-positive SGs than in cells with DDX3X-positive SGs (Figure 5F). These results suggest a potential mechanism by which DDX3Y more effectively inhibit translation through its unique biophysical properties. Phase separation can inhibit translation by sequestering translational machinery and/or mRNA transcripts into the phase-separated compartment (Kim et al., 2019). DDX3Y-containing condensates and SGs are larger and less mobile (Figures 1 and 2), which may result in stronger translation inhibition than the smaller and more dynamic DDX3X condensates that exchange material more rapidly.

APEX-seq captures the protein-RNA interaction patterns of DDX3X and DDX3Y

SGs that are formed under different stress conditions contain distinct proteins and RNA constituents (Markmiller et al., 2018), raising the possibility that SG contents vary based on the type of stress presented to a cell. Neither the RNA composition nor the differential effects that DDX3X or DDX3Y may exert on resident SG RNAs are known. Since SGs are largely thought to be a mechanism for regulating mRNA metabolism (Buchan and Parker, 2009; Jain et al., 2016; Khong et al., 2017), we sought to define the RNA content of DDX3X- and DDX3Y-positive SGs.

(E) Puromycin incorporation assay to determine the extent of translation repression in cells with DDX3X- and DDX3Y-positive SGs. The white outlines indicate the cells that express exogenous DDX3X or DDX3Y.
(F) Quantification of puromycin signal in (E). Only cells expressing exogenous DDX3X or DDX3Y were selected, and the total puromycin signal in each cell was quantified. The total puromycin signals in neighboring cells not expressing exogenous DDX3X or DDX3Y were quantified similarly and used to normalize the data. p value was determined by two-tailed t test; $^{**}p < 0.01$.
(G) Schematic illustration of APEX2-mediated proximity labeling reaction.
(H) Volcano plots showing differential RNA enrichment in streptavidin pull-downs from APEX2-DDX3X-expressing cells (left) and APEX2-DDX3Y-expressing cells (right) compared with APEX2-EGFP-expressing cells after 500 μM arsenite treatment for 1 h. Differentially expressed genes are shown in red and blue for APEX2-DDX3X-enriched and APEX2-DDX3Y-enriched RNAs, respectively (adjusted $p < 0.05$, $\log_2$-fold change > 1) and dark gray for APEX2-DDX3X-depleted and APEX2-DDX3Y-depleted RNAs (adjusted $p < 0.05$, $\log_2$-fold change < −1). The rest of the RNAs are shown in light gray for both DDX3X and DDX3Y. The triangles represent the transcripts with $\log_2$-fold change > 13 or $\log_2$-fold change < −13 in the x axis; $-\log_{10}$ adjusted p > 15 in the y axis.
(I) Gene ontology (GO) analysis of the differentially enriched RNA groups in (E); red: APEX2-DDX3X-enriched RNAs; and blue: APEX2-DDX3Y-enriched mRNAs.
(J) Venn diagram quantifying the overlapping and distinct RNA clients enriched by APEX2-DDX3X and APEX2-DDX3Y after arsenite treatment.
(K) Relative fold change of select RNAs used to conduct qRT-PCR validation of the sequencing results.
See also Figure S5.

Please cite this article in press as: Shen et al., Sexually dimorphic RNA helicases DDX3X and DDX3Y differentially regulate RNA metabolism through phase separation, Molecular Cell (2022), https://doi.org/10.1016/j.molcel.2022.04.022

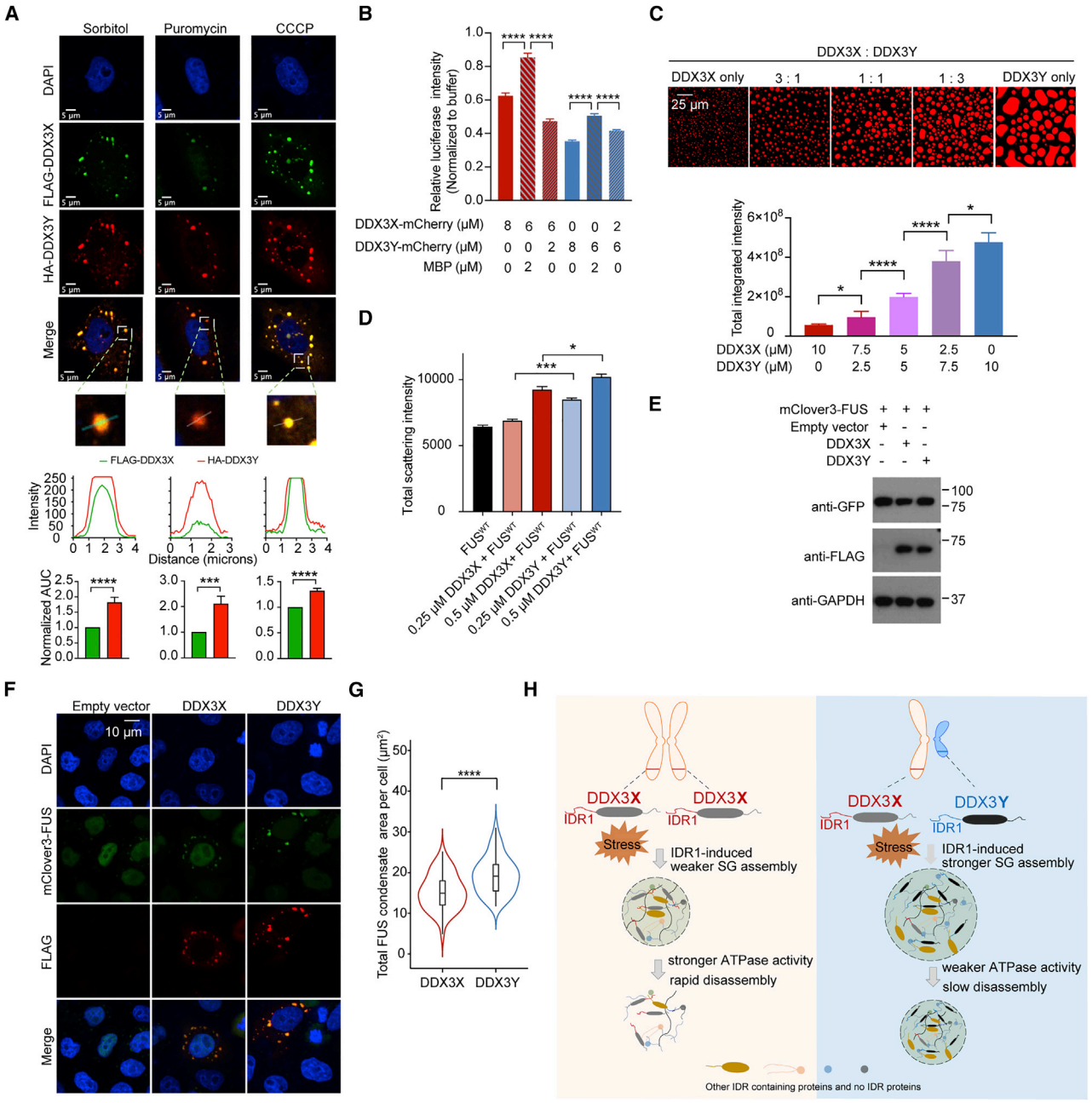

Figure 6. A combination of DDX3X and DDX3Y shows a stronger propensity of LLPS and translation repression than DDX3X alone; and DDX3Y enhances FUS aggregation and accelerates TAR DNA-binding protein 43 (TDP-43) aggregation more than DDX3X

(A) Immunofluorescence images of SGs containing both FLAG-DDX3X and HA-DDX3Y in HeLa cells treated with sorbitol, puromycin, or CCCP. Below each image, traces of fluorescence intensity profiles through positions denoted by the white lines in the merged images. The area under the curve (AUC) normalized to that of FLAG-DDX3X is plotted for each intensity profile and shows that the signal from HA-DDX3Y is consistently higher than the signal from FLAG-DDX3X.

(B) A mixture of DDX3X-mCherry and DDX3Y-mCherry at the annotated concentrations differentially repress *in vitro* translation of luciferase RNA. Overall, DDX3Y represses translation more than DDX3X. p values were determined by two-tailed t test; ****$p < 0.0001$.

(C) *In vitro* droplet formation of recombinant DDX3X-mCherry and DDX3Y-mCherry at the annotated ratios in the presence of 200 ng/μL poly(U)-RNA (top panel). Scale bars, 25 μm. Quantification of the total integrated intensity of each type of condensate (bottom panel). p values were determined by two-tailed t test; *$p < 0.05$, ****$p < 0.0001$.

(D) DDX3Y more strongly promotes FUS aggregation than DDX3X *in vitro*. The area under the curve for each time course of light scattering at 395 nm in Figure S6E was used to compare the extent of aggregation for each condition. p values were determined by two-tailed t test; *$p < 0.05$, ***$p < 0.001$.

(E) Western blots showing the expression of DDX3X and DDX3Y in DOX-inducible stable cell lines expressing mClover3-FUS.

(F) Representative images showing the localization of FLAG-DDX3X, FLAG-DDX3Y, and mClover-FUS upon arsenite treatment (500 μm, 1 h). Scale bars, 10 μm.

(legend continued on next page)

Please cite this article in press as: Shen et al., Sexually dimorphic RNA helicases DDX3X and DDX3Y differentially regulate RNA metabolism through phase separation, Molecular Cell (2022), https://doi.org/10.1016/j.molcel.2022.04.022

To this end, we employed an adapted ascorbate-peroxidase (APEX2)-based proximity labeling method (Fazal et al., 2019; Marmor-Kollet et al., 2020; Padrón et al., 2019; Figure S5C). First, to examine the specificity of APEX2-catalyzed RNA biotinylation, we generated a mito-APEX2 fusion protein consisting of APEX2 fused to a mitochondrial matrix localization signal (Figure S5D; Fazal et al., 2019; Mercer et al., 2011). Using a previously described protocol (Fazal et al., 2019), followed by qRT-PCR analysis, we could reliably identify mitochondrial-specific RNAs (ND1 and ND2) labeled by mito-APEX2 (Figures S5E–S5G).

Next, using this validated approach, we expressed APEX2-DDX3X, APEX2-DDX3Y, or APEX2-EGFP (control) in DDX3X knockdown HeLa cells. Cells were then treated with arsenite or DMSO for 1 h to generate three experimental cell populations. We consistently observed that the total area of APEX2-DDX3Y-positive SGs was significantly larger (1.5-fold) than that of APEX2-DDX3X-positive SGs (Figures S5H and S5I). The results suggest that the fusion of APEX2 to DDX3X or DDX3Y did not significantly interfere with the ability of either protein to colocalize with SGs in cells upon arsenite treatment.

The above cells were then incubated with biotin-phenol for 30 min, followed by H_2O_2 treatment for 1 min to activate the APEX2 enzyme and covalently link biotin to RNAs (Figure 5G). To confirm biotinylating, small aliquots of cell lysate for each condition were blotted using a streptavidin antibody; this antibody detected multiple protein bands (consistent with the previous results; Fazal et al., 2019), confirming that the APEX2 enzyme was active (Figures S5J and S5K). Subsequently, we performed biotin pull-down and poly(dT) extraction to enrich biotinylated poly(A)-RNAs. Enriched RNAs were subjected to next-generation high-throughput RNA-seq. The RNA-seq data from the biological replicates in each group correlated well (Figure S5L).

To determine whether DDX3X- and DDX3Y-positive SGs harbor unique mRNAs, we compared the transcript levels of APEX2-DDX3X or APEX2-DDX3Y libraries with that of APEX2-EGFP libraries. Any transcript for which expression in either the APEX2-DDX3X or APEX2-DDX3Y libraries was at least 2-fold higher than in the APEX2-EGFP dataset ($\log_2$-fold enrichment >1) was defined as ''enriched.'' We found that DDX3X-positive SGs enriched 562 RNAs (Figure 5H; Table S2), and gene ontology (GO) analysis indicated the encoded proteins were mainly involved in the regulation of glycolipid and nucleic acid metabolism (Figure 5I). DDX3Y-positive SGs enriched 1,020 RNAs (Figure 5H); GO analysis suggested that some of the encoded proteins were also involved in the regulation of glycolipid metabolism, whereas others played a role in transcriptional regulation (Figure 5I). Interestingly, although there was a large pool of RNAs enriched in both DDX3X- and DDX3Y-positive SGs (where 61% and 34% of DDX3X- and DDX3Y-positive SG-enriched RNAs, respectively, are shared), there were also RNA targets that were specific to each helicase (Figure 5J). In the absence of arsenite treatment, there was a small number of transcripts with fold change $\log_2 > 1$ or $\log_2 < -1$ in APEX2-DDX3X or APEX2-DDX3Y, compared with APEX2-EGFP (Figures S5H and S5M). We validated a list of RNA targets specifically enriched by either APEX2-DDX3X or APEX2-DDX3Y, ranging from lower to upper enrichment, using qRT-PCR (Figure 5K). These results indicate that DDX3X- and DDX3Y-positive SGs regulate distinct mRNA targets. However, DDX3X and DDX3Y may act on shared transcripts in divergent ways, as these two enzymes inhibit translation to different degrees (Figures 5A–5F).

DDX3X and DDX3Y co-phase separate into SGs

Whereas our study, up to this point, has focused on either DDX3X or DDX3Y individually, XY individuals express both proteins simultaneously (Cotton et al., 2015; Ditton et al., 2004; Godfrey et al., 2020). To examine whether DDX3X and DDX3Y go into the same SGs, we expressed DDX3X and DDX3Y together in cells with endogenous DDX3X transiently knocked down. We found that all the antibodies we tested were highly cross-reactive (Figure S6A), likely due to the high similarity of these two proteins. Thus, we used proteins with different tags (FLAG versus HA), and tagged homologs were expressed to a similar extent (Figure S6B).

Given that SG size and composition are sensitive to different types of stressors (Fujimura et al., 2012; Markmiller et al., 2018; Saito et al., 2019; Szaflarski et al., 2016), we studied SGs triggered by a range of stressors, including energy depletion (carbonyl cyanide 3-chlorophenyl hydrazone, CCCP), osmotic stress (sorbitol), translation inhibition (puromycin), proteasome inhibition (MG132), and ER stress (thapsigargin). Under these conditions, MG132 and thapsigargin did not induce SG formation (Figure S6C). However, when CCCP, sorbitol, or puromycin was used to stress cells, DDX3X, DDX3Y, and G3BP1 colocalize, although the fluorescence intensity of FLAG-DDX3X was much lower than that of HA-DDX3Y (Figure 6A). To ensure that our observations were not due to differential recognition by the anti-FLAG and anti-HA antibodies, we repeated the experiments using HA-DDX3X and FLAG-DDX3Y. We observed the same lower intensity of DDX3X, even though total protein levels for each DDX3 homolog were similar and not affected by either tag (Figure S6D). These results suggest that, although DDX3X and DDX3Y phase separate to SGs together, DDX3Y has a stronger propensity to go into SGs than DDX3X, in line with our previous observations.

Given that DDX3X and DDX3Y can co-phase separate into SGs, we wondered how mixtures of DDX3X and DDX3Y affected translation compared with DDX3X or DDX3Y alone. As shown in Figure 6B, a 3:1 ratio of DDX3X (6 μM) and DDX3Y (2 μM), which is close to the physiological ratios between DDX3X and DDX3Y (Godfrey et al., 2020), led to a 1.4-fold more robust repression of translation compared with DDX3X (8 μM) alone and a 3.6-fold more robust repression of translation compared with a mixture of DDX3X (6 μM) and MBP (2 μM). Moreover, a mixture

(G) The total area of granules containing mClover3-FUS and FLAG-DDX3X or granules containing mClover3-FUS and FLAG-DDX3Y per cell was quantified (n = 50 cells in total, from three biologically independent experiments). p values were determined by a two-tailed t test; ****$p < 0.0001$.
(H) Schematic illustration of how sexually dimorphic RNA helicases DDX3X and DDX3Y differentially regulate RNA translation through phase separation.
See also Figure S6.

Please cite this article in press as: Shen et al., Sexually dimorphic RNA helicases DDX3X and DDX3Y differentially regulate RNA metabolism through phase separation, Molecular Cell (2022), https://doi.org/10.1016/j.molcel.2022.04.022

of DDX3X (2 μM) and DDX3Y (6 μM) less efficiently repressed translation relative to DDX3Y (8 μM) alone. Furthermore, the *in vitro* LLPS assays were performed with different ratios of DDX3X and DDX3Y in the presence of RNA. The addition of DDX3Y to DDX3X stimulated droplet formation, and condensation was positively correlated with the relative amount of DDX3Y (Figure 6C).

DDX3Y more strongly promotes FUS aggregation than DDX3X does

Dysregulation of SGs can promote FUS aggregation, leading to cell death (Bentmann et al., 2012; Guo et al., 2018; Kamelgarn et al., 2016; Silva et al., 2019). Thus, we studied how DDX3X and DDX3Y influence *in vitro* FUS fibrillization. When we added 1 μM wild-type FUS to either DDX3X or DDX3Y, we saw that the aggregation of FUS, detected by light scattering at 395 nm, was enhanced by both helicases but was more extensively aggravated in the presence of DDX3Y (Figure S6E). To quantify the effect of DDX3X and DDX3Y on FUS aggregation over time, we measured the area under the curve (AUC) for each scattering time course. Both DDX3X and DDX3Y enhanced FUS aggregation, but DDX3Y had a stronger enhancement, even at high concentrations of either protein (Figures 6D and S6E). We also studied the colocalization of FUS and DDX3X or DDX3Y in HeLa cells upon arsenite treatment. We constructed a DOX-inducible stable cell line that expressed FUS. As shown in Figures 6E and 6F, whereas wild-type FUS was mainly located in the nucleus with transfection of empty vector, a portion of FUS formed puncta that colocalize with DDX3X-positive granules and DDX3Y-positive granules in the cytoplasm with transfection of DDX3X and DDX3Y expression plasmids. Furthermore, DDX3Y-FUS puncta were significantly larger than DDX3X-FUS puncta (Figure 6G). As XY individuals are at a higher risk of developing ALS (Manjaly et al., 2010), these data not only suggest that DDX3X and DDX3Y affect FUS aggregation but also suggest that the enhanced propensity to promote LLPS by DDX3Y might lead to a XY-specific increase of FUS aggregation.

DDX3Y more strongly accelerates TDP-43 aggregation than DDX3X does

Finally, we tested whether DDX3X or DDX3Y might also stimulate the aggregation of TDP-43, another prominent RNA binding protein connected to ALS and frontal temporal dementia (FTD) (Portz et al., 2021; Tan et al., 2017). We found that DDX3X or DDX3Y did not enhance the total amount of TDP-43 aggregation (Figures S6F and S6G). However, both helicases accelerated TDP-43 aggregation (Figures S6F and S6H). The half-time $t_{1/2}$ (i.e., the time at which 50% TDP-43 aggregation had occurred) was reduced from ~6.9 h in the absence of helicase to ~5.7 h in the presence of DDX3X and ~4.4 h in the presence of DDX3Y (Figures S6F and S6H). These findings suggest that DDX3Y can accelerate TDP-43 aggregation more potently than DDX3X.

DISCUSSION

Herein, we report the first comparative study of the sexually dimorphic RNA helicases DDX3X and DDX3Y in the regulation of translation via distinct phase separation behaviors (Figure 6H). Importantly, we reveal the molecular mechanism underpinning the higher propensity of DDX3Y to phase separate and its lower propensity to disassemble once condensed. Firstly, we find that the condensation propensity differences of DDX3X and DDX3Y are most likely due to the sequence composition of both IDR1s. Overall, the percentages of both negatively and positively charged amino acids in Y^{IDR1} (17.3% and 16.1%, respectively) are higher than in X^{IDR1}(16.7% and 14.9%, respectively), whereas the percentage of charged amino acids is similar between the other domains of DDX3X and DDX3Y (Figure S6I). This finding suggests that Y^{IDR1} can form more charge-charge interactions to support phase separation. In addition to these electrostatic interactions, cation-π and π-π (Vernon et al., 2018) interactions are known to facilitate LLPS (Qamar et al., 2018). As such, Tyr to Phe and Arg to Lys mutations in IDRs dramatically impair phase separation (Schuster et al., 2020). In line with this, Phe84 and Lys118 in X^{IDR1} correspond to Tyr83 and Arg116 in Y^{IDR1}, suggesting that Y^{IDR1} is capable of more cation-π and π-π interactions than X^{IDR1}, which might result in the stronger phase separation of DDX3Y found in these studies (Figure S1A). Indeed, Lys118 in DDX3X is a known site of post-translational acetylation (Saito et al., 2019). Acetylation at this site decreases the phase separation of DDX3X *in vitro* and inside of cells through the disruption of cation-π interactions. Given that the analogous position in DDX3Y is an arginine (Arg116), which is often thought of as a ''non-acetyl'' mimetic, this position is likely a key source of difference between DDX3X and DDX3Y and merits future study.

Second, our data suggest that the distinct dynamics of DDX3X- and DDX3Y-positive SGs may also be related to differences in their ATPase-driven SG remodeling activity (Jain et al., 2016; Tauber et al., 2020; Figure 4). Furthermore, the differences in dynamics of DDX3X and DDX3Y condensates may also explain why DDX3Y more strongly repressed translation than DDX3X. DDX3X- and DDX3Y-positive SGs sequester distinct mRNAs in addition to a shared pool of transcripts, suggesting that the differences in ATPase activity and translational repression may have functional consequences, especially under stress (Figures 5G–5K). The results shared here suggest that DDX3X and DDX3Y might influence the translation of the overlapping mRNA targets to different degrees in addition to exerting differential regulation of distinct RNA components. They might also differentially sequester other translational components.

One important question that remains to be answered is the degree to which DDX3X and DDX3Y overlap functionally. Studies by others have suggested that DDX3X and DDX3Y are redundant in protein synthesis under unstressed conditions (Venkataramanan et al., 2021). Our data suggest that their divergent roles may not be apparent until they are driven to phase separate during the stress response.

Stress leads to various human disorders, many of which display sex-biased features. For instance, ALS is ~20% more common in males than females (Manjaly et al., 2010). We showed that DDX3Y more strongly promotes FUS self-assembly *in vitro* and formed larger FUS granules in cells (Figures 6D–6G), possibly through its stronger phase separation propensity, compared with DDX3X. Furthermore, DDX3Y more strongly

Please cite this article in press as: Shen et al., Sexually dimorphic RNA helicases DDX3X and DDX3Y differentially regulate RNA metabolism through phase separation, Molecular Cell (2022), https://doi.org/10.1016/j.molcel.2022.04.022

accelerated TDP-43 aggregation than DDX3X (Figures S6F–S6H). Other known SG resident proteins such as TIA-1, hnRNPA1, and hnRNPA2 have been previously indicated in ALS (Fernandes et al., 2020; Gilks et al., 2004; Harrison and Shorter, 2017; Khalfallah et al., 2018; Molliex et al., 2015). Future investigation on the scope and extent of DDX3X's and DDX3Y's impact on these proteins in sex specificity in neurodegenerative diseases will be intriguing.

Limitations of the study

HeLa cells may not be perfectly suited to the task of uncovering the biological targets in DDX3Y-specific SGs, because they lack a Y chromosome and thus may also lack some of the specific transcripts that may be targeted by DDX3Y. However, we feel that reconstituting HeLa cells (with endogenous DDX3X depleted) with ectopically expressed DDX3X or DDX3Y provided a clean system to reveal the different RNA sequestration impacts of DDX3X and DDX3Y due to their intrinsic differences in phase separation. Thus, we believe our findings are an excellent proof of principle. Additionally, even though our recombinant proteins were purified to apparent homogeneity and were not expected to have unequal carry-over of RNA, there could have been some effect of potential impurities on the magnitude of the differences we measured. However, we believe that the difference itself is a true observation about these proteins. The apparent unwinding activity observed in the smFRET assays is not an indication of complete unwinding by DDX3X/DDX3Y, and this assay is not a conventional assay to study helicase activity. Both the donor and acceptor fluorophores being present in all molecules compiled in the smFRET analysis indicates only partial unwinding of the RNA substrate. We believe our smFRET assay is mainly reflecting the ATPase and dynamic activity of the proteins with RNA and gives insight into the differences between DDX3X and DDX3Y in these features. Our experiments should therefore serve as a crucial first step toward understanding the role of sexually dimorphic proteins in disease.

STAR★METHODS

Detailed methods are provided in the online version of this paper and include the following:

- KEY RESOURCES TABLE
- RESOURCE AVAILABILITY
  - Lead contact
  - Materials availability
  - Data and code availability
- EXPERIMENTAL MODEL AND SUBJECT DETAILS
  - Cell culture, transfection, and *Escherichia coli* strains
- METHOD DETAILS
  - Constructs
  - Protein purification
  - Differential scanning fluorimetry assay
  - *In vitro* LLPS assay
  - Immunofluorescence cell staining
  - Fluorescence recovery after photobleaching
  - Formation of stress granules in cells
  - Sequence alignment
  - Turbidity assay
  - Construction of DOX-inducible cell lines
  - Colocalization of DDX3X/Y with FUS in cells
  - Cycloheximide chase assay
  - Puromycin incorporation assay
  - Malachite green ATPase assay
  - Continuous ATPase assay
  - smFRET
  - RNA isolation
  - qRT-PCR
  - Cellular APEX labeling
  - Validation of APEX labeling
  - Purification and sequencing biotinylated RNA
  - Validation of the APEX labeling of RNA
  - High throughput data analysis
  - *In vitro* translation
  - FUS aggregation assay
  - TDP-43 aggregation assay
  - Protein quantification and western blot
- QUANTIFICATION AND STATISTICAL ANALYSIS

SUPPLEMENTAL INFORMATION

Supplemental information can be found online at https://doi.org/10.1016/j.molcel.2022.04.022.

ACKNOWLEDGMENTS

This work was supported by the National Institutes of Health (R35GM133721 to K.F.L.; R35GM133721-03S1 to A.Y.; T32GM132039 to A.Y., M.C.O., and K.E.C.; T32GM008275 and F31NS111870 to C.M.F.; R01GM099836, R21AG061784, and R21AG065854 to J.S.; and R35GM118139 to Y.E.G.). K.F.L. is supported by the American Cancer Society (RSG-22-064-01-RMC). J.S. is supported by grants from Target ALS, the Amyotrophic Lateral Sclerosis Association, the Office of the Assistant Secretary of Defense for Health Affairs through the Amyotrophic Lateral Sclerosis Research Program (W81XWH-20-1-0242), the G. Harold and Leila Y. Mathers Foundation, and Sanofi. We thank Dr. Bede Portz for the pMAL-c2X-DDX3X plasmid, Kollin Schultz for his help with DSF experiments, Dr. Matthew Kayser for sharing the Leica SP8 confocal microscope, Dr. Brian Capell for sharing the Nextseq550 sequencer, Dr. Karsten Weis for sharing the pKW4557 (DDX3X-mCherry) plasmid, and Dr. Ophir Shalem for sharing the plasmid expressing mClover3-FUS and mClover3-TDP-43 with us. We also thank Drs. Ronen Marmorstein, Hillary Nelson, Gregory Van Duyne, and Kristen Lynch for their constructive discussions and for editing this manuscript.

AUTHOR CONTRIBUTIONS

H.S. and K.F.L. designed the experiments. H.S. and K.F.L. processed the APEX-seq data. H.S., A.Y., M.C.O., and C.Z. generated the constructs and the mammalian cell lines used in this study. H.S., A.Y., and C.Z. purified the recombinant DDX3X and DDX3Y (full-length proteins and the truncation variants) used in this study. H.S. and A.Y. performed the immunofluorescence imaging experiments and analyzed the data. A.Y., M.C.O., and C.Z. performed the ATPase activity assays. C.M.F. performed FUS aggregation assays, and K.E.C. performed TDP-43 aggregation assays with suggestions from J.S. A.Y. and C.F. performed the smFRET studies under the direction of Y.E.G. H.S., M.C.O., and A.Y. wrote the manuscript together with K.F.L. All authors participated in the discussion and editing of the manuscript.

DECLARATION OF INTERESTS

J.S. is a consultant for Dewpoint Therapeutics, Confluence Therapeutics, Korro Bio, Neumora, and ADRx.

Received: September 13, 2021
Revised: April 9, 2022
Accepted: April 19, 2022
Published: May 18, 2022

REFERENCES

Ash, P.E., Vanderweyde, T.E., Youmans, K.L., Apicco, D.J., and Wolozin, B. (2014). Pathological stress granules in Alzheimer's disease. Brain Res. *1584*, 52–58.

Baradaran-Heravi, Y., Van Broeckhoven, C., and van der Zee, J. (2020). Stress granule mediated protein aggregation and underlying gene defects in the FTD-ALS spectrum. Neurobiol. Dis. *134*, 104639.

Beckham, C., Hilliker, A., Cziko, A.M., Noueiry, A., Ramaswami, M., and Parker, R. (2008). The DEAD-box RNA helicase Ded1p affects and accumulates in *Saccharomyces cerevisiae* P-bodies. Mol. Biol. Cell *19*, 984–993.

Bellott, D.W., Hughes, J.F., Skaletsky, H., Brown, L.G., Pyntikova, T., Cho, T.J., Koutseva, N., Zaghlul, S., Graves, T., Rock, S., et al. (2014). Mammalian Y chromosomes retain widely expressed dosage-sensitive regulators. Nature *508*, 494–499.

Bentmann, E., Neumann, M., Tahirovic, S., Rodde, R., Dormann, D., and Haass, C. (2012). Requirements for stress granule recruitment of fused in sarcoma (FUS) and TAR DNA-binding protein of 43 kDa (TDP-43). J. Biol. Chem. *287*, 23079–23094.

Bolger, A.M., Lohse, M., and Usadel, B. (2014). Trimmomatic: a flexible trimmer for Illumina sequence data. Bioinformatics *30*, 2114–2120.

Bryk, A.H., and Wiśniewski, J.R. (2017). Quantitative analysis of human red blood cell proteome. J. Proteome Res. *16*, 2752–2761.

Buchan, J.R., and Parker, R. (2009). Eukaryotic stress granules: the ins and outs of translation. Mol. Cell *36*, 932–941.

Cardinal, T., Bergeron, K.F., Soret, R., Souchkova, O., Faure, C., Guillon, A., and Pilon, N. (2020). Male-biased aganglionic megacolon in the TashT mouse model of Hirschsprung disease involves upregulation of p53 protein activity and Ddx3y gene expression. PLoS Genet. *16*, e1009008.

Chen, C.Y., Chan, C.H., Chen, C.M., Tsai, Y.S., Tsai, T.Y., Wu Lee, Y.H., and You, L.R. (2016). Targeted inactivation of murine Ddx3x: essential roles of Ddx3x in placentation and embryogenesis. Hum. Mol. Genet. *25*, 2905–2922.

Cheng, W., Wang, S., Zhang, Z., Morgens, D.W., Hayes, L.R., Lee, S., Portz, B., Xie, Y., Nguyen, B.V., Haney, M.S., et al. (2019). CRISPR-Cas9 screens identify the RNA helicase DDX3X as a repressor of C9ORF72 (GGGGCC)n repeat-associated non-AUG translation. Neuron *104*, 885–898.e8.

Cotton, A.M., Price, E.M., Jones, M.J., Balaton, B.P., Kobor, M.S., and Brown, C.J. (2015). Landscape of DNA methylation on the X chromosome reflects CpG density, functional chromatin state and X-chromosome inactivation. Hum. Mol. Genet. *24*, 1528–1539.

Ditton, H.J., Zimmer, J., Kamp, C., Rajpert-De Meyts, E., and Vogt, P.H. (2004). The AZFa gene DBY (DDX3Y) is widely transcribed but the protein is limited to the male germ cells by translation control. Hum. Mol. Genet. *13*, 2333–2341.

Elbaum-Garfinkle, S., Kim, Y., Szczepaniak, K., Chen, C.C., Eckmann, C.R., Myong, S., and Brangwynne, C.P. (2015). The disordered P granule protein LAF-1 drives phase separation into droplets with tunable viscosity and dynamics. Proc. Natl. Acad. Sci. USA *112*, 7189–7194.

Fazal, F.M., Han, S., Parker, K.R., Kaewsapsak, P., Xu, J., Boettiger, A.N., Chang, H.Y., and Ting, A.Y. (2019). Atlas of subcellular RNA localization revealed by APEX-Seq. Cell *178*, 473–490.e26.

Fernandes, N., Nero, L., Lyons, S.M., Ivanov, P., Mittelmeier, T.M., Bolger, T.A., and Buchan, J.R. (2020). Stress granule assembly can facilitate but is not required for TDP-43 cytoplasmic aggregation. Biomolecules *10*, 1367.

Ferretti, M.T., Iulita, M.F., Cavedo, E., Chiesa, P.A., Schumacher Dimech, A., Santuccione Chadha, A., Baracchi, F., Girouard, H., Misoch, S., Giacobini, E., et al. (2018). Sex differences in Alzheimer disease - the gateway to precision medicine. Nat. Rev. Neurol. *14*, 457–469.

Floor, S.N., Condon, K.J., Sharma, D., Jankowsky, E., and Doudna, J.A. (2016). Autoinhibitory interdomain interactions and subfamily-specific extensions redefine the catalytic core of the human DEAD-box protein DDX3. J. Biol. Chem. *291*, 2412–2421.

Fujimura, K., Sasaki, A.T., and Anderson, P. (2012). Selenite targets eIF4E-binding protein-1 to inhibit translation initiation and induce the assembly of non-canonical stress granules. Nucleic Acids Res. *40*, 8099–8110.

Gao, K., Oerlemans, R., and Groves, M.R. (2020). Theory and applications of differential scanning fluorimetry in early-stage drug discovery. Biophys. Rev. *12*, 85–104.

Gilks, N., Kedersha, N., Ayodele, M., Shen, L., Stoecklin, G., Dember, L.M., and Anderson, P. (2004). Stress granule assembly is mediated by prion-like aggregation of TIA-1. Mol. Biol. Cell *15*, 5383–5398.

Godfrey, A.K., Naqvi, S., Chmátal, L., Chick, J.M., Mitchell, R.N., Gygi, S.P., Skaletsky, H., and Page, D.C. (2020). Quantitative analysis of Y-Chromosome gene expression across 36 human tissues. Genome Res. *30*, 860–873.

Gozdecka, M., Meduri, E., Mazan, M., Tzelepis, K., Dudek, M., Knights, A.J., Pardo, M., Yu, L., Choudhary, J.S., Metzakopian, E., et al. (2018). UTX-mediated enhancer and chromatin remodeling suppresses myeloid leukemogenesis through noncatalytic inverse regulation of ETS and GATA programs. Nat. Genet. *50*, 883–894.

Guo, L., Kim, H.J., Wang, H., Monaghan, J., Freyermuth, F., Sung, J.C., O'Donovan, K., Fare, C.M., Diaz, Z., Singh, N., et al. (2018). Nuclear-import receptors reverse aberrant phase transitions of RNA-binding proteins with prion-like domains. Cell *173*, 677–692.e20.

Hallegger, M., Chakrabarti, A.M., Lee, F.C.Y., Lee, B.L., Amalietti, A.G., Odeh, H.M., Copley, K.E., Rubien, J.D., Portz, B., Kuret, K., et al. (2021). TDP-43 condensation properties specify its RNA-binding and regulatory repertoire. Cell *184*, 4680–4696.e22.

Harrison, A.F., and Shorter, J. (2017). RNA-binding proteins with prion-like domains in health and disease. Biochem. J. *474*, 1417–1438.

Hellenkamp, B., Schmid, S., Doroshenko, O., Opanasyuk, O., Kühnemuth, R., Rezaei Adariani, S., Ambrose, B., Aznauryan, M., Barth, A., Birkedal, V., et al. (2018). Precision and accuracy of single-molecule FRET measurements-a multi-laboratory benchmark study. Nat. Methods *15*, 669–676.

Hondele, M., Sachdev, R., Heinrich, S., Wang, J., Vallotton, P., Fontoura, B.M.A., and Weis, K. (2019). DEAD-box ATPases are global regulators of phase-separated organelles. Nature *573*, 144–148.

Iossifov, I., O'Roak, B.J., Sanders, S.J., Ronemus, M., Krumm, N., Levy, D., Stessman, H.A., Witherspoon, K.T., Vives, L., Patterson, K.E., et al. (2014). The contribution of de novo coding mutations to autism spectrum disorder. Nature *515*, 216–221.

Iserman, C., Desroches Altamirano, C., Jegers, C., Friedrich, U., Zarin, T., Fritsch, A.W., Mittasch, M., Domingues, A., Hersemann, L., Jahnel, M., et al. (2020). Condensation of Ded1p promotes a translational switch from housekeeping to stress protein production. Cell *181*, 818–831.e19.

Jain, S., Wheeler, J.R., Walters, R.W., Agrawal, A., Barsic, A., and Parker, R. (2016). ATPase-modulated stress granules contain a diverse proteome and substructure. Cell *164*, 487–498.

Jamiolkowski, R.M., Chen, C., Cooperman, B.S., and Goldman, Y.E. (2017). tRNA fluctuations observed on stalled ribosomes are suppressed during ongoing protein synthesis. Biophys. J. *113*, 2326–2335.

Joshi, R.N., Stadler, C., Lehmann, R., Lehtiö, J., Tegnér, J., Schmidt, A., and Vesterlund, M. (2019). TcellSubC: an atlas of the subcellular proteome of human T cells. Front. Immunol. *10*, 2708.

Kamelgarn, M., Chen, J., Kuang, L., Arenas, A., Zhai, J., Zhu, H., and Gal, J. (2016). Proteomic analysis of FUS interacting proteins provides insights into FUS function and its role in ALS. Biochim. Biophys. Acta *1862*, 2004–2014.

Khalfallah, Y., Kuta, R., Grasmuck, C., Prat, A., Durham, H.D., and Vande Velde, C.V. (2018). TDP-43 regulation of stress granule dynamics in neurodegenerative disease-relevant cell types. Sci. Rep. *8*, 7551.

Khong, A., Matheny, T., Jain, S., Mitchell, S.F., Wheeler, J.R., and Parker, R. (2017). The stress granule transcriptome reveals principles of mRNA accumulation in stress granules. Mol. Cell *68*, 808–820.e5.

Kim, D., Langmead, B., and Salzberg, S.L. (2015). HISAT: a fast spliced aligner with low memory requirements. Nat. Methods *12*, 357–360.

Kim, T.H., Tsang, B., Vernon, R.M., Sonenberg, N., Kay, L.E., and Forman-Kay, J.D. (2019). Phospho-dependent phase separation of FMRP and CAPRIN1 recapitulates regulation of translation and deadenylation. Science *365*, 825–829.

Kim, Y., and Myong, S. (2016). RNA remodeling activity of DEAD box proteins tuned by protein concentration, RNA length, and ATP. Mol. Cell *63*, 865–876.

Kimball, S.R., Horetsky, R.L., Ron, D., Jefferson, L.S., and Harding, H.P. (2003). Mammalian stress granules represent sites of accumulation of stalled translation initiation complexes. Am. J. Physiol. Cell Physiol. *284*, C273–C284.

Ku, Y.C., Lai, M.H., Lo, C.C., Cheng, Y.C., Qiu, J.T., Tarn, W.Y., and Lai, M.C. (2019). DDX3 participates in translational control of inflammation induced by infections and injuries. Mol. Cell. Biol. *39*. e00285–e00218.

Lai, M.C., Lee, Y.H., and Tarn, W.Y. (2008). The DEAD-box RNA helicase DDX3 associates with export messenger ribonucleoproteins as well as tip-associated protein and participates in translational control. Mol. Biol. Cell *19*, 3847–3858.

Lancaster, A.K., Nutter-Upham, A., Lindquist, S., and King, O.D. (2014). PLAAC: a web and command-line application to identify proteins with prion-like amino acid composition. Bioinformatics *30*, 2501–2502.

Lee, C.S., Dias, A.P., Jedrychowski, M., Patel, A.H., Hsu, J.L., and Reed, R. (2008). Human DDX3 functions in translation and interacts with the translation initiation factor eIF3. Nucleic Acids Res. *36*, 4708–4718.

Lennox, A.L., Hoye, M.L., Jiang, R., Johnson-Kerner, B.L., Suit, L.A., Venkataramanan, S., Sheehan, C.J., Alsina, F.C., Fregeau, B., Aldinger, K.A., et al. (2020). Pathogenic DDX3X mutations impair RNA metabolism and neurogenesis during fetal cortical development. Neuron *106*, 404–420.e8.

Liao, Y., Smyth, G.K., and Shi, W. (2014). featureCounts: an efficient general purpose program for assigning sequence reads to genomic features. Bioinformatics *30*, 923–930.

Linsalata, A.E., He, F., Malik, A.M., Glineburg, M.R., Green, K.M., Natla, S., Flores, B.N., Krans, A., Archbold, H.C., Fedak, S.J., et al. (2019). DDX3X and specific initiation factors modulate FMR1 repeat-associated non-AUG-initiated translation. EMBO Rep. *20*, e47498.

Love, M.I., Huber, W., and Anders, S. (2014). Moderated estimation of fold change and dispersion for RNA-seq data with DESeq2. Genome Biol. *15*, 550.

Maharana, S., Wang, J., Papadopoulos, D.K., Richter, D., Pozniakovsky, A., Poser, I., Bickle, M., Rizk, S., Guillén-Boixet, J., Franzmann, T.M., et al. (2018). RNA buffers the phase separation behavior of prion-like RNA binding proteins. Science *360*, 918–921.

Manjaly, Z.R., Scott, K.M., Abhinav, K., Wijesekera, L., Ganesalingam, J., Goldstein, L.H., Janssen, A., Dougherty, A., Willey, E., Stanton, B.R., et al. (2010). The sex ratio in amyotrophic lateral sclerosis: a population based study. Amyotroph. Lateral Scler. *11*, 439–442.

Markmiller, S., Soltanieh, S., Server, K.L., Mak, R., Jin, W., Fang, M.Y., Luo, E.C., Krach, F., Yang, D., Sen, A., et al. (2018). Context-dependent and disease-specific diversity in protein interactions within stress granules. Cell *172*, 590–604.e13.

Marmor-Kollet, H., Siany, A., Kedersha, N., Knafo, N., Rivkin, N., Danino, Y.M., Moens, T.G., Olender, T., Sheban, D., Cohen, N., et al. (2020). Spatiotemporal proteomic analysis of stress granule disassembly using APEX reveals regulation by SUMOylation and links to ALS pathogenesis. Mol. Cell *80*, 876–891.e6.

Mauvais-Jarvis, F., Bairey Merz, N., Barnes, P.J., Brinton, R.D., Carrero, J.J., DeMeo, D.L., De Vries, G.J., Epperson, C.N., Govindan, R., Klein, S.L., et al. (2020). Sex and gender: modifiers of health, disease, and medicine. Lancet *396*, 565–582.

McCombe, P.A., and Henderson, R.D. (2010). Effects of gender in amyotrophic lateral sclerosis. Gend. Med. *7*, 557–570.

Mercer, T.R., Neph, S., Dinger, M.E., Crawford, J., Smith, M.A., Shearwood, A.M., Haugen, E., Bracken, C.P., Rackham, O., Stamatoyannopoulos, J.A., et al. (2011). The human mitochondrial transcriptome. Cell *146*, 645–658.

Meyer, S., van der Meer, P., van Tintelen, J.P., and van den Berg, M.P. (2014). Sex differences in cardiomyopathies. Eur. J. Heart Fail. *16*, 238–247.

Mitchell, S.F., Jain, S., She, M., and Parker, R. (2013). Global analysis of yeast mRNPs. Nat. Struct. Mol. Biol. *20*, 127–133.

Molliex, A., Temirov, J., Lee, J., Coughlin, M., Kanagaraj, A.P., Kim, H.J., Mittag, T., and Taylor, J.P. (2015). Phase separation by low complexity domains promotes stress granule assembly and drives pathological fibrillization. Cell *163*, 123–133.

Moon, S.L., Morisaki, T., Khong, A., Lyon, K., Parker, R., and Stasevich, T.J. (2019). Multicolour single-molecule tracking of mRNA interactions with RNP granules. Nat. Cell Biol. *21*, 162–168.

Nguyen, T.A., Wu, K., Pandey, S., Lehr, A.W., Li, Y., Bemben, M.A., Badger, J.D., 2nd, Lauzon, J.L., Wang, T., Zaghloul, K.A., et al. (2020). A cluster of autism-associated variants on X-linked NLGN4X functionally resemble NLGN4Y. Neuron *106*, 759–768.e7.

Padrón, A., Iwasaki, S., and Ingolia, N.T. (2019). Proximity RNA labeling by APEX-seq reveals the organization of translation initiation complexes and repressive RNA granules. Mol. Cell *75*, 875–887.e5.

Patel, A., Malinovska, L., Saha, S., Wang, J., Alberti, S., Krishnan, Y., and Hyman, A.A. (2017). ATP as a biological hydrotrope. Science *356*, 753–756.

Patmore, D.M., Jassim, A., Nathan, E., Gilbertson, R.J., Tahan, D., Hoffmann, N., Tong, Y., Smith, K.S., Kanneganti, T.D., Suzuki, H., et al. (2020). DDX3X suppresses the susceptibility of hindbrain lineages to medulloblastoma. Dev. Cell *54*, 455–470.e5.

Phung, B., Cieśla, M., Sanna, A., Guzzi, N., Beneventi, G., Cao Thi Ngoc, P., Lauss, M., Cabrita, R., Cordero, E., Bosch, A., et al. (2019). The X-linked DDX3X RNA helicase dictates translation reprogramming and metastasis in melanoma. Cell Rep. *27*, 3573–3586.e7.

Portz, B., Lee, B.L., and Shorter, J. (2021). FUS and TDP-43 phases in health and disease. Trends Biochem. Sci. *46*, 550–563.

Protter, D.S.W., and Parker, R. (2016). Principles and properties of stress granules. Trends Cell Biol. *26*, 668–679.

Qamar, S., Wang, G.Z., Randle, S.J., Ruggeri, F.S., Varela, J.A., Lin, J.Q., Phillips, E.C., Miyashita, A., Williams, D., Ströhl, F., et al. (2018). FUS phase separation is modulated by a molecular chaperone and methylation of arginine cation-pi interactions. Cell *173*, 720–734.e15.

Robert, X., and Gouet, P. (2014). Deciphering key features in protein structures with the new ENDscript server. Nucleic Acids Res. *42*, W320–W324.

Ruzzo, E.K., Pérez-Cano, L., Jung, J.Y., Wang, L.K., Kashef-Haghighi, D., Hartl, C., Singh, C., Xu, J., Hoekstra, J.N., Leventhal, O., et al. (2019). Inherited and de novo genetic risk for autism impacts shared networks. Cell *178*, 850–866.e26.

Saito, M., Hess, D., Eglinger, J., Fritsch, A.W., Kreysing, M., Weinert, B.T., Choudhary, C., and Matthias, P. (2019). Acetylation of intrinsically disordered regions regulates phase separation. Nat. Chem. Biol. *15*, 51–61.

Scala, M., Torella, A., Severino, M., Morana, G., Castello, R., Accogli, A., Verrico, A., Vari, M.S., Cappuccio, G., Pinelli, M., et al. (2019). Three de novo DDX3X variants associated with distinctive brain developmental abnormalities and brain tumor in intellectually disabled females. Eur. J. Hum. Genet. *27*, 1254–1259.

Schindelin, J., Arganda-Carreras, I., Frise, E., Kaynig, V., Longair, M., Pietzsch, T., Preibisch, S., Rueden, C., Saalfeld, S., Schmid, B., et al. (2012). Fiji: an open-source platform for biological-image analysis. Nat. Methods *9*, 676–682.

Schneider, J.W., Oommen, S., Qureshi, M.Y., Goetsch, S.C., Pease, D.R., Sundsbak, R.S., Guo, W., Sun, M., Sun, H., Kuroyanagi, H., et al. (2020). Dysregulated ribonucleoprotein granules promote cardiomyopathy in RBM20 gene-edited pigs. Nat. Med. *26*, 1788–1800.

Schuster, B.S., Dignon, G.L., Tang, W.S., Kelley, F.M., Ranganath, A.K., Jahnke, C.N., Simpkins, A.G., Regy, R.M., Hammer, D.A., Good, M.C., et al. (2020). Identifying sequence perturbations to an intrinsically disordered

protein that determine its phase-separation behavior. Proc. Natl. Acad. Sci. USA *117*, 11421–11431.

Sharma, D., and Jankowsky, E. (2014). The Ded1/DDX3 subfamily of DEAD-box RNA helicases. Crit. Rev. Biochem. Mol. Biol. *49*, 343–360.

Shi, B., Li, W., Song, Y.S., Wang, Z.J., Ju, R., Ulman, A., Hu, J., Palomba, F., Zhao, Y.F., Le, J.P., et al. (2021). UTX condensation underlies its tumour-suppressive activity. Nature *597*, 726–731.

Shih, J.W., Wang, W.T., Tsai, T.Y., Kuo, C.Y., Li, H.K., and Wu Lee, Y.H. (2012). Critical roles of RNA helicase DDX3 and its interactions with eIF4E/PABP1 in stress granule assembly and stress response. Biochem. J. *441*, 119–129.

Silva, J.M., Rodrigues, S., Sampaio-Marques, B., Gomes, P., Neves-Carvalho, A., Dioli, C., Soares-Cunha, C., Mazuik, B.F., Takashima, A., Ludovico, P., et al. (2019). Dysregulation of autophagy and stress granule-related proteins in stress-driven Tau pathology. Cell Death Differ. *26*, 1411–1427.

Snijders Blok, L., Madsen, E., Juusola, J., Gilissen, C., Baralle, D., Reijnders, M.R., Venselaar, H., Helsmoortel, C., Cho, M.T., Hoischen, A., et al. (2015). Mutations in DDX3X are a common cause of unexplained intellectual disability with gender-specific effects on Wnt signaling. Am. J. Hum. Genet. *97*, 343–352.

Song, H., and Ji, X. (2019). The mechanism of RNA duplex recognition and unwinding by DEAD-box helicase DDX3X. Nat. Commun. *10*, 3085.

Soto-Rifo, R., Rubilar, P.S., Limousin, T., de Breyne, S., Décimo, D., and Ohlmann, T. (2012). DEAD-box protein DDX3 associates with eIF4F to promote translation of selected mRNAs. EMBO J. *31*, 3745–3756.

Sun, Z., Diaz, Z., Fang, X., Hart, M.P., Chesi, A., Shorter, J., and Gitler, A.D. (2011). Molecular determinants and genetic modifiers of aggregation and toxicity for the ALS disease protein FUS/TLS. PLoS Biol. *9*, e1000614.

Szaflarski, W., Fay, M.M., Kedersha, N., Zabel, M., Anderson, P., and Ivanov, P. (2016). Vinca alkaloid drugs promote stress-induced translational repression and stress granule formation. Oncotarget *7*, 30307–30322.

Szappanos, D., Tschismarov, R., Perlot, T., Westermayer, S., Fischer, K., Platanitis, E., Kallinger, F., Novatchkova, M., Lassnig, C., Müller, M., et al. (2018). The RNA helicase DDX3X is an essential mediator of innate antimicrobial immunity. PLoS Pathog. *14*, e1007397.

Tan, R.H., Ke, Y.D., Ittner, L.M., and Halliday, G.M. (2017). ALS/FTLD: experimental models and reality. Acta Neuropathol. *133*, 177–196.

Tauber, D., Tauber, G., Khong, A., Van Treeck, B., Pelletier, J., and Parker, R. (2020). Modulation of RNA condensation by the DEAD-box protein eIF4A. Cell *180*, 411–426.e16.

Vakilian, H., Mirzaei, M., Sharifi Tabar, M., Pooyan, P., Habibi Rezaee, L., Parker, L., Haynes, P.A., Gourabi, H., Baharvand, H., and Salekdeh, G.H. (2015). DDX3Y, a male-specific region of Y chromosome gene, may modulate neuronal differentiation. J. Proteome Res. *14*, 3474–3483.

Valentin-Vega, Y.A., Wang, Y.D., Parker, M., Patmore, D.M., Kanagaraj, A., Moore, J., Rusch, M., Finkelstein, D., Ellison, D.W., Gilbertson, R.J., et al. (2016). Cancer-associated DDX3X mutations drive stress granule assembly and impair global translation. Sci. Rep. *6*, 25996.

Venkataramanan, S., Gadek, M., Calviello, L., Wilkins, K., and Floor, S.N. (2021). DDX3X and DDX3Y are redundant in protein synthesis. RNA *27*, 1577–1588.

Vernon, R.M., Chong, P.A., Tsang, B., Kim, T.H., Bah, A., Farber, P., Lin, H., and Forman-Kay, J.D. (2018). Pi-Pi contacts are an overlooked protein feature relevant to phase separation. Elife *7*, e31486.

Walker, I.H., Hsieh, P.C., and Riggs, P.D. (2010). Mutations in maltose-binding protein that alter affinity and solubility properties. Appl. Microbiol. Biotechnol. *88*, 187–197.

Wang, J., Choi, J.M., Holehouse, A.S., Lee, H.O., Zhang, X., Jahnel, M., Maharana, S., Lemaitre, R., Pozniakovsky, A., Drechsel, D., et al. (2018a). A molecular grammar governing the driving forces for phase separation of prion-like RNA binding proteins. Cell *174*, 688–699.e16.

Wang, X., Posey, J.E., Rosenfeld, J.A., Bacino, C.A., Scaglia, F., Immken, L., Harris, J.M., Hickey, S.E., Mosher, T.M., Slavotinek, A., et al. (2018b). Phenotypic expansion in DDX3X—a common cause of intellectual disability in females. Ann. Clin. Transl. Neurol. *5*, 1277–1285.

Watkins, J., Ghosh, A., Keerie, A.F.A., Alix, J.J.P., Mead, R.J., and Sreedharan, J. (2020). Female sex mitigates motor and behavioural phenotypes in TDP-43(Q331K) knock-in mice. Sci. Rep. *10*, 19220.

Wu, T., Yu, J., Gale-Day, Z., Woo, A., Suresh, A., Hornsby, M., and Gestwicki, J.E. (2020). Three essential resources to improve differential scanning fluorimetry (DSF) experiments. Preprint at bioRxiv. https://doi.org/10.1101/2020.03.22.002543.

Xue, B., Dunbrack, R.L., Williams, R.W., Dunker, A.K., and Uversky, V.N. (2010). PONDR-FIT: a meta-predictor of intrinsically disordered amino acids. Biochim. Biophys. Acta *1804*, 996–1010.

Yedavalli, V.S.R.K., Neuveut, C., Chi, Y.H., Kleiman, L., and Jeang, K.T. (2004). Requirement of DDX3 DEAD box RNA helicase for HIV-1 Rev-RRE export function. Cell *119*, 381–392.

Zhou, Y., Zhou, B., Pache, L., Chang, M., Khodabakhshi, A.H., Tanaseichuk, O., Benner, C., and Chanda, S.K. (2019). Metascape provides a biologist-oriented resource for the analysis of systems-level datasets. Nat. Commun. *10*, 1523.

Please cite this article in press as: Shen et al., Sexually dimorphic RNA helicases DDX3X and DDX3Y differentially regulate RNA metabolism through phase separation, Molecular Cell (2022), https://doi.org/10.1016/j.molcel.2022.04.022

STAR★METHODS

KEY RESOURCES TABLE

REAGENT or RESOURCE	SOURCE	IDENTIFIER
Antibodies		
Rabbit polyclonal anti-G3BP1	Proteintech	Cat# 13057-2-AP, RRID:AB_2232034
Rabbit polyclonal anti-HA	Abcam	Cat# ab9110, RRID:AB_307019
Mouse monoclonal anti-FLAG	Sigma-Aldrich	Cat# F3165, RRID:AB_259529
Rat monoclonal anti-FLAG	Invitrogen	Cat# MA1-142, RRID:AB_2536846
HRP conjugated anti-FLAG	Invitrogen	Cat# MA1-91878-HRP, RRID:AB_2537626
Rabbit polyclonal anti-GAPDH	Invitrogen	Cat# PA1-16777, RRID:AB_568552
Mouse monoclonal anti-GFP	Santa Cruz	Cat# sc-996, RRID:AB_2187785
Mouse anti-puromycin, clone 12D10, Alexa Fluor 488 conjugated antibody	Sigma-Aldrich	Cat# MABE343-AF488, RRID:AB_2736875
Goat anti-mouse IgG (H&L) (HRP)	Abcam	Cat# ab6789, RRID:AB_955439
Mouse monoclonal anti-ATP5A	Abcam	Cat# ab14748, RRID:AB_301447
Goat anti-Mouse IgG H&L (Alex Fluor® 647)	Abcam	Cat# ab150115, RRID:AB_2687948
Goat anti-Rabbit IgG H&L (Alexa Fluor® 594)	Abcam	Cat# ab150080, RRID:AB_2650602
Goat anti-Mouse IgG H&L (Alexa Fluor® 488)	Abcam	Cat# ab150113, RRID:AB_2576208
Goat Anti-Rat IgG H&L (Alexa Fluor® 488)	Abcam	Cat# ab150157, RRID:AB_2722511
Mouse monoclonal anti-DDX3	Abcam	Cat# ab196032, RRID:AB_2910197
Rabbit polyclonal anti-DDX3Y	Invitrogen	Cat# PA5-90055, RRID:AB_2805908
Bacterial and virus strains		
One Shot™ TOP10 Chemically Competent *E. coli*	Invitrogen	Cat# 404003
BL21(DE3)-RIL Competent *E. coli*	Agilent	Cat# 230204
Chemicals, peptides, and recombinant proteins		
Streptavidin-HRP	Cell Signaling Technology	Cat# 3999, RRID:AB_10830897
DDX3X-mCherry recombinant protein	This paper	N/A
DDX3Y-mCherry recombinant protein	This paper	N/A
MBP-DDX3X recombinant protein	This paper	N/A
MBP-DDX3Y recombinant protein	This paper	N/A
N-Lauroylsarcosine sodium salt solution	Sigma-Aldrich	Cat# L7414-10ML
SUPERase•In™ RNase Inhibitor	Invitrogen	Cat# AM2694
Proteinase K solution (20 mg/mL)	Life Technologies	Cat# AM2548
Lipofectamine 2000	Thermo Fisher	Cat# 11668019
Pierce streptavidin magnetic beads	Thermo Fisher	Cat# 88816
Agencourt AMPure XP	Beckman Coulter	Cat# A63881
TRIzol	Invitrogen	Cat# 15596026
IPTG	Thermo Fisher	Cat# 34060
DAPI	Sigma-Aldrich	Cat# D9542
Fisher BioReagents™ Bovine Serum Albumin, Heat Shock Treated	Fisher Scientific	Cat# BP1600-100
Polyuridylic acid potassium salt	Sigma-Aldrich	Cat# P9528-10MG
Sodium arsenite	Spectrum Chemical	Cat# S-222
Sorbitol solution	Spectrum Chemical	Cat# S-1525
Thapsigargin	ACROS Organics	Cat# AC328570010
CCCP	Alfa Aesar	Cat# AAL06932MC
Puromycin	Takara Bio USA	Cat# 631305

(*Continued on next page*)

Please cite this article in press as: Shen et al., Sexually dimorphic RNA helicases DDX3X and DDX3Y differentially regulate RNA metabolism through phase separation, Molecular Cell (2022), https://doi.org/10.1016/j.molcel.2022.04.022

Continued

REAGENT or RESOURCE	SOURCE	IDENTIFIER
MG132	Sigma-Aldrich	Cat# 474790-1MG
Hydrogen peroxide solution	Sigma-Aldrich	Cat# H1009
Biotin-phenol	Iris Biotech	Cat# LS-3500.1000
Sodium azide	Sigma-Aldrich	Cat# S2002
Sodium ascorbate	Sigma-Aldrich	Cat# A7631
Trolox	Sigma-Aldrich	Cat# 238813
Cycloheximide	Sigma-Aldrich	Cat# C7698
Critical commercial assays		
Malachite Green Phosphate Assay Kit	Sigma-Aldrich	Cat# MAK307-1KT
Flexi® Rabbit Reticulocyte Lysate System	Promega	Cat# L4540
Luna® Universal One-Step RT-qPCR Kit	NEB	Cat# M3005L
Truseq Stranded mRNA Library Prep	Illumina	Cat# 20020594
Dynabeads™ mRNA Purification Kit (for mRNA purification from total RNA preps)	Invitrogen	Cat# 61006
EnzChek™ Phosphate Assay Kit	Thermo Fisher	Cat# E6646
RNA Clean and Concentrator-5	Zymo Research	Cat# R1016
Deposited data		
APEX-seq with stress treatment	This paper	GEO: GSE171792
APEX-seq without stress treatment	This paper	GEO: GSE193783
Raw data	This paper; Mendeley Data	https://dx.doi.org/10.17632/9hs5d4fvgd.1
Experimental models: Cell lines		
Human: HeLa	ATCC	CCL-2, RRID:CVCL_0030
Human: HEK 293T	ATCC	CRL-3216, RRID:CVCL_0063
Mouse: N2a	ATCC	CCL-131, RRID:CVCL_0470
Oligonucleotides		
Primers for all the recombinant DNA	This paper	Table S3
Recombinant DNA		
pPB DDX3X	This paper	N/A
pPB DDX3Y	This paper	N/A
pPB DDX3X-IDR1	This paper	N/A
pPB DDX3Y-IDR1	This paper	N/A
pPB DDX3X-Helicase	This paper	N/A
pPB DDX3Y-Helicase	This paper	N/A
pPB DDX3X-IDR2	This paper	N/A
pPB DDX3Y-IDR2	This paper	N/A
pPB DDX3X-ΔIDR1	This paper	N/A
pPB DDX3Y-ΔIDR1	This paper	N/A
pPB DDX3X-ΔIDR2	This paper	N/A
pPB DDX3Y-ΔIDR2	This paper	N/A
pPB DDX3X-ΔHelicase	This paper	N/A
pPB DDX3Y-ΔHelicase	This paper	N/A
pPB DDX3X^{IDR1}-DDX3Y^{Helicase}-DDX3Y^{IDR2}	This paper	N/A
pPB DDX3Y^{IDR1}-DDX3X^{Helicase}-DDX3X^{IDR2}	This paper	N/A
pPB DDX3X^{IDR1}-DDX3X^{helicase}-DDX3Y^{IDR2}	This paper	N/A
pPB DDX3Y^{IDR1}-DDX3Y^{helicase}-DDX3X^{IDR2}	This paper	N/A
pPB DDX3X^{IDR1}-DDX3Y^{helicase}-DDX3X^{IDR2}	This paper	N/A
pPB DDX3Y^{IDR1}-DDX3X^{helicase}-DDX3Y^{IDR2}	This paper	N/A
pcDNA3 mito-APEX2	This paper	N/A

(*Continued on next page*)

Please cite this article in press as: Shen et al., Sexually dimorphic RNA helicases DDX3X and DDX3Y differentially regulate RNA metabolism through phase separation, Molecular Cell (2022), https://doi.org/10.1016/j.molcel.2022.04.022

Continued

REAGENT or RESOURCE	SOURCE	IDENTIFIER
pPB DDX3X-EGFP	This paper	N/A
pPB DDX3Y-EGFP	This paper	N/A
pcDNA3 FLAG-DDX3X	This paper	N/A
pcDNA3 FLAG-DDX3Y	This paper	N/A
pcDNA3 HA-DDX3X	This paper	N/A
pcDNA3 HA-DDX3Y	This paper	N/A
pET-MCN_His-TEV_V5-DDX3X-mCherry	(Hondele et al., 2019)	N/A
pET-MCN_His-TEV_V5-DDX3Y-mCherry	This paper	N/A
pET-MCN_His-TEV_V5-DDX3X^{IDR1}-DDX3Y^{Helicase}-DDX3Y^{IDR2}-mCherry	This paper	N/A
pET-MCN_His-TEV_V5-DDX3Y^{IDR1}-DDX3X^{Helicase}-DDX3X^{IDR2}-mCherry	This paper	N/A
pET-MCN_His-TEV_V5-DDX3X^{IDR1}-DDX3X^{helicase}-DDX3Y^{IDR2}-mCherry	This paper	N/A
pET-MCN_His-TEV_V5-DDX3Y^{IDR1}-DDX3Y^{helicase}-DDX3X^{IDR2}-mCherry	This paper	N/A
pET-MCN_His-TEV_V5-DDX3X^{IDR1}-DDX3Y^{helicase}-DDX3X^{IDR2}-mCherry	This paper	N/A
pET-MCN_His-TEV_V5-DDX3Y^{IDR1}-DDX3X^{helicase}-DDX3Y^{IDR2}-mCherry	This paper	N/A
pMAL-c2X	(Walker et al., 2010)	Addgene Plasmid #75286, RRID:Addgene_75286
pMAL-c2X-DDX3X	This paper	N/A
pMAL-c2X-DDX3Y	This paper	N/A
pcDNA5/FRT/TO APEX2-GFP	(Padrón et al., 2019)	Addgene Plasmid #129640, RRID:Addgene_129640
pJ4M/TDP-43	(Hallegger et al., 2021)	Addgene plasmid # 104480, RRID:Addgene_104480
pPB APEX2-DDX3X	This paper	N/A
pPB APEX2-DDX3Y	This paper	N/A
pPB APEX2-EGFP	This paper	N/A
Software and algorithms		
HISAT2	(Kim et al., 2015)	https://daehwankimlab.github.io/hisat2/, RRID:SCR_015530
DESeq2	(Love et al., 2014)	https://bioconductor.org/packages/release/bioc/html/DESeq2.html, RRID:SCR_015687
featureCounts	(Liao et al., 2014)	http://subread.sourceforge.net/, RRID:SCR_012919
trimmomatic	(Bolger et al., 2014)	http://www.usadellab.org/cms/index.php?page=trimmomatic, RRID:SCR_011848
R	https://www.r-project.org	https://www.r-project.org, RRID:SCR_000036
Fiji	(Schindelin et al., 2012)	https://imagej.net/Fiji, RRID:SCR_002285
GraphPad Prism	GraphPad Software	https://graphpad.com, RRID:SCR_002798
Other		
384-well microscopy plates	Brooks Life Sciences	Cat#4ti-0203
Amicon ultra-15	EMD Millipore	Cat# UFC901024

Please cite this article in press as: Shen et al., Sexually dimorphic RNA helicases DDX3X and DDX3Y differentially regulate RNA metabolism through phase separation, Molecular Cell (2022), https://doi.org/10.1016/j.molcel.2022.04.022

RESOURCE AVAILABILITY

Lead contact

Further information and requests for resources and reagents should be directed to and will be fulfilled by the lead contact, Kathy Fange Liu (liufg@pennmedicine.upenn.edu).

Materials availability

All materials generated in this study are available on request to lead contact.

Data and code availability

- RNA-seq data have been deposited at GEO and are publicly available as of the date of publication. Accession numbers are listed in the key resources table. Original western blot images have been deposited at Mendeley and are publicly available as of the date of publication. The DOI is listed in the key resources table. Microscopy data reposted in this paper will be shared by the lead contact upon request.
- This paper does not report original code.
- Any additional information required to reanalyze the data reported in this paper is available from the lead contact upon request.

EXPERIMENTAL MODEL AND SUBJECT DETAILS

Cell culture, transfection, and *Escherichia coli* strains

HeLa, HEK293T, and N2a cells were cultured in DMEM + GlutaMAX (GIBCO) with 10% FBS (GIBCO) and 1% Pen/Strep (Corning) in a humidified incubator with 5% CO_2 at 37°C.

For bacterial cell culture, TOP10 and BL21(DE3)-RIL chemically competent bacterial strains grew in lysogeny broth containing the corresponding antibiotics at 200 rpm, 37°C.

The negative control siRNA from Ambion (AM4611) was used as a control siRNA in the knockdown experiments. DDX3X siRNA was purchased from Ambion (Assay ID 145803). Lipofectamine 2000 (Invitrogen) and Lipofectamine RNAiMax (Invitrogen) from Invitrogen were used for plasmids and siRNA transfection, respectively. It took 48 hrs for siRNA knockdown and 24 hrs for plasmid expression.

METHOD DETAILS

Constructs

For recombinant MBP-DDX3X and MBP-DDX3Y protein expression: DNA fragments encoding human DDX3X were PCR-amplified from the HeLa cDNA library, and the human DDX3Y coding sequence was PCR-amplified from pCMV6-DDX3Y (Origene RC226072). These DNA fragments were then inserted into the pMAL-c2x vector (Walker et al., 2010) (Addgene Plasmid #75286) using restriction enzymes BamHI and SalI. A TEV enzyme digestion sequence (protein sequence ENLYFQG; DNA sequence GAAAACCTG TACTTCCAGGGA) was added to the forward primers, and a His-tag sequence (protein sequence HHHHHH; DNA sequence CATCATCACCATCACCAC) was added to the reverse primers. For *in vitro* LLPS experiments, the pETMCN_His-TEV_V5-DDX3Y-mCherry construct was made by swapping the DDX3Y with the DDX3X in the pETMCN_His-TEV_V5-DDX3X-mCherry (Hondele et al., 2019) using NdeI and BamHI restriction enzymes. For expression of DDX3X and DDX3Y in mammalian cells, DNA fragments encoding the full-length DDX3X and full-length DDX3Y were inserted into the pPB vector with FLAG (DYKDDDDK) and HA (YPYDVPDYA) tags before the N-terminus of the proteins using MfeI and SalI (XhoI was used for digesting the pPB vector) restriction enzymes. The plasmids expressing FLAG or HA single-tagged DDX3X and DDX3Y were made by inserting the DNA fragments encoding full-length DDX3X or full-length DDX3Y into the modified pcDNA3 vector with FLAG or HA tag in frame at the N-terminus.

For the truncation variants of DDX3X and DDX3Y, the following truncations were put into the pPB vector (domain prediction based on PONDR; Xue et al., 2010): IDR1 of DDX3X (amino acids 1 - 168); IDR1 of DDX3Y (amino acids 1 - 164); IDR2 of DDX3X (amino acids 580 - 662); IDR2 of DDX3Y (amino acids 579 - 660); helicase domain of DDX3X (amino acids 169 - 579); helicase domain of DDX3Y (amino acids 165 - 578); ΔIDR1 truncation variant of DDX3X (amino acid 169 - 662); ΔIDR1 truncation variant of DDX3Y (amino acids 165 - 660); ΔIDR2 truncation variant of DDX3X (amino acids 1 - 579); ΔIDR2 truncation variant of DDX3Y (amino acids 1 - 578); ΔHelicase truncation variant of DDX3X (amino acids Δ169 - 579); ΔHelicase truncation variant of DDX3Y (amino acids Δ165 - 578). For domain-swap variants of DDX3X and DDX3Y, the following constructs were inserted into the pPB vector: $DDX3X^{IDR1}$-$DDX3Y^{Helicase}$-$DDX3Y^{IDR2}$; $DDX3Y^{IDR1}$-$DDX3X^{Helicase}$-$DDX3X^{IDR2}$; $DDX3X^{IDR1}$-$DDX3X^{helicase}$-$DDX3Y^{IDR2}$; $DDX3Y^{IDR1}$-$DDX3Y^{helicase}$-$DDX3X^{IDR2}$; $DDX3X^{IDR1}$-$DDX3Y^{helicase}$-$DDX3X^{IDR2}$; $DDX3Y^{IDR1}$-$DDX3X^{helicase}$-$DDX3Y^{IDR2}$. DDX3X-EGFP, DDX3X-mCherry, DDX3Y-EGFP, and DDX3Y-mCherry with a linker sequence (amino acids GlyGlySerGly) inserted between DDX3X/DDX3Y and EGFP/mCherry were inserted into the pPB vector using MfeI and SalI restriction enzymes. Those domain-swap variants were cloned into the pETMCN_His-TEV_V5-mCherry vector to express mCherry-tagged proteins in *E.coli* as well.

For APEX2-seq experiments, the DNA fragment encoding APEX2 was PCR amplified from pcDNA5/FRT/TO APEX2-GFP (Addgene, 129640) and fused to DDX3X and DDX3Y using fusion PCR. APEX2-DDX3X and APEX2-DDX3Y were inserted into the pPB

Please cite this article in press as: Shen et al., Sexually dimorphic RNA helicases DDX3X and DDX3Y differentially regulate RNA metabolism through phase separation, Molecular Cell (2022), https://doi.org/10.1016/j.molcel.2022.04.022

vector using MfeI and Sal I restriction enzymes, and APEX2-EGFP was inserted into the pPB vector using MfeI and XhoI restriction enzymes. To validate the biotin labeling efficiency of APEX2, the plasmid pPB mito-APEX2 was constructed. The DNA fragment encoding a mitochondria matrix localization sequence (amino acids MLATRVFSLVGKRAISTSVCVRAH) derived from *COX4* was added to the APEX2 forward primer for the PCR reaction. The PCR product was subsequently inserted into the pcDNA3 vector by using BamHI and XhoI restriction enzymes.

All the sequences of the primers used for these clones are summarized in Table S3, and each plasmid was validated by Sanger sequencing.

Protein purification

The pMAL-c2X-DDX3X, pMAL-c2X-DDX3Y plasmids were transformed into *Escherichia coli* strain BL21-RIL to express the MBP-tagged recombinant proteins. The pETMCN_His-TEV_V5-DDX3X-mCherry (Hondele et al., 2019), pETMCN_His-TEV_V5-DDX3Y-mCherry and other domain-swap variants in the pETMCN_His-TEV_V5-mCherry vectors were transformed into *E. coli* strain BL21-RIL to express the mCherry-tagged recombinant proteins. The bacteria were cultured in lysogeny broth at 37°C till $OD_{600\ nm}$ = 0.8 before administration of 1 mM IPTG at 16°C for 16 hrs. The pellets from 2 L bacterial culture were resuspended with 80 mL binding buffer (25 mM Tris-HCl, pH 7.5, 500 mM NaCl) and sonicated. After centrifuging at 12,000 rpm for 30 min to remove the cell debris, the supernatant was loaded to a Ni-NTA column. Next, 10 column volumes of the binding buffer supplemented with 50 mM imidazole was used as buffer A to wash away the non-specific binding proteins. Another 10 column volumes of a high salt buffer (25 mM Tris-HCl, pH 7.5, and 2 M NaCl) was used to decrease the amount of bound RNAs from DDX3X or DDX3Y. Finally, four column volumes of the binding buffer supplemented with 500 mM imidazole was used to elute the bound proteins. The DDX3X-mCherry and DDX3Y-mCherry recombinant proteins were dialyzed into the storage buffer (25 mM Tris-HCl, pH 7.5, 500 mM NaCl, 10% glycerol, and 2 mM DTT) and the His-tag was cleaved using TEV enzyme simultaneously with the dialysis. Then, the proteins were concentrated using Amicon Ultra-15 (Millipore) tubes before loading to a Superdex 200 column, with buffer (25 mM Tris-HCl, pH 7.5, and 500 mM NaCl) for mCherry tagged proteins and buffer (25 mM Tris-HCl, pH 7.5, 200 mM NaCl) for MBP tagged proteins. MBP-tagged proteins were purified at 4°C, while mCherry-tagged proteins were purified at room temperature. The purity of the proteins was analyzed by SDS-PAGE. Purified proteins were aliquoted, snap-frozen in liquid nitrogen and stored at -80°C. Once thawed, aliquots were never refrozen.

GST-TEV-FUS^{WT} was purified as described (Sun et al., 2011). Briefly, *E. coli* cells were lysed by sonication on ice in PBS with protease inhibitors (cOmplete, EDTA-free, Roche Applied Science). The protein was purified over Glutathione Sepharose 4 Fast Flow (GE Healthcare) and eluted from the beads using 50 mM Tris-HCl pH 8, 20 mM trehalose, and 20 mM glutathione. Purified protein was snap-frozen in liquid nitrogen and stored at -80°C.

pJ4M/TDP-43 was a gift from Nicolas Fawzi (Addgene plasmid # 104480). TDP-43 was purified as previously described (Hallegger et al., 2021). Briefly, the plasmid was transformed into BL21(DE3) RIL *E. coli*. Cells were harvested by centrifugation and lysed by lysozyme (1 mg/mL) and sonication in wash buffer (20 mM Tris-HCl pH 8.0, 1 M NaCl, 10 mM imidazole, 10% glycerol, 1 mM DTT, 5 μM Pepstatin A, 100 μM PMSF, and cOmplete, EDTA-free, Roche Applied Science protease inhibitors). The protein was purified over Ni-NTA agarose beads (QIAGEN) and eluted from the beads using elution buffer (wash buffer except with 300 mM imidazole rather than 10 mM imidazole). The protein was further purified over amylose resin (NEB) and eluted with 20 mM Tris-HCl pH 8.0, 1 M NaCl, 10 mM imidazole, 10% glycerol, 1 mM DTT, 5 μM Pepstatin A, 100 μM PMSF, and 10 mM maltose. The protein was concentrated, snap-frozen in liquid nitrogen, and stored at -80°C.

Differential scanning fluorimetry assay

Purified MBP-DDX3X and MBP-DDX3Y proteins were diluted to 0.25 mg/mL. 19 μL of each protein was transferred to a well of a 384-well plate, and 1 μL of 5-fold SYPRO Orange (Thermo Fisher) was added to each well. The plate was sealed and spun at 3,600 *g* for 2 min. The fluorescent signal at 570 nm was collected using a qRT-PCR machine with the temperature ramping from 20 to 95°C. The data were analyzed using DSF World (Wu et al., 2020).

In vitro LLPS assay

The *in vitro* LLPS was set up at room temperature with total volume of 20 μL in PCR tube. Proteins were diluted to 100 μM (DDX3X-mCherry and DDX3Y-mCherry) or 75 μM (DDX3X-mCherry, DDX3Y-mCherry and all the domain-swap mutants) using the storage buffer. 10 μL buffer (25 mM Tris-HCl, pH 7.5, 500 mM NaCl) and 2 μL diluted protein were transferred to the PCR tube. Then, 8 μL water was added to the tube to observe the LLPS of protein alone; 2 μL polyU-RNA (2 mg/mL, dissolved in water) and 6 μL water were added to the tube to observe the LLPS of protein with RNA; 2 μL polyU-RNA (2 mg/mL, dissolved in water), 2 μL ATP buffer (40 mM ATP and 50 mM $MgCl_2$) or UTP buffer (40 mM UTP and 50 mM $MgCl_2$) and 4 μL water were added to the tube to observe the LLPS of protein with RNA and ATP or UTP. To observe the LLPS of different combinations of DDX3X-mCherry and DDX3Y-mCherry, the proteins were diluted to the proper concentrations. Then 10 μL buffer, 2 μL diluted protein and 8 μL water were transferred to a PCR tube. The mixtures were mixed by pipetting and transferred to 384-well glass-bottomed plate. After incubating at room temperature for 1 hr, the plate was spun at 100 *g* for 1 min. Then the images were taken using a Zeiss LSM 880 confocal microscope under a 63 × oil lens.

Immunofluorescence cell staining

Cells were passaged to a 6-well plate with a coverslip in each well and cultured overnight. The cells were washed once in PBS and then fixed using 4% paraformaldehyde in PBST (PBS with 0.05% Tween-20) at room temperature for 15 min. Then, the cells were washed twice by PBST and permeabilized by 0.5% Triton at room temperature for 20 min. After being washed once by PBST, the cells were blocked with 1% BSA in PBST at room temperature for 30 min. Then, the blocking solution was replaced with 1 mL blocking solution supplemented with desired primary antibodies (at 1:1000 dilution) and incubated at room temperature for 1 hr or 4 °C overnight. After 4 washes with PBST, the corresponding Alexa Fluor-conjugated secondary antibodies were applied (1:1,000 diluted in the blocking solution) and incubated at room temperature for 1 hr. After being washed three times by PBST, the cells were incubated with 0.5 μg/mL DAPI for 1 min. After 4 times PBST washes, an antifade reagent (Invitrogen) was used to mount the slides. The images were taken using a Leica TCS SP8 confocal microscope. The "analyze particles tool" in Fiji (Schindelin et al., 2012) was utilized to quantify the sizes of the SGs in mammalian cells in about 50 different cells per condition. The sizes of the SG in cells were analyzed by two researchers independently.

Fluorescence recovery after photobleaching

The FRAP assays were conducted using the bleaching module of the Zeiss LSM 880 confocal microscope for DDX3X and DDX3Y droplets individually. The 488 nm laser was used to bleach the EGFP signal, and the 561 nm laser was used to bleach the mCherry signal. Bleaching was focused on a circular region of interest (ROI) using 100% laser power, and time-lapse images were collected afterward. A same-sized circular area away from the bleaching point was selected as an unbleached control. The fluorescence intensity was directly measured in the Zen software. The values were reported as relative to pre-bleaching time points. GraphPad Prism was used to plot the data. The halftime for each replicate was calculated using the following formula: $y=a\cdot(1-\exp(-b\cdot x))+c$, in which a is the slow recovery fraction, c is the rapid diffusion fraction, and b is the recovery rate. The halftime is $\ln 2 / b$, and a mobile fraction is $a + c$. The two-tail t-test was used to calculate the p-values. For FRAP of the live cells, cells expressing DDX3X-EGFP or DDX3Y-EGFP were cultured in 35 mm poly-D-lysine coated glass-bottomed dishes (Mattek). Before taking the images, cells were treated with 500 μM sodium arsenite for 1 hr in the FluoroBrite DMEM medium with 10% FBS. A 20 × lens was used at zoom scale 6. For FRAP of *in vitro* LLPS, a 63 × oil lens was used.

Formation of stress granules in cells

Cells were seeded in a 6-well plate and cultured overnight. The following stressors: 500 μM sodium arsenite (1 hr), 1 M sorbitol (1 hr), 50 μM thapsigargin (1 hr), 40 μg/mL puromycin (3 hrs), and 10 μM MG132 (3 hrs) were added to the cell culture media (DMEM + 10% FBS) each in a separate well. For the stress condition of 60 μM CCCP, CCCP was added to glucose-free DMEM with 10% FBS. After the treatment, cells were fixed and subjected to the immunofluorescence imaging procedure detailed above.

Sequence alignment

The amino acid sequences of DDX3X and DDX3Y were downloaded from CCDS Database and aligned using Clustal Omega. The alignment results were redrawn using ESPript 3.0 (Robert and Gouet, 2014). The sequences were used to predict the natural disordered regions by PONDR (Xue et al., 2010), prion-like amino acid regions by PLAAC (Lancaster et al., 2014) and LLPS propensity by catGRANULE (Mitchell et al., 2013).

Turbidity assay

DDX3X-mCherry and DDX3Y-mCherry proteins were diluted to 10, 20, 30, 50, 75, 100, 125 and 150 μM using the storage buffer. 15 μL buffer (25 mM Tris-HCl, pH 7.5, 200 mM NaCl), 3 μL diluted protein were transferred to the PCR tube, 3 μL polyU-RNA (2 mg/mL, dissolved in water), and 9 μL water were mixed in a PCR tube. After incubating for 20 min at room temperature, the mixtures were transferred to a 384-well black plate with a clear flat bottom. The turbidity was measured by using a Tecan plate reader at $OD_{600\ nm}$. Then, the solution was transferred to a clean Eppendorf tube, and spun at 16,000 *g* for 2 min. The supernatant was used to measure protein concentration using Bradford method.

Construction of DOX-inducible cell lines

5 μg of the lentiviral vectors expressing mClover3-FUS, 2.5 μg VSVG plasmid, and 3.75 μg pPAX2 plasmid were co-transfected to 100% confluent HEK 293T cells in 6-well plate with 40 μL polyethylenimine. The medium was changed after 6 to 8 hrs. 500 μL medium containing the virus was collected twice a day and 500 μL fresh medium was replenished at each time. The virus was collected in a total three-day period, and then spun down at 3000 rpm for 5 min at room temperature. The HeLa cells were infected with lentivirus with 8 μg/mL polybrene. After induction with 100 ng/mL of doxycycline (DOX) for two days, the cells were subjected to cell sorting. Western blots were performed to validate the expression of mClover3-FUS by using anti-GFP antibody.

Colocalization of DDX3X/Y with FUS in cells

The DOX-inducible HeLa cells expressing mClover3-FUS were seeded in a 6-well plate with 100 ng/mL of DOX and a coverslip in the well. 1 μg of empty vector, DDX3X-pPB, or DDX3Y-pPB were transfected to those cells respectively using lipofectamine 2000. 24 hrs

Please cite this article in press as: Shen et al., Sexually dimorphic RNA helicases DDX3X and DDX3Y differentially regulate RNA metabolism through phase separation, Molecular Cell (2022), https://doi.org/10.1016/j.molcel.2022.04.022

later, sodium arsenite was used to each well at a final concentration of 500 μM for 1 hr. The cells were then subjected to the immunofluorescence cell stain protocol as discussed above.

Cycloheximide chase assay

The cycloheximide (CHX) chase assay was performed to explore the half-life of DDX3X and DDX3Y proteins in cells. HeLa cells were seeded in 6-well plate and transfected with 1 μg of DDX3X-pPB and DDX3Y-pPB respectively. 24 hrs later, CHX was added to the cells at a final concentration of 100 μg/mL and incubated for different time intervals. Then, the cells were collected and lysed with RIPA buffer (25 mM Tris-HCl, pH 7.4, 150 mM NaCl, 2 mM EDTA, and 1% NP-40). The protein concentrations were measured using a Bradford assay and the same amount of cell lysate was used in Western blot analyses. The intensity for each band was quantified using Fiji. The intensity for each DDX3X and DDX3Y band was normalized to the corresponding GAPDH intensity firstly, and then for each replicate at different time points were normalized to time 0 hr. The data were plotted in Prism and an exponential decay formula was used to determine the half-life of DDX3X and DDX3Y. The degradation rate K_{decay} was estimated by $\ln(A_t/A_0) = -K_{\mathrm{decay}}\,t$ where A_t and A_0 stand for the quantity at time t and time 0. Thus, the half-life ($t_{1/2}$), when 50% of the protein is decayed is described by $t_{1/2} = \ln 2 / K_{\mathrm{decay}}$.

Puromycin incorporation assay

HeLa cells were seeded in a 6-well plate with a coverslip in it, and then transfected with 1 μg of pPB-DDX3X and pPB-DDX3Y respectively. After 24 hrs, a final concentration of 500 μM sodium arsenite was added to the DMEM and incubated for 5 min to trigger stress granule formation. Then, the medium was replaced by fresh DMEM medium with puromycin (1 μg/mL). After incubating for 30 min in a humidified incubator with 5% CO_2 at 37°C, the cells were then washed with 1 × PBS and subjected to the immunofluorescence cell staining protocol as described above using anti-puromycin and anti-FLAG antibodies.

Malachite green ATPase assay

ATPase measurements were taken using the Malachite Green Phosphate Assay Kit according to the manufacturer's instructions. Briefly, 1.0 μM MPB-DDX3X or MBP-DDX3Y was incubated with 100 ng/μL total RNA extracted from HeLa cells for 15 min in the reaction buffer (25 mM Tris-HCl, pH 8, 200 mM NaCl, 1 mM DTT, and 2 mM MgCl2) before the addition of 2 mM ATP. The reaction was incubated at room temperature for 30 min. Then the reaction was quenched by the addition of malachite green mixture and left for an additional 30 min to develop the color. The samples were then loaded into a clear-bottom 384-well plate and absorbance at $OD_{600\ \mathrm{nm}}$ was measured. Values were converted from absorbance units to μM free phosphate using a standard curve generated with the kit's phosphate standard. Background values (free phosphates detected from reactions lacking RNA) were subtracted from the value from reactions with RNA. Data were plotted in Prism. Significance was calculated using Student's two-tailed t test.

Continuous ATPase assay

ATPase measurements were taken using the EnzChek Phosphate Assay Kit (ThermoFisher) as previously described (Song and Ji, 2019). Briefly, MBP-DDX3X or MBP-DDX3Y was titrated at the indicated concentrations into 500 μL reactions containing 40 mM Tris-HCl pH 7.5, 50 mM NaCl, 0.5 mM $MgCl_2$, 2 mM DTT, 0.5 units Super RNaseIN, 0.01% NP-40 substitute and 100 nM annealed duplex RNA (sequence in Table S3). After 10 min of incubation at room temperature, the reaction was started by adding 2 mM magnesium ATP. The reaction progress was monitored over five min at 30 sec intervals as absorbance at 360 nm. Absorbance values were the converted to μM/min using a standard curve and initial rates were plotted and fit to Hill kinetics using Prism.

smFRET

PEG-passivated slides were prepared according to previously published protocols with minor modifications (Jamiolkowski et al., 2017). Briefly, glass coverslips and slides were sonicated at 40°C twice with acetone for 15 min followed by sonication with methanol (25 min), 1 M KOH (40 min), and ethanol (15 min). Plasma cleaning was then used to remove any remaining contaminants from the surfaces. Plasma cleaned slides and coverslips were then incubated in a solution composed of 1.4 mL of 3-aminopropyltriethoxysilane (APTES), 2.3 mL of glacial acetic acid, and 46 mL of methanol overnight at room temperature. Silicated slides and coverslips were then incubated with polyethylene glycol (PEG, Laysan Bio, Inc., containing 20% (w/w) mPEG succinimidyl valerate, MW 2000 and 1% biotin-PEG-SC, MW 2000) in 0.1 M sodium bicarbonate (pH 8.3) for four hrs followed by an additional incubation overnight in a humidifying chamber. Slides and coverslips were then washed with MilliQ water and used to construct flow chambers for single molecule experiments with double-sided sticky tape. Double stranded RNA with a 5' overhang was obtained as follows: 5'-biotin/ACCGCUGCCGUCGCUCCG/AlexF647N/-3'; and 5'-/Cy3/UUUUUUUUUUUUUUUUUUUUUUUUUUUUUUUUUUUUUUUUUUUUUUUUUUUUUUUUCGGAGCGACGGCAGCGGU-3' were ordered from IDT; the two strands were annealed by heating the sample at 65°C for 5 min, then slowly cooling the sample to room temperature over 3 hrs. 2 mM protocatechuic acid (PCA), 0.05 μM protocatechuate-3,4,dioxygenase, 2.45 mM 6-hydroxy-2,5,7,8- tetramethylchromane-2-carboxylic (Trolox), 1 mM cyclooctatetraene (COT), and 1 mM 4-nitrobenzyl alcohol (NBA) were added to the imaging buffer (125 mM NaCl and 50 mM Tris-HCl pH 7.5). 70 pM biotinylated, fluorescent dsRNA was added to the flow cell and incubated for 6 min. Unbound RNA was washed out and recording either commenced or DDX3X or DDX3Y were first added as indicated in the text. The TIRF microscope, optics and camera were used to record smFRET as in previous report (Jamiolkowski et al., 2017). All FRET measurements were carried out at room

temperature (~23°C) using a frame interval of 100 ms with alternating 532 nm/640 nm laser excitation (ALEX; effective frame interval 200 ms). Data analyses were carried out using custom scripts written in either Python or Java. Background-corrected fluorescence intensities and FRET distributions were corrected for differential quantum yield, differential detector sensitivity, direct excitation of the A647 by the 532 nm laser and leakage of Cy3 fluorescence into the acceptor detector channel as in previous report (Hellenkamp et al., 2018; Jamiolkowski et al., 2017). Only recordings exhibiting a single step photobleaching event in the direct acceptor excitation (ALEX) channel were further analyzed and included in FRET distributions.

RNA isolation

A Direct-zol RNA MicroPrep kit (Zymo Research) was used to isolate total RNA following the manufacturer's instructions. DNA digestion was performed on the column at room temperature for 15 min to remove the DNA contamination of the extracted RNA. For a larger scale of RNA purification, total RNA was purified by TRIzol reagent (Invitrogen), following the manufacturer's instruction.

qRT-PCR

qRT-PCR was performed using a Luna Universal One-Step RT-qPCR kit (NEB) to assess the relative abundance of RNA in each sample. All samples used for qRT-PCR were treated with DNase I to remove possible DNA contamination. The primers used for qRT-PCR are listed in Table S3.

Cellular APEX labeling

To enable APEX labeling in mammalian cells, we followed a previously established protocol (Fazal et al., 2019). Briefly, the cells were treated with or without 500 μM sodium arsenite in DMEM media for 30 min. Then, the DMEM media with 500 μM sodium arsenite was replaced with DMEM media supplemented with 500 μM sodium arsenite and 500 mM biotin-phenol for another 30 min. Next, H_2O_2 (Sigma-Aldrich) was added to each cell culture dish at 1 mM final concentration for exactly 1 min with gentle agitation. To stop the labeling, the culture media was removed, and the quenching solution (10 mM sodium ascorbate, 10 mM sodium azide, and 5 mM Trolox in PBS) was immediately used to wash the cells three times. Finally, 1 mL quenching solution was applied to cover the cells. Cells were then collected with a cell scraper. The unlabeled control samples were prepared in parallel under the same procedure as aforementioned, without the addition of the H_2O_2.

Validation of APEX labeling

To validate APEX labeling in cells, after the cellular labeling reaction, the cells were lysed using RIPA buffer (25 mM Tris-HCl, pH 7.4, 150 mM NaCl, 2 mM EDTA, and 1% NP-40) supplemented with 10 mM sodium ascorbate, 10 mM sodium azide, 5 mM Trolox, and proteinase inhibitor on ice for 15 min. After centrifugation, the supernatant of the cell lysate was loaded on an SDS-PAGE gel and transferred to a PVDF membrane (Millipore) by a semi-dry transfer instrument. The membrane was blocked with 5% BSA in PBST at 4 °C overnight. 1:20,000 diluted streptavidin-HRP antibody (cell signaling) in 5% BSA was used at room temperature for 1 hr to detect the biotinylated proteins. After washing three times with PBST, the membrane was visualized by ECL Western Blotting Detection Kit (Thermo Fisher). The endogenous biotinylated proteins were also visible at 130, 75, and 72 kDa in both the labeled and unlabeled cells (as expected).

Purification and sequencing biotinylated RNA

After the cellular APEX-labeling, total RNA was extracted using TRIzol following the manufacturer's instruction. To enrich biotinylated RNAs, Pierce streptavidin magnetic beads (Thermo Fisher) were used (20 μL beads per 50 μg RNA). The beads were washed 3 times with 500 μL B&W buffer (5 mM Tris-HCl, pH 7.5, 0.5 mM EDTA, 1 M NaCl, and 0.1% TWEEN 20), followed by 2 times with 500 μL solution A (0.1 M NaOH and 50 mM NaCl), and once with 500 μL solution B (100 mM NaCl). The beads were then suspended in 125 μL solution B. 50 μg RNA diluted in 125 μL water was mixed with the beads and incubated at 4 °C for 2 hrs with rotation. Then, the beads were placed on a magnetic stand to remove the solution and washed 3 times with 500 μL B&W buffer. Finally, the beads were resuspended in 54 μL water. To release the biotinylated RNA, 33 μL proteinase buffer (3 × PBS, 6% N-Lauryl sarcosine sodium solution (Sigma-Aldrich), 30 μM EDTA, and 15 μM DTT) was added to the beads with 10 μL proteinase K (Thermo Fisher) and 5 μL RNase inhibitor. The beads were then incubated at 42 °C for 1 hr and 55°C for 1 hr on a shaker at 600 rpm. The RNA was then purified using a RNA Clean and Concentrator 5 kit (Zymo Research) following the manufacturer's instruction. The resulting RNA was then used for RNA-seq library construction using a TruSeq Stranded mRNA Kit (Illumina). The concentrations for all the libraries were determined by KAPA Library Quantification Kit (KAPA Biosystems) following the manufacturer's protocol and subjected to Next-generation high-throughput sequencing using an Illumina NextSeq 550 with a single-end 75-bp read length.

Validation of the APEX labeling of RNA

To test the specificity of APEX2 labeling, APEX2 was fused with a mitochondrial localization signal (MLATRVFSLVGKRAIS TSVCVRAH, derived from *COX4*) at its N terminus. The localization of the fused protein was validated by immunofluorescence. Total RNA was first extracted from the labeled and unlabeled cells, which was then followed by enrichment of biotinylated RNA using the streptavidin magnetic beads as described above. To test for the RNA enrichment, primers against mitochondria-translated transcripts *ND1* and *ND2*, and cytoplasm translated transcripts *GAPDH* and *TRMT10A* were designed and listed in Table S3. qRT-PCR

Please cite this article in press as: Shen et al., Sexually dimorphic RNA helicases DDX3X and DDX3Y differentially regulate RNA metabolism through phase separation, Molecular Cell (2022), https://doi.org/10.1016/j.molcel.2022.04.022

was performed in the labeled and unlabeled controls. The ratios of RNA recovered in the labeled samples relative to unlabeled controls were calculated.

High throughput data analysis

The high throughput sequencing reads were adaptor and quality trimmed using Trimmomatic (Bolger et al., 2014) with the following command: trimmomatc SE -phred33 ILLUMINACLIP:TruSeq3-SE.fa:2:30:10 LEADING:3 TRAILING:3 SLIDINGWINDOW:4:15 MINLEN:30. Then, the reads were aligned to the GRCh38 human genome reference using HISAT2(Kim et al., 2015). The default parameters were used. Aligned reads were quantified using featureCounts (Liao et al., 2014). Read counts were further analyzed using DESeq2 (Love et al., 2014). Gene ontology (GO) analysis was carried out with the Metascape (Zhou et al., 2019).

In vitro translation

In vitro translation assays were performed using the Flexi Rabbit Reticulocyte Lysate System (Promega). Each reaction (25 μL) contains 10 μL rabbit reticulocyte lysate, 0.25 μL amino acid mixture minus leucine (1 mM), 0.25 μL of amino acid mixture minus methionine (1 mM), 1 μL $Mg(OAc)_2$, 0.25 μL luciferase mRNA (1 mg/mL), 0.5 μL RNase inhibitor, 0.25 μL DTT (1 M), and 12.5 μL of different concentrations of DDX3X-mCherry, DDX3Y-mCherry, or buffer (25 mM HEPES-KOH, pH 7.4, 150 mM KCl, and 2 mM DTT). Assembled reactions were incubated at 30°C for 90 mins. A standard reaction containing 75 μL of the luciferase substrate mixed with 5 μL of the unpurified translation mixture in a white 96-well plate. The luminescence was measured using a luminometer (Promega). To observe any LLPS in the lysate, the lysate from the translation assays was transferred to 384-well glass-bottomed plate. Then, the plate was spun at 100 *g* for 1 min. The images were taken using a Zeiss LSM 880 confocal microscope under a 63 × oil lens.

FUS aggregation assay

First, 0, 0.25, or 0.5 μM MBP-TEV-DDX3X or MBP-TEV-DDX3Y was incubated with 1 μg TEV protease for 30 min at room temperature. Then, 1 μM GST-TEV-FUS^{WT} (or an equal volume of FUS elution buffer [50 mM Tris-HCl pH 8, 20 mM trehalose, 20 mM glutathione]) was added to the reaction and turbidity was used to assess aggregation by measuring absorbance at 395 nm in a Tecan plate reader. Readings from DDX3X or DDX3Y alone were subtracted from the appropriate FUS conditions. Area under the curve was used to compare the extent of aggregation for each condition (GraphPad Prism).

TDP-43 aggregation assay

Firstly, 0, 0.25, or 0.5 μM MBP-TEV-DDX3X or MBP-TEV-DDX3Y in buffer (200 mM NaCl, 25 mM Tris-HCl pH 8.0) was incubated in TDP-43 assay buffer (150 mM NaCl, 20 mM HEPES-NaOH pH 7.0, 1mM DTT) with 0.25 μg TEV protease for 30 minutes at room temperature. Turbidity was assessed by measuring absorbance at 395 nm in a Tecan plate reader. TDP-43 was buffer exchanged into TDP-43 assay buffer (Bio-Rad Micro Bio-Spin Chromatography Columns, following manufacturer's instructions) and concentration was determined via NanoDrop. Turbidity measurements were paused after 30 minutes in order to add 4.0 μM TDP-43 (or an equal volume of TDP-43 assay buffer) to the reaction. Then, turbidity measurements were resumed for an additional 16 hours. The data was standardized by subtracting out the initial reading at t = 1 min. from each respective condition. Values from conditions with DDX3X or DDX3Y alone were then subtracted from the appropriate conditions with TDP-43. Area under the curve analysis was used to compare the extent of aggregation for each condition. The $t_{1/2}$ of aggregation was determined by performing a nonlinear regression (asymmetric sigmoidal) on the data starting after TDP-43 addition (t = 31 min.) (GraphPad Prism).

Protein quantification and western blot

Protein concentrations of the samples were calculated using the Bradford Assay (Bio-Rad). Protein samples were boiled at 95°C in Laemmli sample buffer for 10 min. After brief centrifugation, the samples were loaded onto SDS-PAGE gels. After running at 180 V for 1 hr, the gels were transferred to the PVDF membranes (Millipore) by semi-dry transfer apparatus at 20 V for 50 min. Then, the PVDF membranes were blocked with 5% milk or BSA in 1 × PBST for 30 mins at room temperature or 4°C overnight. The membranes were then incubated in 3% milk or BSA in 1 × PBST containing the corresponding primary antibodies overnight at 4°C. After washing three times with 1 × PBST, the horseradish peroxidase (HRP)-conjugated secondary antibodies (1:20,000) in 1% milk were applied and incubated at room temperature for 1 hr. After washing three times with 1 × PBST, the membranes were visualized using ECL Western Blotting Detection Kit (Thermo Fisher).

QUANTIFICATION AND STATISTICAL ANALYSIS

Images were analyzed using Fiji. All data are presented as the mean ± standard error of mean (s.e.m.) or standard deviation (s.d.) from the independent determinations. The statistical analyses were performed using the GraphPad Prism (GraphPad Software, Inc,; La Jolla, CA, USA). Differences of means were tested for statistical significance with unpaired two-tailed Student's t-test. $^{*}p < 0.05$; $^{**}p < 0.01$; $^{***}p < 0.001$; $^{****}p < 0.0001$; n.s. means $p > 0.05$.

Molecular Cell, Volume *82*

Supplemental information

Sexually dimorphic RNA helicases DDX3X and DDX3Y differentially regulate RNA metabolism through phase separation

Hui Shen, Amber Yanas, Michael C. Owens, Celia Zhang, Clark Fritsch, Charlotte M. Fare, Katie E. Copley, James Shorter, Yale E. Goldman, and Kathy Fange Liu

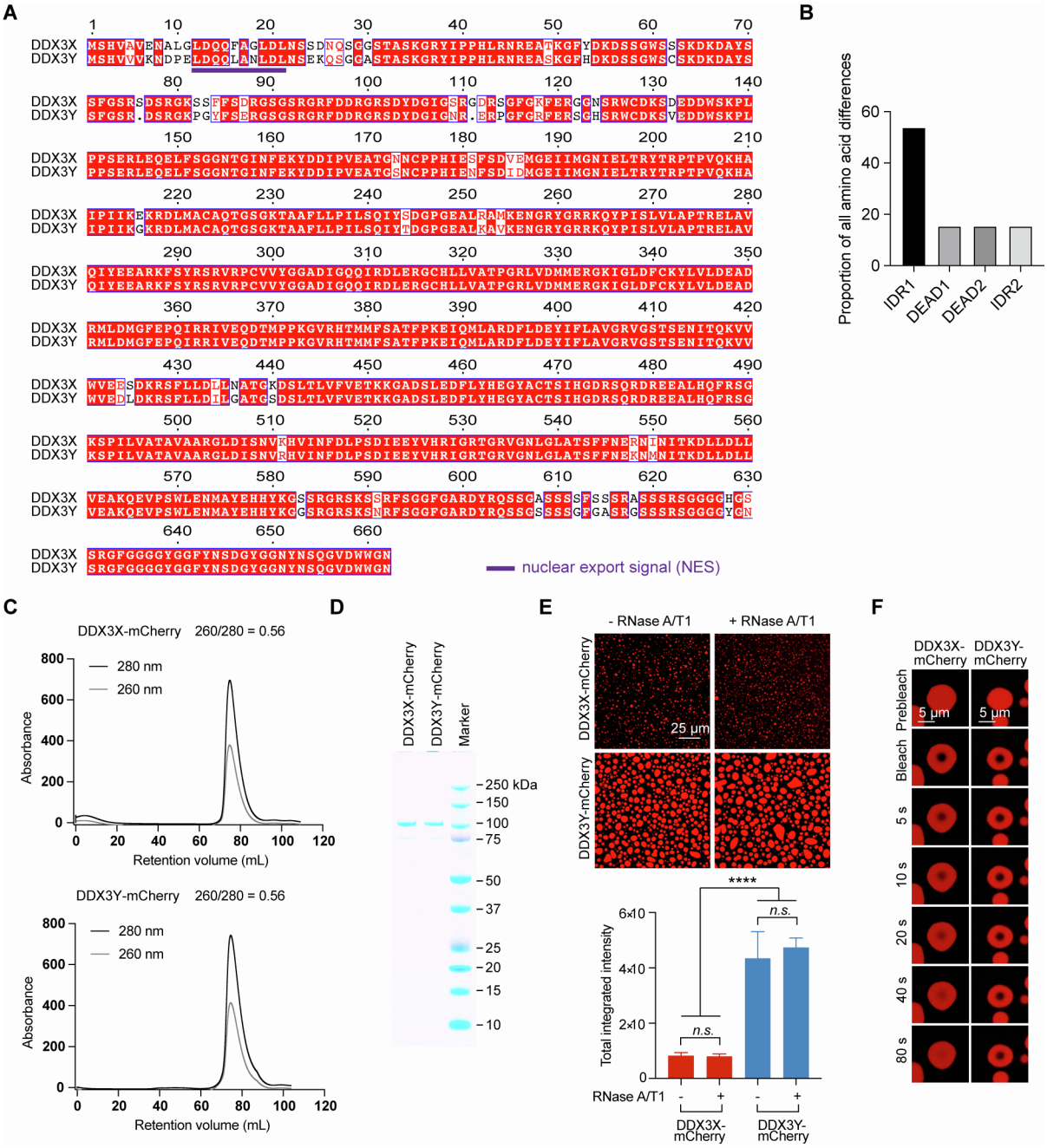
A
DDX3X
DDX3Y
nuclear export signal (NES)
B
Proportion of all amino acid differences
IDR1
DEAD1
DEAD2
IDR2
C
DDX3X-mCherry 260/280 = 0.56
DDX3Y-mCherry 260/280 = 0.56
280 nm
260 nm
Absorbance
Retention volume (mL)
D
DDX3X-mCherry
DDX3Y-mCherry
Marker
250 kDa
150
100
75
50
37
25
20
15
10
E
- RNase A/T1
+ RNase A/T1
25 μm
Total integrated intensity
****
n.s.
RNase A/T1
F
Prebleach
Bleach
5 s
10 s
20 s
40 s
80 s
5 μm

Figure S1 DDX3Y has a stronger LLPS propensity compared to DDX3X *in vitro*. Related to Figure 1. (A) Amino acid sequence alignment of human DDX3X and DDX3Y. The nuclear export signal (NES) is underlined in purple. (B) Percentage of sequence differences attributable to the individual domains (IDR1, DEAD1, DEAD2, and IDR2) between DDX3X and DDX3Y. (C) Chromatographic profiles of the purification of DDX3X-mCherry and DDX3Y-mCherry. The black line refers to A_{280nm}, and the gray line refers to A_{260nm}. The final A_{260nm}/A_{280nm} was determined using a Nanodrop spectrophotometer. The ratios of A_{260nm}/A_{280nm} of DDX3X and DDX3Y indicate that the purified proteins don't contain noticeable RNA carry-over. (D) SDS-PAGE results of purified DDX3X-mCherry and DDX3Y-mCherry proteins. (E) Top: *in vitro* droplet formation of 10 μM recombinant DDX3X-mCherry or DDX3Y-mCherry, with or without RNase treatment, in the presence of 200 ng/μL poly(U)-RNA. Scale bar, 25 μm. Bottom: quantification of the total integrated intensity of DDX3X condensation and DDX3Y condensation from the top panel. A two-tailed t-test was used to calculate the *p*-values between +/- RNase treatment. A nested t-test was used to calculate the *p*-value between DDX3X and DDX3Y groups; *n.s.* $p > 0.05$, ****$p < 0.0001$. (F) One representative biological replicate of Figure 1F. Size-comparable droplets of DDX3X and DDX3Y were chosen. Time-lapse images of the DDX3X-mCherry (10 μM) and DDX3Y-mCherry (10 μM) droplets from *in vitro* FRAP experiments.

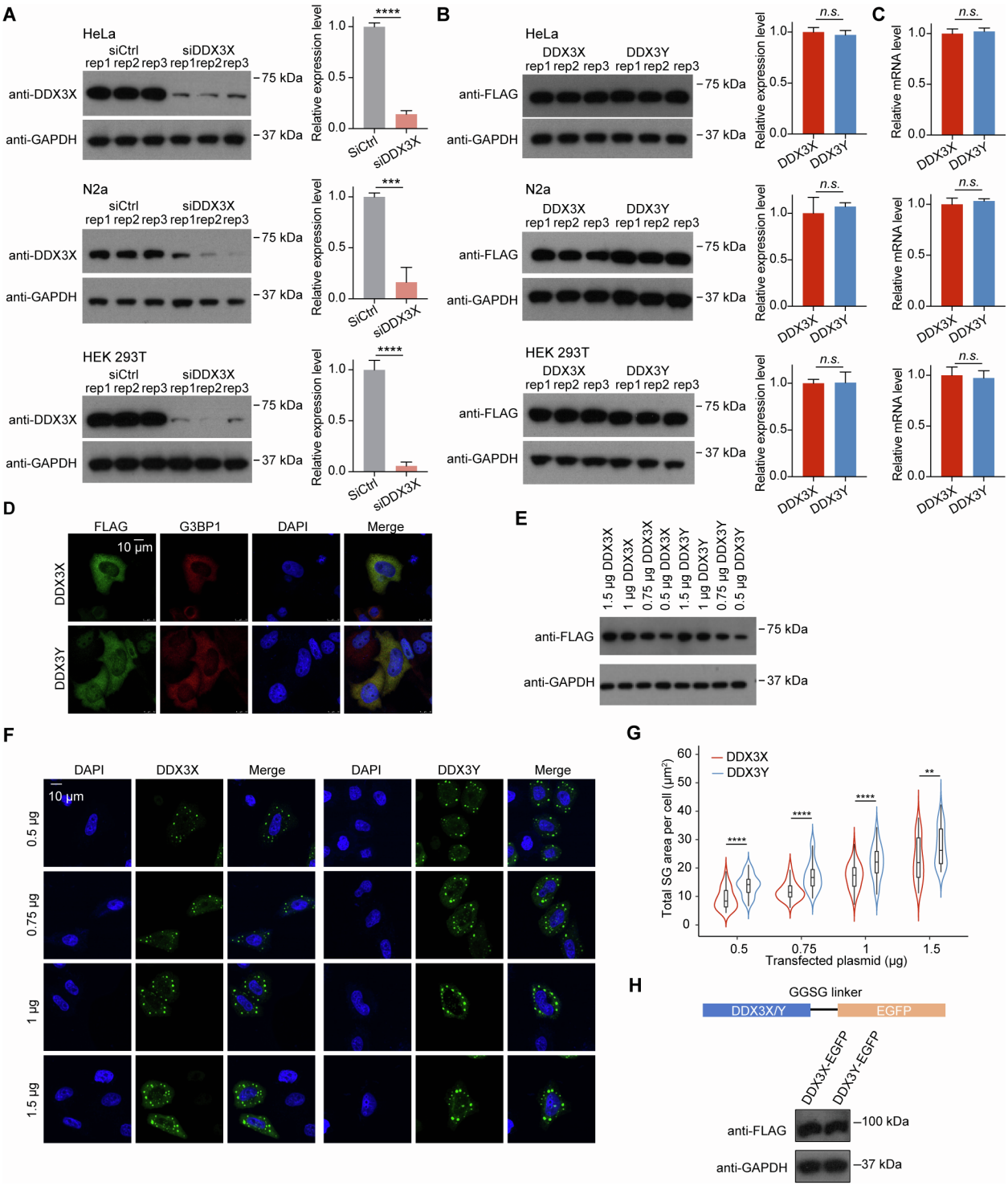
A
HeLa
siCtrl rep1 rep2 rep3
siDDX3X rep1 rep2 rep3
anti-DDX3X
anti-GAPDH
75 kDa
37 kDa
Relative expression level
SiCtrl
siDDX3X
N2a
HEK 293T
B
DDX3X rep1 rep2 rep3
DDX3Y rep1 rep2 rep3
anti-FLAG
n.s.
C
Relative mRNA level
DDX3X
DDX3Y
D
FLAG
G3BP1
DAPI
Merge
10 μm
E
1.5 μg DDX3X
1 μg DDX3X
0.75 μg DDX3X
0.5 μg DDX3X
1.5 μg DDX3Y
1 μg DDX3Y
0.75 μg DDX3Y
0.5 μg DDX3Y
F
0.5 μg
0.75 μg
1 μg
1.5 μg
G
Total SG area per cell (μm²)
Transfected plasmid (μg)
H
GGSG linker
DDX3X/Y
EGFP
DDX3X-EGFP
DDX3Y-EGFP
100 kDa

Figure S2 DDX3Y has a stronger LLPS propensity compared to DDX3X in cells. Related to Figure 2. (A) Western blots showing the expression of DDX3X in DDX3X-knockdown and knockdown control HeLa, N2a, and HEK 293T cells. The intensity of each band was quantified using Fiji. The intensity of each DDX3X band was normalized to the corresponding GAPDH intensity and then normalized to the knockdown control samples. Error bars represent s.d. of three biological replicates. *p* values were determined by a two-tailed t-test; *** $p < 0.001$; **** $p < 0.0001$. (B) Western blot results show that FLAG-DDX3X and FLAG-DDX3Y are expressed at comparable levels in HeLa, N2a, and HEK 293T cells. The intensity of each band was quantified using Fiji. The intensity of each DDX3X or DDX3Y band was normalized to the corresponding GAPDH intensity and then normalized to the DDX3X overexpression samples. Error bars represent s.d. of three biological replicates. *p* values were determined by a two-tailed t-test; *n.s.* $p > 0.05$. (C) RT-qPCR results show that the transcript level of DDX3X and DDX3Y were comparable in HeLa, N2a, and HEK 293T cells. Each sample was normalized to the corresponding loading control GAPDH first and then normalized to DDX3X. *p* values were determined by a two-tailed t-test; *n.s.* $p > 0.05$. (D) Representative images of FLAG-DDX3X or FLAG-DDX3Y localization with G3BP1 in HeLa cells before arsenite treatment. The expression of FLAG-DDX3X and FLAG-DDX3Y did not lead to puncta formation for this condition. Scale bar, 10 μm. (E) Western blot results showing the expression level of DDX3X and DDX3Y in HeLa cells transfected with different amounts of plasmids. (F) Immunofluorescent cell stain of SGs formed by different amounts of DDX3X and DDX3Y. The SGs were triggered by 500 μM sodium arsenite for 1 hr. Scale bar, 10 μm. (G) The total SG area per cell were quantified (n = 50 cells in total, from three biologically independent experiments) and displayed in violin plots. *p* values were determined by a two-tailed t-test; ** $p < 0.01$, **** $p < 0.0001$. (H) Construct and expression of DDX3X-EGFP and DDX3Y-EGFP in HeLa cells. A GlyGlySerGly (GGSG) linker was inserted between DDX3X/Y and EGFP.

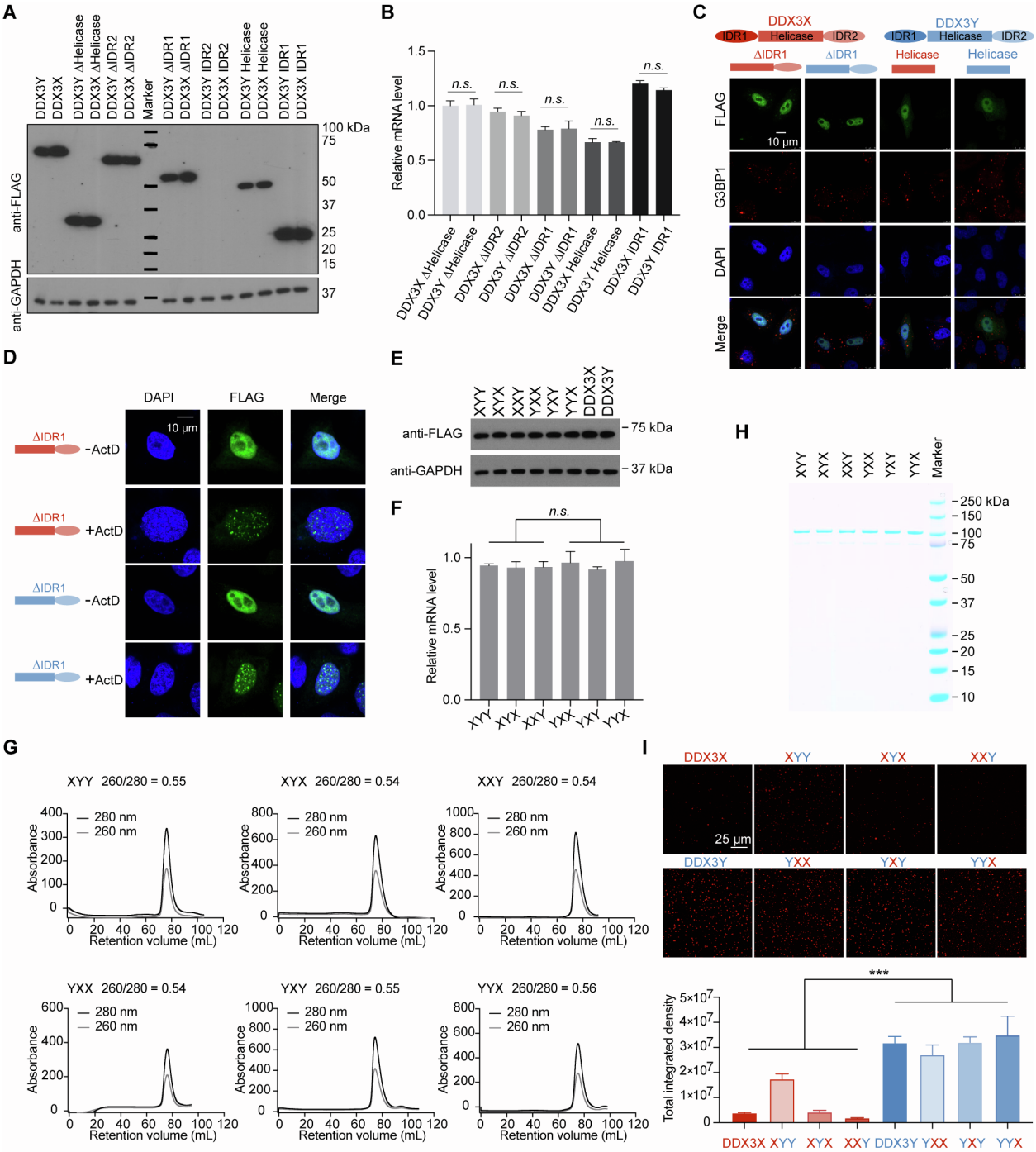
A
DDX3Y
DDX3X
DDX3Y ΔHelicase
DDX3X ΔHelicase
DDX3Y ΔIDR2
DDX3X ΔIDR2
Marker
DDX3Y ΔIDR1
DDX3X ΔIDR1
DDX3Y IDR2
DDX3X IDR2
DDX3Y Helicase
DDX3X Helicase
DDX3Y IDR1
DDX3X IDR1
100 kDa
75
50
37
25
20
15
anti-FLAG
anti-GAPDH
37
B
Relative mRNA level
1.5
1.0
0.5
0.0
n.s.
DDX3X ΔHelicase
DDX3Y ΔHelicase
DDX3X ΔIDR2
DDX3Y ΔIDR2
DDX3X ΔIDR1
DDX3Y ΔIDR1
DDX3X Helicase
DDX3Y Helicase
DDX3X IDR1
DDX3Y IDR1
C
DDX3X
IDR1
Helicase
IDR2
ΔIDR1
ΔIDR1
DDX3Y
IDR1
Helicase
IDR2
Helicase
Helicase
FLAG
G3BP1
DAPI
Merge
10 μm
D
DAPI
FLAG
Merge
ΔIDR1
-ActD
ΔIDR1
+ActD
ΔIDR1
-ActD
ΔIDR1
+ActD
10 μm
E
XYY
XYX
XXY
YXX
YXY
YYX
DDX3X
DDX3Y
anti-FLAG
anti-GAPDH
75 kDa
37 kDa
F
n.s.
Relative mRNA level
1.0
0.5
0.0
XYY
XYX
XXY
YXX
YXY
YYX
H
XYY
XYX
XXY
YXX
YXY
YYX
Marker
250 kDa
150
100
75
50
37
25
20
15
10
G
XYY 260/280 = 0.55
XYX 260/280 = 0.54
XXY 260/280 = 0.54
YXX 260/280 = 0.54
YXY 260/280 = 0.55
YYX 260/280 = 0.56
280 nm
260 nm
Absorbance
Retention volume (mL)
I
DDX3X
XYY
XYX
XXY
DDX3Y
YXX
YXY
YYX
25 μm
***
Total integrated density
5×10^7
4×10^7
3×10^7
2×10^7
1×10^7
0
DDX3X XYY
XYX
XXY
DDX3Y YXX
YXY
YYX

Figure S3 IDR1 of DDX3Y more strongly promotes phase separation than IDR1 of DDX3X. Related to Figure 3. (A) Western blot results showing the expression of the wild type and truncated variants of DDX3X (including DDX3X$^{\Delta helicase}$, DDX3X$^{\Delta IDR2}$, DDX3X$^{\Delta IDR1}$, DDX3X^{IDR2}, DDX3X^{helicase}, DDX3X^{IDR1}) and DDX3Y (including DDX3Y$^{\Delta helicase}$, DDX3Y$^{\Delta IDR2}$, DDX3Y$^{\Delta IDR1}$, DDX3Y^{IDR2}, DDX3Y^{helicase}, DDX3Y^{IDR1}). The IDR2 domains alone do not express in HeLa cells. (B) RT-qPCR to show the transcript level of different DDX3X and DDX3Y truncations. All the truncations were normalized to the loading control GAPDH first and then normalized to DDX3X. DDX3X truncations were expressed at the comparable level to the corresponding DDX3Y truncations. *p* values were determined by a two-tailed t-test; *n.s.* $p > 0.05$. (C) Representative images of localization of DDX3$^{\Delta IDR1}$, DDX3Y$^{\Delta IDR1}$, DDX3X^{helicase}, DDX3Y^{helicase}, and G3BP1 in HeLa cells upon arsenite treatment (500 μm, 1 hr). Scale bar, 10 μm. (D) Representative images of localization of DDX3$^{\Delta IDR1}$ and DDX3Y$^{\Delta IDR1}$ with and without 5 μg/mL of actinomycin D (ActD) treatment for 2 hrs. Scale bar, 10 μm. (E) Western blot results showing the expression of the wild type and domain-swap variants of DDX3X and DDX3Y. (F) RT-qPCR to show the transcript level of different DDX3X and DDX3Y domain-swap variants. All the truncations were normalized to the loading control GAPDH first and then normalized to DDX3X. All the domain-swap variants were expressed at the comparable level. *p* values were determined by a two-tailed t-test; *n.s.* $p > 0.05$. (G) Chromatographic profile of the domain-swap variants with mCherry tag during purification. The black line refers to A_{280nm}, and the gray line refers to A_{260nm}. The final A_{260nm}/A_{280nm} was determined using a Nanodrop spectrophotometer. The ratios of A_{260nm}/A_{280nm} of DDX3X and DDX3Y indicate that the purified proteins don't contain noticeable RNA carryover. (H) SDS-PAGE gel of the final purified the domain-swap variants with mCherry tag. (I) *In vitro* droplet formation of 7.5 μM recombinant DDX3X-mCherry, DDX3Y-mCherry, and domain swap variants of DDX3X and DDX3Y in the absence of poly(U)-RNA. Scale bar, 25 μm. Quantification of the total integrated intensity of the different types of condensations. Error bars represent s.d. from three repeats at

each condition. *p* values were determined by nested t-test in the Prism to compare all domain-swapped variants with X^{IDR1} versus all domain-swapped variants with Y^{IDR1}; ***$p < 0.001$.

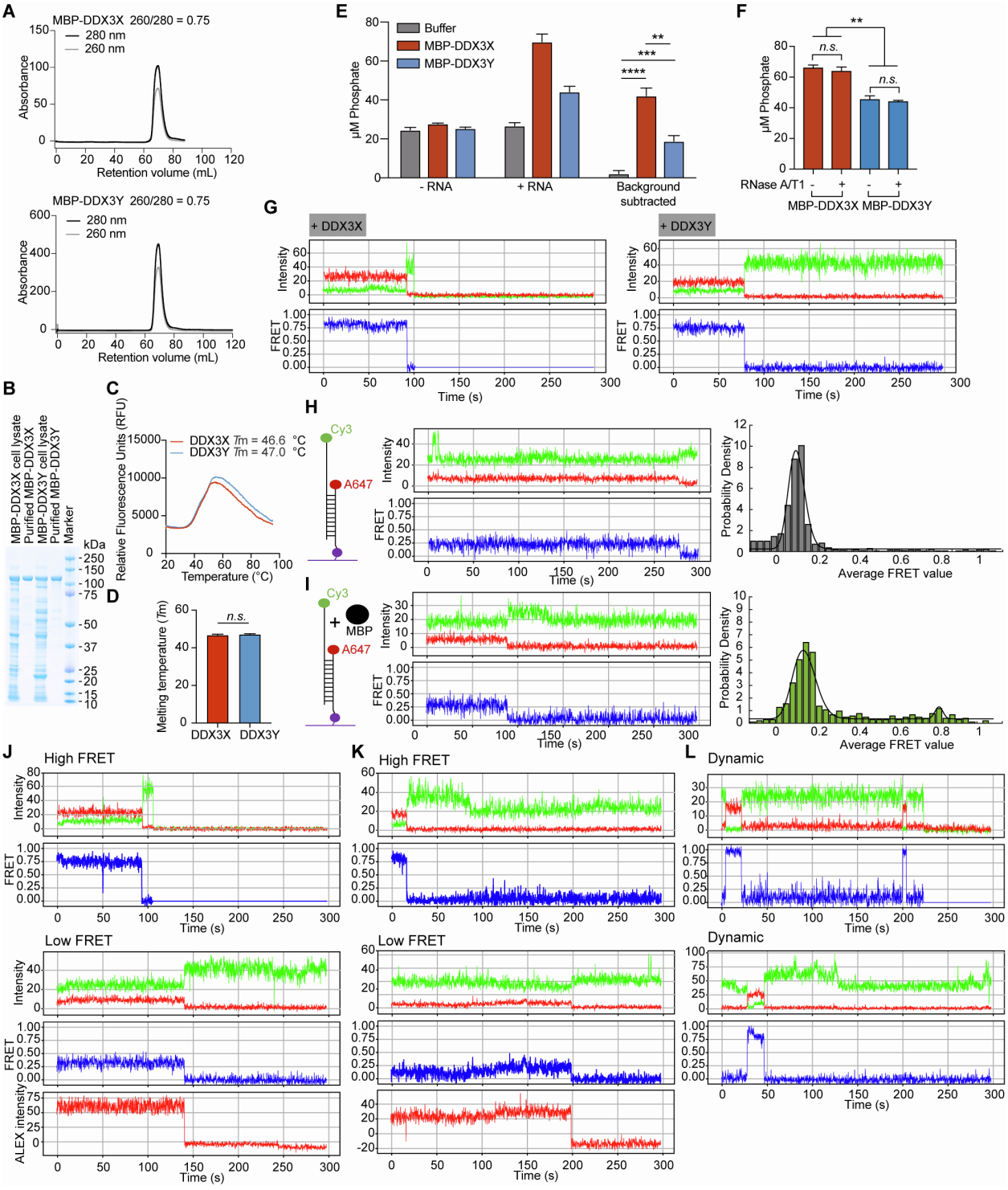
A
MBP-DDX3X 260/280 = 0.75
280 nm
260 nm
Absorbance
Retention volume (mL)
MBP-DDX3Y 260/280 = 0.75
B
MBP-DDX3X cell lysate
Purified MBP-DDX3X
MBP-DDX3Y cell lysate
Purified MBP-DDX3Y
Marker
kDa
C
Relative Fluorescence Units (RFU)
DDX3X Tm = 46.6 °C
DDX3Y Tm = 47.0 °C
Temperature (°C)
D
Melting temperature (Tm)
n.s.
DDX3X
DDX3Y
E
Buffer
MBP-DDX3X
MBP-DDX3Y
μM Phosphate
- RNA
+ RNA
Background subtracted
F
n.s.
RNase A/T1
MBP-DDX3X MBP-DDX3Y
G
+ DDX3X
+ DDX3Y
Intensity
FRET
Time (s)
H
Cy3
A647
Probability Density
Average FRET value
I
MBP
J
High FRET
Low FRET
ALEX intensity
K
L
Dynamic

Figure S4 The weaker ATPase activity of DDX3Y compared to DDX3X weakens its condensate disassembly. Related to Figure 4. (A) Chromatographic profile of MBP-DDX3X and MBP-DXDX3Y during purification. The black line refers to A_{280nm}, and the gray line refers to A_{260nm}. The final A_{260nm}/A_{280nm} ratio was determined using a Nanodrop spectrophotometer. (B) SDS-PAGE gel of the bacterial cell lysate and the final purified MBP-DDX3X and MBP-DDX3Y. (C) Differential Scanning Fluorometry (DSF) melting curves showing the relative fluorescence units with increasing temperature. The fluorescence is a product of SYPRO Orange dye, which resides on hydrophobic residues of exposed residues of DDX3X/DDX3Y and has a max fluorescence at 620 nm. The steady increase in fluorescence is due to the unfolding of the protein with increased temperature and the subsequent binding of the SYPRO Orange dye. (D) The melting temperatures (*Tm*, the temperature at which 50% of a protein sample is in a folded and 50% is in an unfolded state) of MBP-DDX3X and MBP-DDX3Y determined by DSF. *p* values were determined by a two-tailed t-test; *n.s.* $p > 0.05$. (E) Malachite green ATPase assay. Reactions were assembled as described in methods. Measurements were taken with 1.0 μM MBP-DDX3X, MBP-DDX3Y, or buffer with 2 mM ATP either in the absence of RNA ("- RNA") or with the addition of 100 ng/μL total HeLa RNA ("+ RNA") to stimulate ATPase activity after a 30 min reaction. "- RNA" values were subtracted from their corresponding "+ RNA" values as background ("Background Subtracted"). Values = mean ± s.d., n = 3 repeats. (F) Malachite green ATPase assays of MBP-DDX3X and MBP-DDX3Y with or without RNase treatment. Values = mean ± s.d., n = 3 repeats. A two-tailed t-test was used to calculate the *p*-values between +/- RNase treatment; a nested t-test was used to calculate the *p*-value between DDX3X and DDX3Y groups; *n.s.* $p > 0.05$, $^{**}p < 0.01$. (G) – (L) Recordings of single-molecule fluorescence intensities excited at 532 nm, corrected for channel sensitivities and spectral bleed-through as described in Methods. Green, Cy3 donor fluorescence; red, sensitized emission of Alexa 647 due to FRET; blue FRET Efficiency. The sudden decrease of the Alexa 647 and FRET traces accompanied by an increase of Cy3 intensity in each panel indicates photobleaching of the Alexa 647. Photobleaching of Alexa

647 was corroborated by direct excitation in alternating frames at 640 nm. (G) Representative fluorescent intensities and the FRET efficiency of RNA probe with MBP-DDX3X (left) and MBP-DDX3Y (right), which show high FRET. The histograms of FRET efficiencies are shown in Figure 4E. (H) The RNA probe alone gave low FRET, with a peak at E = ~0.12. Left panel: schematic of the RNA construct immobilized on the coverslip surface. Middle panel: representative figure showing the raw traces of the fluorescent intensities and the FRET efficiency trace. Right panel: histogram showing the distribution of FRET efficiencies from ~1000 traces. (I) The RNA probe with MBP (a control with no DDX3), gave low FRET, like the RNA probe alone. Left panel: schematic of the FRET assay configuration. Middle panel: representative plot showing the raw traces of the fluorescent intensities and the FRET efficiency trace. Right panel: histogram figure showing the distribution of FRET efficiency from ~400 traces, similar to the RNA in the absence of MBP. (J) Corresponding fluorescent intensities and FRET efficiency of the RNA probe with MBP-DDX3X and 1 mM ATP show high FRET and low FRET. The histogram is shown in Figure 4E. The lower panel of the low FRET trace shows ALEX direct excitation of Alexa 647 at 640 nm, indicating both donor and acceptor are present. (K) Corresponding fluorescent intensities and FRET efficiency of the RNA probe with MBP-DDX3Y and 1 mM ATP show high FRET and low FRET. The histogram is shown in Figure 4E. The lower panel of the low FRET trace shows ALEX direct excitation of Alexa 647, indicating both donor and acceptor are present. (L) Examples of corresponding fluorescent intensities and FRET efficiency of the RNA probe with 8 μM MBP-DDX3X (upper) and MBP-DDX3Y (lower) and 1 mM ATP, which show dynamic FRET presumably due to kinetics of dissociation and reassociation of the protein.

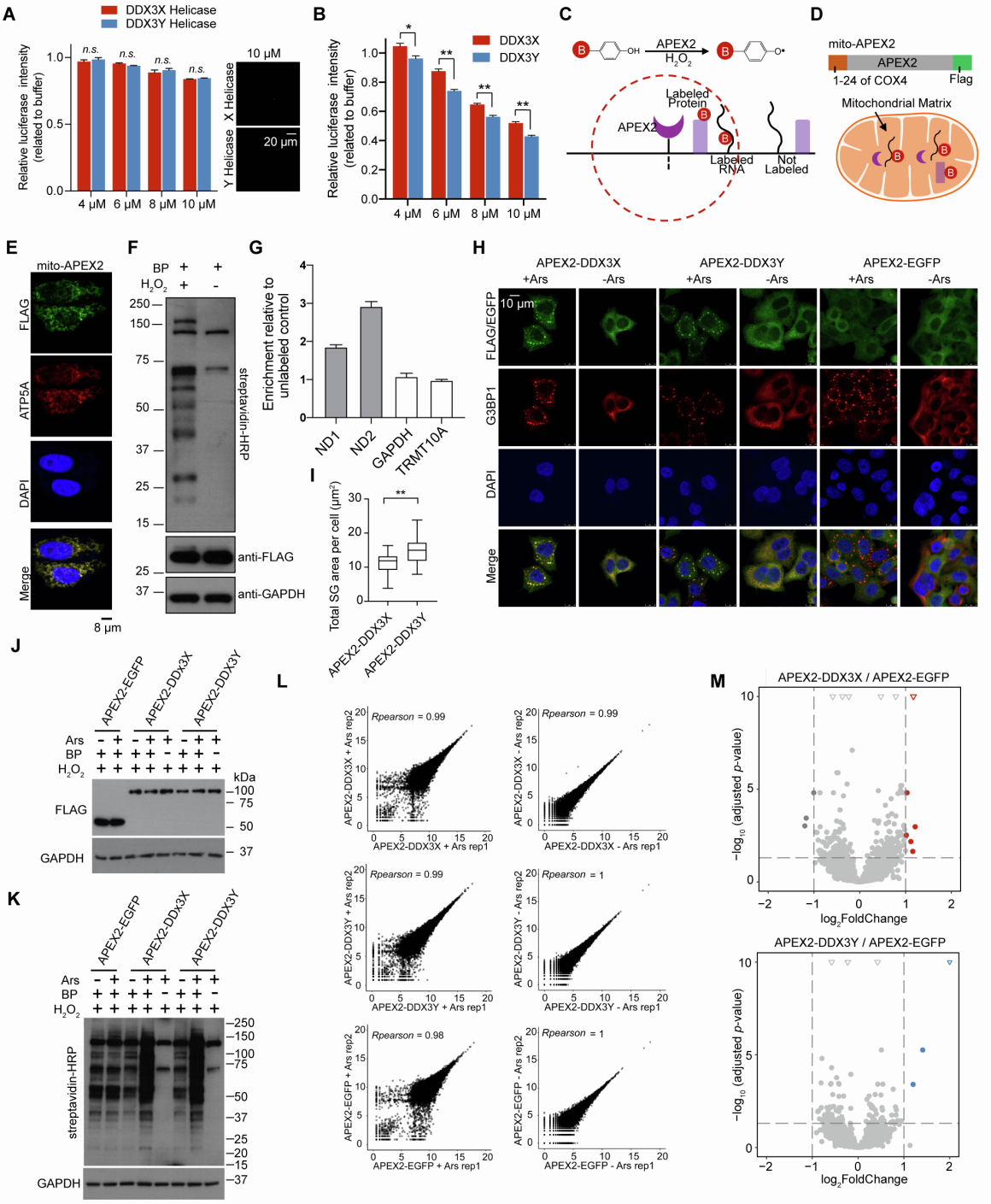
A
DDX3X Helicase
DDX3Y Helicase
Relative luciferase intensity (related to buffer)
n.s.
4 μM 6 μM 8 μM 10 μM
10 μM
20 μm
X Helicase
Y Helicase
B
DDX3X
DDX3Y
Relative luciferase intensity (related to buffer)
*
**
4 μM 6 μM 8 μM 10 μM
C
APEX2
H2O2
Labeled Protein
APEX2
Labeled RNA
Not Labeled
D
mito-APEX2
APEX2
1-24 of COX4
Flag
Mitochondrial Matrix
E
mito-APEX2
FLAG
ATP5A
DAPI
Merge
8 μm
F
BP
H2O2
250
150
75
50
37
25
15
streptavidin-HRP
anti-FLAG
anti-GAPDH
G
Enrichment relative to unlabeled control
ND1
ND2
GAPDH
TRMT10A
I
Total SG area per cell (μm²)
**
APEX2-DDX3X
APEX2-DDX3Y
H
APEX2-DDX3X
APEX2-DDX3Y
APEX2-EGFP
+Ars
-Ars
10 μm
FLAG/EGFP
G3BP1
DAPI
Merge
J
APEX2-EGFP
APEX2-DDX3X
APEX2-DDX3Y
Ars
BP
H2O2
kDa
100
75
50
37
FLAG
GAPDH
K
APEX2-EGFP
APEX2-DDX3X
APEX2-DDX3Y
Ars
BP
H2O2
250
150
100
75
50
37
25
20
15
streptavidin-HRP
GAPDH
L
Rpearson = 0.99
APEX2-DDX3X + Ars rep2
APEX2-DDX3X + Ars rep1
Rpearson = 0.99
APEX2-DDX3X - Ars rep2
APEX2-DDX3X - Ars rep1
Rpearson = 0.99
APEX2-DDX3Y + Ars rep2
APEX2-DDX3Y + Ars rep1
Rpearson = 1
APEX2-DDX3Y - Ars rep2
APEX2-DDX3Y - Ars rep1
Rpearson = 0.98
APEX2-EGFP + Ars rep2
APEX2-EGFP + Ars rep1
Rpearson = 1
APEX2-EGFP - Ars rep2
APEX2-EGFP - Ars rep1
M
APEX2-DDX3X / APEX2-EGFP
−log10 (adjusted p-value)
log2FoldChange
APEX2-DDX3Y / APEX2-EGFP
−log10 (adjusted p-value)
log2FoldChange

Figure S5 DDX3X and DDX3Y condensation inhibit the translation of luciferase RNA, and DDX3X- and DDX3Y-positive SGs have shared and unique RNA constituents in cells. Related to Figure 5. (A) Quantification of translation inhibition in the presence of the mCherry-tagged protein truncation variants (which contain only the helicase domains of DDX3X or DDX3Y) at the indicated concentrations. Error bars represent s.d. from three biological repeats at each condition. Images below the graph did not reveal noticeable phase separation in the reticulocyte assay at 10 μM DDX3; scale bar, 10 μm. (B) The *in vitro* translation assays performed at the same conditions as in Figure 5B except with the addition of 1 mM ATP. (C) Schematic illustration of APEX2-mediated proximity labeling reaction and spatial labeling of RNAs and proteins. (D) Schematic illustration of mito-APEX2 fusion system in the mitochondrial matrix. APEX2 fusion with the first 24 amino acids from mitochondrial protein COX4 allowed us to validate the APEX2-proximity labeling method used in the experiments shown in Figure 5G. (E) Representative images of co-localization of mito-APEX2 with ATP5A (a mitochondrial protein). (F) Western blots show the APEX2 labeling using an anti-biotin antibody. Proximity labeling only occurred in the presence of both BP and hydrogen peroxide. Bands at 130, 75, and 72 kDa are endogenous biotinylated proteins. BP: biotin phenol. (G) RT-qPCR quantification of cytosolic (*GADPH* and *TRMT10A*) and mitochondrial (*ND1* and *ND2*) transcripts in APEX-RNA labeling experiments. (H) Representative images of localization of APEX2-DDX3X, APEX2-DDX3Y, or APEX2-EGFP with G3BP1 in HeLa cells before and after arsenite treatment (500 μM, 1 hr). Scale bar, 10 μm. (I) Box plot of the total SG area of APEX2-DDX3X- or APEX2-DDX3Y-positive SGs per cell across 20 cells upon arsenite treatment (500 μM, 1 hr); (20 cells each from 3 biologically independent experiments). *p* values were determined by two-tailed t-test; ** $p < 0.01$. (J) Western blot results showing the expression of APEX2-EGFP, APEX2-DDX3X, and APEX2-DDX3Y in HeLa cells. (K) Western blot results showing the APEX2 labeling using an anti-biotin antibody. Ars: arsenite; BP: biotin phenol. (L) Correlation between the biological repeats of APEX-seq samples including

APEX2-DDX3X, APEX2-DDX3Y, APEX2-EGFP with (left) and without arsenite (right) treatment. (M) Top, a volcano plot showing differential RNA enrichment in streptavidin pull-downs from APEX2-DDX3X expressing cells compared to APEX2-EGFP expressing cells without 500 μM arsenite treatment. Differentially expressed genes are shown in red for APEX2-DDX3X-enriched RNAs (adjusted $p < 0.05$, $\log_2$ fold change > 1) and dark gray for APEX2-DDX3X-depleted RNAs (adjusted $p < 0.05$, $\log_2$ fold change < -1). Bottom, the corresponding volcano plot for APEX2-DDX3Y expressing cells. Differentially expressed genes are shown in blue for APEX2-DDX3Y-enriched RNAs (adjusted $p < 0.05$, $\log_2$ fold change > 1). The rest of the RNAs (which do not fit the criteria of the differential expression with $\log_2$ fold change < -1 or $\log_2$ fold change > 1, adjusted $p < 0.05$) are shown in light gray for both DDX3X and DDX3Y. The triangles represent the transcripts with $\log_2$ fold change > 2 in the X-axis; $-\log_{10}$ adjusted p >10 in the Y-axis. Of note, without arsenite treatment, APEX2-DDX3X, APEX2-DDX3Y and APEX2-EGFP are diffuse in the cytoplasm as shown in Figure S5H. Therefore, there are no significantly enriched transcripts by APEX2-DDX3X and APEX2-DDX3Y in comparison to APEX2-EGFP in the no arsenite treated condition.

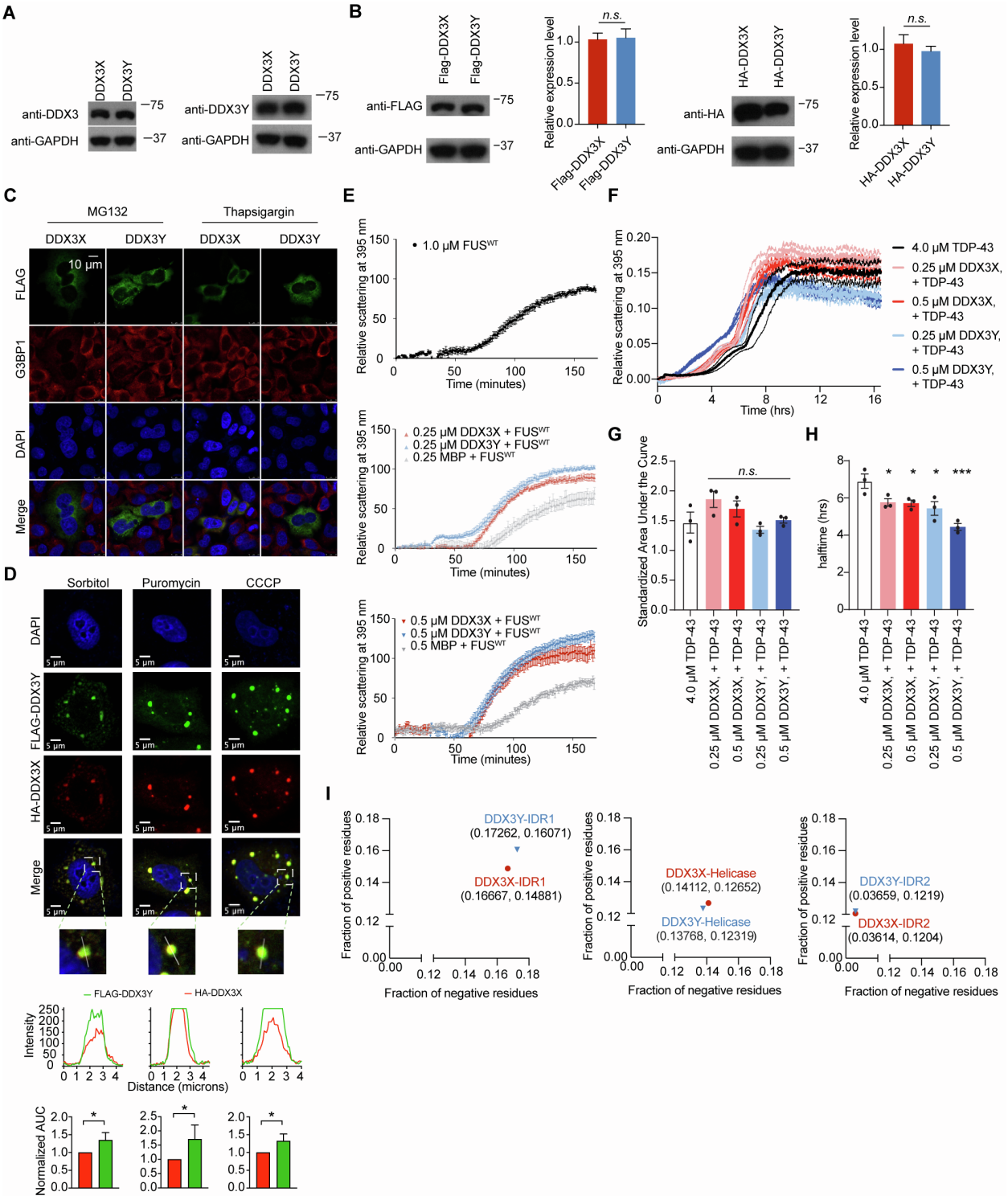
A
DDX3X
DDX3Y
anti-DDX3
anti-GAPDH
anti-DDX3Y
B
Flag-DDX3X
Flag-DDX3Y
anti-FLAG
Relative expression level
n.s.
HA-DDX3X
HA-DDX3Y
anti-HA
C
MG132
Thapsigargin
FLAG
G3BP1
DAPI
Merge
10 μm
D
Sorbitol
Puromycin
CCCP
FLAG-DDX3Y
HA-DDX3X
Intensity
Distance (microns)
Normalized AUC
E
1.0 μM FUS^WT
Relative scattering at 395 nm
Time (minutes)
0.25 μM DDX3X + FUS^WT
0.25 μM DDX3Y + FUS^WT
0.25 MBP + FUS^WT
0.5 μM DDX3X + FUS^WT
0.5 μM DDX3Y + FUS^WT
0.5 MBP + FUS^WT
F
4.0 μM TDP-43
0.25 μM DDX3X, + TDP-43
0.5 μM DDX3X, + TDP-43
0.25 μM DDX3Y, + TDP-43
0.5 μM DDX3Y, + TDP-43
Time (hrs)
G
Standardized Area Under the Curve
H
halftime (hrs)
I
DDX3Y-IDR1
(0.17262, 0.16071)
DDX3X-IDR1
(0.16667, 0.14881)
DDX3X-Helicase
(0.14112, 0.12652)
DDX3Y-Helicase
(0.13768, 0.12319)
DDX3Y-IDR2
(0.03659, 0.1219)
DDX3X-IDR2
(0.03614, 0.1204)
Fraction of positive residues
Fraction of negative residues

Figure S6 A combination of DDX3X and DDX3Y shows a stronger propensity of LLPS and translation repression than DDX3X alone, and DDX3Y enhances FUS aggregation and accelerates TDP-43 aggregation more than DDX3X. Related to Figure 6. (A) Western blot showing the expression of FLAG-DDX3X or FLAG-DDX3Y using anti-DDX3 (Abcam ab196032, left) or anti-DDX3Y (Invitrogen PA5-22050, right) antibodies. The results showed that neither of the antibodies distinguished DDX3X from DDX3Y. (B) Western blots showing the expression of FLAG-DDX3X, HA-DDX3X, FLAG-DDX3Y, HA-DDX3Y using anti-FLAG or anti-HA antibodies. The intensity of each band was quantified using Fiji. The intensity of each DDX3X or DDX3Y band was normalized to the corresponding GAPDH intensity and then normalized to the DDX3X samples. Error bars represent s.d. of three biological replicates. *P* values were determined by a two-tailed t-test; *n.s.* $p > 0.05$. (C) Immunofluorescence images of FLAG-DDX3X, FLAG-DDX3Y, and G3BP1 in Hela cells treated with MG132 (proteasome inhibitor, 10 μM, 3 hrs) or Thapsigargin (potent inhibitor of sarco/endoplasmic reticulum Ca^{2+}-ATPases, 10 μM, 1 hr). Under these conditions, we did not detect SG formation. Scale bar, 10 μm. (D) Reciprocal immunofluorescence images of SGs containing both HA-DDX3X and FLAG-DDX3Y in HeLa cells treated as the same as in Figure 6A. Below each image, traces of fluorescence intensity profiles through positions denoted by the white lines in the merged images. AUC normalized to that of HA-DDX3X is plotted for each intensity profile and shows that the signal from FLAG-DDX3Y is consistently higher than the signal from HA-DDX3X. (E) The impact of DDX3X and DDX3Y on FUS aggregation was measured using a Tecan plate reader measuring scattering at 395 nm. The indicated concentration of MBP-TEV-DDX3X, MBP-TEV-DDX3Y, or MBP (or buffer alone) was incubated with 1 μg TEV protease for 30 min at room temperature to generate untagged DDX3X and DDX3Y. 1 μM GST-TEV-FUS (or an equal volume of elution buffer, see methods) was then added to the reaction, and turbidity was used to assess aggregation by measuring scattering at 395 nm. (F) The impact of DDX3X and DDX3Y on TDP-43 aggregation was measured using a Tecan plate reader measuring scattering at 395 nm. The indicated concentrations of MBP-TEV-DDX3X or

MBP-TEV-DDX3Y, or an equal volume of elution buffer (200 mM NaCl, 25 mM Tris-HCl pH 8.0) for conditions without either protein, was incubated in TDP-43 assay buffer (150 mM NaCl, 20 mM HEPES-NaOH pH 7.0, and 1 mM DTT) with 0.25 µg TEV protease for 30 minutes at room temperature to generate untagged DDX3X and DDX3Y. Turbidity was assessed by measuring scattering at 395 nm. 4.0 µM TDP-43 (or an equal volume of TDP-43 assay buffer) was then added to the reaction, and turbidity was measured for an additional 16 hours (n = 3; dotted lines of corresponding colors represent ± s.e.m.). (G) Area under the curve of the individual replicates summarized in Figure S6F was used to compare the extent of aggregation for each condition (one-way ANOVA comparing to the 4.0 µM TDP-43 condition, Dunnett's multiple comparisons test, ± s.e.m., *n.s.* means $p > 0.05$). (H) The $t_{1/2}$ of aggregation was used to compare the kinetics of aggregation for each condition. The $t_{1/2}$ was obtained by performing nonlinear regression (asymmetric sigmoidal) on the individual replicates summarized in Figure S6F from the time of TDP-43 addition (t = 31 min) through the end of the assay (t = 16.5 hrs). Decreased halftime values indicate that both DDX3X and DDX3Y accelerate TDP-43 aggregation (one-way ANOVA comparing to the 4.0 µM TDP-43 condition, Dunnett's multiple comparisons test, ± s.e.m., $*p < 0.05$ and $***p < 0.001$). (I) The fraction of negative and positively charged amino acids in the IDR1, IDR2, and helicase domain of DDX3X (red) or DDX3Y (blue). The fractions were calculated using numbers of the charged residues over the total number of amino acids in the individual domains via CIDER software.

Table S1. Summary of smFRET values, related to Figure 4.

	Relative area of Low FRET peak	Average low-FRET Efficiency	Average high-FRET Efficiency
RNA probe only	1	0.124 (0.120, 0.127)	NA
8 μM MBP	0.933 (0.877, 0.970)	0.164 (0.156, 0.172)	0.789 (0.656, 0.816)
8 μM MBP + DDX3X/3Y	0	NA	0.807 (0.800, 0.814)
2 μM DDX3X	NA	NA	0.841 (0.830, 0.850)
4 μM DDX3X	NA	NA	0.822 (0.819, 0.825)
8 μM DDX3X	NA	NA	0.818 (0.814, 0.822)
2 μM DDX3Y	NA	NA	0.845 (0.834, 0.851)
4 μM DDX3Y	NA	NA	0.811 (0.808, 0.814)
8 μM DDX3Y	NA	NA	0.819 (0.815, 0.824)
2 μM DDX3X + ATP	0.061 (0.022, 0.10)	0.010 (-0.0097, 0.032)	0.836 (0.827, 0.844)
4 μM DDX3X + ATP	0.249 (0.218, 0.285)	-0.0039 (-0.0081, - 0.00074)	0.840 (0.834, 0.845)
8 μM DDX3X + ATP	0.41 (0.37, 0.45)	-0.010 (-0.014, - 0.0062)	0.819 (0.812, 0.825)
2 μM DDX3Y + ATP	0.019 (0.013, 0.034)	0.001612 (0.001608, 0.001671)	0.85 (0.84, 0. 86)
4 μM DDX3Y + ATP	0.161 (0.130, 0.185)	-0.0064 (-0.011, - 0.0019)	0.818 (0.813, 0.822)
8 μM DDX3Y + ATP	0.23 (0.20, 0.26)	-0.0077 (-0.012, - 0.0031)	0.824 (0.816, 0.830)

"NA" indicates the absence of the corresponding peak.
The values in the parentheses are the 95% confidence intervals of the indicated value.